UNDERSTANDING AND EXPLOITING THE EFFECTS OF LOADING ON ULTRASONIC SENSING SYSTEMS FOR STRUCTURAL HEALTH MONITORING

Jennifer E. Michaels, Thomas E. Michaels, Sang Jun Lee, Xin Chen, Navneet Gandhi and Fan Shi

School of Electrical and Computer Engineering
Georgia Institute of Technology

MARCH 31, 2012
Final Report

Table of Contents

Table of Contents (Continued)

List of Figures

List of Figures (Continued)

List of Figures (Continued)

List of Figures (Continued)

List of Figures (Continued)

List of Tables

Foreword

The project reported herein was conducted in the QUEST Laboratory in the School of Electrical and Computer Engineering at the Georgia Institute of Technology during the time period 07-January-2009 through 31-January-2012. The work was conducted under Air Force Contract FA8650-09-C-5206, with Air Force technical management provided by Mr. Charles Buynak, AFRL/RXLP. Georgia Tech program management was provided by Professor Jennifer Michaels, who also served as Principal Investigator. Key project contributors were Professor Thomas E. Michaels, co-Principal Investigator, and Dr. Sang Jun Lee, Postdoctoral Associate, who were involved in all aspects of the project. Mr. Navneet Gandhi, Graduate Research Assistant, developed the theory of acoustoelastic Lamb wave propagation, Mr. Fan Shi, Graduate Research Assistant, was responsible for inverting acoustoelastic data to obtain applied loads, and Mr. Xin Chen, Graduate Research Assistant, was instrumental in running the experiments and performing the load-differential analysis. All Georgia Tech participants gratefully acknowledge the valuable discussions with and input received from Dr. Eric Lindgren, AFRL/RXLP, during the course of this project.

1. Introduction

Structural health monitoring (SHM), also referred to as *in situ* nondestructive evaluation (NDE), seeks to apply NDE methods to autonomously assess a structure for damage using permanently mounted sensors. One method that is receiving widespread attention for SHM is guided elastic waves, which are being investigated for large area monitoring of plate and shell-like components using spatially distributed arrays of sensors. Although prior work on flat plates has demonstrated reasonable sensitivity to artificial defects under laboratory conditions, there are significant issues with signal complexity and sensitivity to changing environmental (boundary) conditions. Signal complexity results from waves interacting with fastener holes, ribs, stiffeners, thickness changes, etc., making signal interpretation difficult. Baseline subtraction is generally effective in the laboratory where it can be assumed that residual signals result from damage, facilitating detection and localization. However, it is well known that even small temperature changes (~1 °C) significantly affect the subtraction results. Compensation methods have enabled detection and localization of reasonably small artificial defects (~5-10 mm) in flat plates via baseline subtraction, but it is unrealistic to think that they will work in a complex aircraft environment and for other types of changing conditions.

Besides temperature, flight-induced loads are the environmental effect that is most likely to have a significant adverse effect on guided wave signals. In an undamaged structure, loads cause anisotropic dimensional and wave speed changes, and can also cause boundary conditions of built-up structures to change. In a damaged structure, load changes can cause cracks to open and close, and poor bonds to make and break contact; there may be other less obvious effects that occur prior to formation of macro-cracks. The goal of the program reported here was to first understand and then exploit the effects of applied loads on guided wave structural health monitoring. The emphasis was on metallic structures, although the methods developed should be generally applicable to composites.

2. Background

Guided waves in plates, which are known as Lamb waves, are of considerable practical interest for both nondestructive evaluation and structural health monitoring because of their ability to propagate relatively long distances while still maintaining sensitivity to damage [1,2]. Because of the long propagation distances, particularly as compared to most bulk wave NDE methods, Lamb waves are particularly sensitive to changes in the propagation environment, such as temperature, stress and surface conditions [3,4].

Different sensor array geometries have been proposed to implement guided wave NDE and SHM systems. Zhao *et al.* [5] compared circular, rectangular and parallel linear arrays for Lamb wave tomography. Yu and Giurgiutiu [6] constructed five different 2-D compact phased arrays and applied beamforming to compare the damage detection capabilities of the five geometries. One limitation of the above tomographic and compact array approaches is the requirement of a relatively large number of transducers. A sparse (i.e., spatially distributed) array geometry was initially proposed by Wang *et al.* [7] and later used by others [8,9] to achieve detection and localization of discrete damage using fewer transducers than are typically required for the tomographic and compact array approaches. Another advantage of the sparse array geometry is that forward scattered as well as backscattered signals are incorporated into imaging algorithms, which enables the approach to take advantage of the increased sensitivity of forward scattered waves to damage as compared to backscattered waves [10].

The idea of baseline comparison plays a key role in many SHM methods. Ideally, by subtracting baseline signals recorded from the damage-free structure from current test signals, a residual signal, which is assumed to arise from damage, is obtained. A variety of signal processing algorithms can be applied to these residual signals for damage detection, localization and characterization. However, such a process is strongly affected by mismatched environmental and operational conditions. Lu and Michaels [11] and Konstantinidis *et al.* [12] both addressed the temperature mismatch problem by optimal baseline selection, where a number of baselines were recorded at different temperatures and the optimal baseline that minimized the residual signal was selected. The signal stretch method, which was introduced in [11] and since used by others [3,13], adjusts the optimal baseline by stretching to better match it to the current test signals.

Another environmental condition, surface wetting, has not been as fully investigated as temperature. Takatsubo *et al.* [14] considered the effect of droplets of water on an SHM system consisting of two transducers monitoring fatigue crack growth. In [4], different features were extracted from diffuse ultrasonic wave signals and evaluated for damage detection in the presence of surface wetting. All chosen features were shown to have some capability of discriminating surface wetting from damage. Li *et al.* [15] recently studied the effects that surface wetting can have on guided waves, and results indicate that even small amounts of surface wetting can adversely affect the performance of guided wave SHM systems.

The theory to explain the dependence of wave speed on stress, or acoustoelasticity, was developed by Hughes and Kelly by applying the Murnaghan theory of finite deformation to propagation of bulk elastic waves in an initially isotropic solid subjected to a static predeformation [16]. They specifically considered the cases of hydrostatic pressure and uniaxial compressive stresses and derived expressions for changes in shear and longitudinal wave speeds as a function of applied stress for known material properties. Their work was extended to

materials of arbitrary symmetry by Toupin and Bernstein [17]. The comprehensive article in [18] provides a thorough treatment of acoustoelasticity with an emphasis on stress measurements via shear wave birefringence.

Acoustoelastic Rayleigh waves have also been quite thoroughly investigated, e.g., [19,20], but there are significantly fewer published works on other types of acoustoelastic guided waves. Husson [21] considered acoustoelastic Lamb waves from a theoretical point of view and, among other things, predicted a strong frequency dependence of the acoustoelastic constants. Qu and Liu [22] generated dispersion curves for waves propagating in a stressed aluminum plate, but did not investigate dependence on the direction of propagation. Rizzo and Lanza di Scalea [23] measured changes in wave speed with tensile loads for guided waves in bars, and found a strong frequency dependence of the acoustoelastic constants. Lematre *et al.* [24] developed theory for Lamb wave propagation in stressed piezoelectric plate structures but showed only numerical results for propagation along the direction of the applied uniaxial load. The semi-analytical finite element method has been applied to acoustoelastic wave propagation in bar-like structures (i.e., rails) [25].

Fatigue cracks are one of the most common defect types in metallic plate structures and frequently initiate from fastener holes. It is well known that closed cracks are hard to detect with conventional ultrasonic testing methods because ultrasound can propagate through a tightly closed crack [26,27]; applied loads can open such cracks and make them easier to detect. Research on load modulation of ultrasound with fatigue cracks can be traced back to 1970s and has been the subject of a number of investigations. Frandsen *et al.* [26] used acoustic techniques to qualitatively measure the area over which closure occurred. Kim *et al.* [28] investigated closed fatigue cracks using surface acoustic waves and suggested that modulation of loading about a low mean static load was able to enhance the detection of small closed cracks. Mi *et al.* [29] used the bulk wave energy transmitted through the region of a fastener hole to dynamically monitor the initiation and growth of fatigue cracks. Connolly and Rokhlin [30] analyzed the backscattered ultrasonic response to fatigue cracking as a function of transit time, fatigue life, and applied load to visualize and identify specific echoes scattered from geometrical features of the specimen and crack. Ohara *et al.* [31] recently introduced a nonlinear ultrasonic imaging method whereby a phased array was used to create linear and subharmonic images. Images obtained at different applied loads were subtracted to better visualize fatigue cracks.

This report is organized as follows. Section 3 summarizes experiments performed, Section 4 develops the theory for acoustoelastic Lamb waves, Section 5 considers inversion of load-dependent Lamb wave behavior, and Section 6 presents key results from the project in terms of fatigue crack detection and localization under variable loading conditions. Concluding remarks are made in Section 7, including recommendations for future work. Note that a list of all publications to date resulting from this project follows the references.

3. Description of Experiments

A total of eight aluminum plate specimens were tested under load as a part of this project. Although each experiment was different, there are several common factors between all experiments. The material was 6061-T6 AL, the specimen size was nominally 12" × 24" (305 mm × 610 mm) to accommodate the testing machine grips, the thickness was either 0.25" or 0.125" (6.35 mm or 3.175 mm), and the transducers were constructed from 7 mm diameter PZT discs operating in radial mode with a resonant frequency of 300 kHz (Steimer & Martins, Part Number SMD07T05R411, www.steminc.com). Information about each plate specimen is summarized in Table 3.1 and additional details are provided in the following sections.

Table 3.1. Summary of specimens tested.

Plate No.	Thickness	Fatigued?	Comments
1	0.25”	No	Data recorded as a function of load and temperature using 150 and 600 kHz excitations (data not reported here).
2	0.25”	No	Data recorded as a function of load and temperature using 150, 250, 400 and 600 kHz excitations.
3	0.125”	Yes	Plate tested twice but with two different sets of sensors. Data recorded with glued-on mass prior to fatiguing. First plate to be tested with chirp excitations.
4	0.125”	Yes	Plate tested with a short stiffener section. Some fatiguing but with no change in bonding. Artificial disbonds were then introduced.
5	0.125”	Yes	Cracks grown from initial drilled hole. Stiffener added and more data recorded.
6	0.125”	Yes	Cracks grown from four initial drilled holes. Data also recorded at different temperatures.
7	0.125”	Yes	Plate with initial drilled hole and bonded doubler. Partway through it was noticed that the doubler had become unbonded, at which time it was bolted in place.
8	0.125”	Yes	Plate with initial drilled hole and bonded/bolted doubler. Data recorded with various combinations of bolts present and tightness.

3.1 Plate #1

The purpose of the plate #1 test was to obtain data for guided waves of different modes and frequencies propagating at different angles and under different uniaxial loads. The goal was to understand the effects of applied loads on guided wave propagation in a homogeneous, isotropic plate. Eight transducers were mounted on a 6061-T6 aluminum plate of dimensions 12" × 24" × 0.25" (305 mm × 610 mm × 6.35 mm). The transducers were arranged at 45° increments on a 218 mm diameter circle centered on the plate; see Figure 3.1(a) for a diagram of the plate geometry and transducer locations.

The transmitters were excited using five-cycle, Hann-windowed tone bursts centered at both 150 kHz and 600 kHz. Data were recorded for each frequency at loads of 0 to 46 MPa at steps of 9.2 MPa, for a total of 12 signals recorded from each transducer pair. Results indicated that additional angles of propagation would be useful, which motivated the design of Plate #2. No data from this plate is reported here.

3.2 Plate #2

The purpose of the plate #2 test was also to obtain data for guided waves of different modes and frequencies propagating at different angles and under different uniaxial loads. The plate dimensions were the same as for plate #1, and a total of 12 transducers were mounted at unequal increments on a 218 mm diameter circle centered on the plate. Data were recorded from nine of the 45 possible transmit-receive pairs as shown in Figure 3.1(b) at eleven uniaxial loads (0 MPa to 57.5 MPa in steps of 5.75 MPa). Excitations were five-cycle Hann-windowed sinusoids centered at four distinct frequencies to produce an unambiguous first arrival of a specific Lamb wave mode: 150 kHz (S_0 mode), 250 kHz (S_0 mode), 400 kHz (A_1 mode), and 600 kHz (S_1 mode). There were a total of 44 signals recorded from each transducer pair (11 loads and four frequencies).

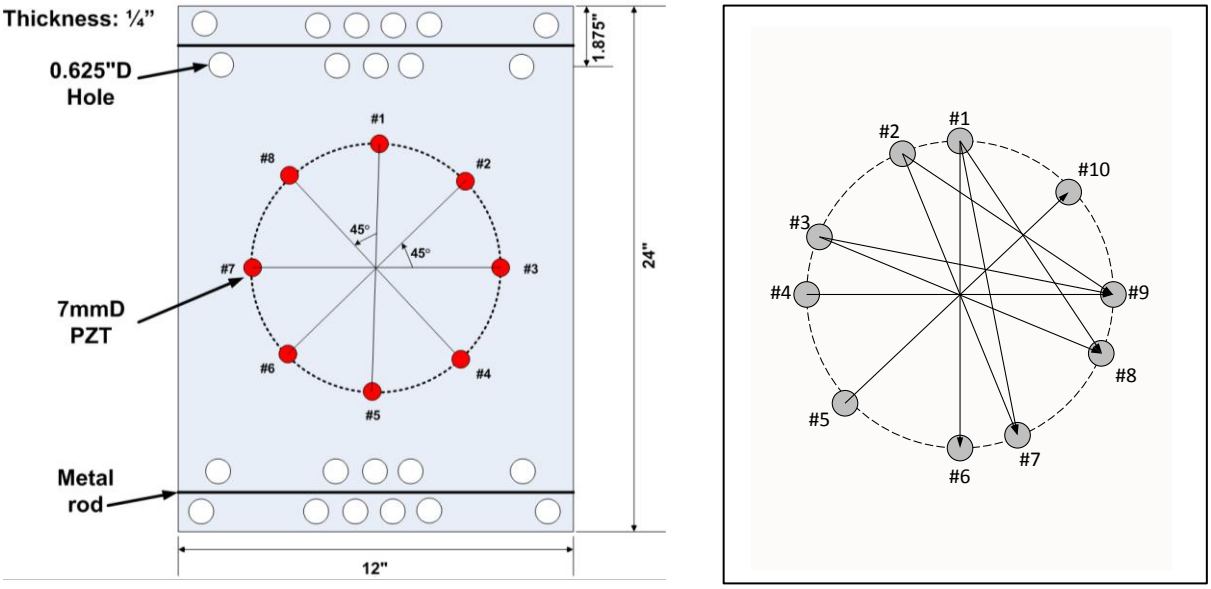

Figure 3.1. (a) Sketch of Plate #1 geometry including mounted transducers. (b) Sketch of transducers mounted on Plate #2 and nine selected propagation paths.

3.3 Plate #3

This 6061-T6 aluminum plate of dimensions 12" × 24" × 0.125" (305 mm × 610 mm × 3.175 mm) was instrumented with six bonded PZT discs arranged in a near-circular but asymmetrical pattern as shown in Figure 3.2. The nominal transducer locations, which are listed in Table 3.2, were selected to avoid symmetries and in particular to ensure that there were no redundant transducer-to-transducer distances. This characteristic ensures unique transducer-to-transducer path lengths, which is useful for *in situ* group velocity calibration. These nominal transducer locations were used for all subsequent plates (#4-#8), which were of the same dimensions and material as Plate #3.

This plate was initially tested in several ways to develop the procedures that were used for all subsequent tests. Data were recorded with and without glued-on masses prior to fatiguing,

and the plate was fatigued until the maximum final crack length was about 1" (25 mm). Chirp-based testing was developed and implemented to permit efficient recording of multi-frequency data, and equivalent tone burst responses were obtained via post-processing [32]. This development was critical to avoid excessive plastic deformation that would have otherwise been caused by having to keep a static load applied to the specimen while all frequencies were used to excite the transducer pairs.

The protocol for fatiguing and recording data for this and all subsequent plates is described as follows. The plate was fatigued with a 3 Hz sinusoidal tension-tension load ranging from 16.5 to 165 MPa. Fatiguing was periodically paused and ultrasonic data were recorded as a function of applied static tensile load from 0 to 115 MPa in steps of 11.5 MPa, which corresponds to 0% to 100% load with a 10% load step (11 loading conditions for each data set). A National Instrument PXIe-5122 waveform generator was used to generate a linear chirp excitation from 50 to 500 kHz with a duration of 0.2 ms and an amplitude of ±10 volts. A Panametrics 5072PR pulser-receiver was used to amplify the received signals, and a custom multiplexer switched between the 15 unique transmit-receive pairs. The received signals were then digitized by a National Instrument PXI-5412 14-bit digitizer at a sampling frequency of 20 MHz. For each acquisition, 20 waveforms were averaged to improve the signal-to-noise ratio. Received signals were filtered to yield the equivalent narrow-band tone burst response as described in [32]. A 3-cycle or 5-cycle Hann-windowed tone burst centered at 100 kHz was selected because of the purity of the A_0 mode at this frequency and its sensitivity to through-thickness cracks.

Table 3.3 summarizes all data sets recorded from Plate #3. Note that the initial set of six transducers consisted of bare PZT discs. During the first ten data sets, several soldered wires broke even though all wiring was strain-relieved. There was a gap between data sets 11 and 12, during which various backing compounds were investigated to provide more protection for the wiring without interfering with signal quality. A micro-bubble-filled epoxy mixture captured within a plastic sleeve was used for the second part of the Plate #3 test as well as for all subsequent tests.

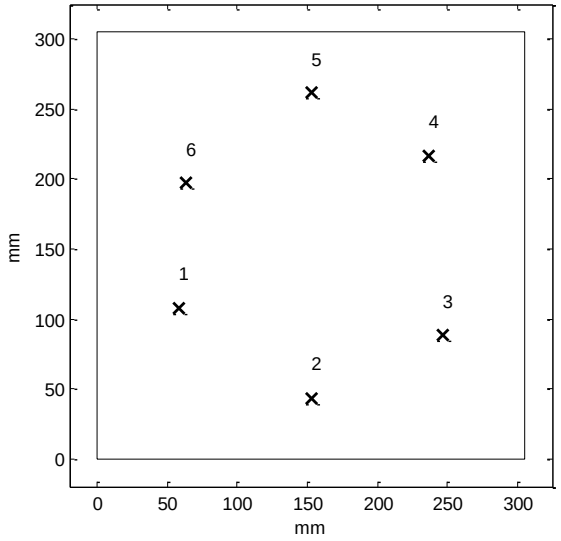

Figure 3.2. Sketch of the transducer pattern for Plate #3.

Table 3.2. Nominal transducer coordinates.

Transducer Number	*x* (mm)	*y* (mm)
1	58.1	108.0
2	152.5	43.5
3	246.9	88.0
4	236.9	217.0
5	152.5	261.5
6	63.1	197.0

Table 3.3. Data sets recorded for Plate #3.

Data Set	Cycles	Notes / Max Crack Length
2	0	5.1 mm hole drilled
3	0	Starter notch cut
4	1,000	No visible cracks
5	3,000	0.05” (1.3 mm)
6	4,000	0.1” (2.5 mm)
7	5,060	0.105” (2.7 mm)
8	6,060	0.11” (2.8 mm)
9	7,060	0.15” (3.8 mm)
10	9,060	0.21” (5.3 mm)
11	11,060	0.29” (7.4 mm)
All transducers removed and replaced after data set 11		
12	12,166	Fine load increments
13	12,166	0.344” (8.7 mm)
14	14,166	0.462” (11.7 mm)
15	15,166	0.544” (13.8 mm)
16	16,166	0.670” (17.0 mm)
17	16,667	0.772” (19.6 mm)
18	17,167	0.864” (22.0 mm)
19	17,667	1.004” (25.5 mm)

3.4 Plate #4

Plate #4 was instrumented with six transducers using two-component epoxy, and each transducer was further backed with a bubble-filled epoxy protection layer. A short “T” stiffener section was bonded to the plate with epoxy. Figure 3.3 shows a photograph of the plate mounted in the testing machine, and Table 3.4 summarizes the data recorded. The original goal was to fatigue the plate until the stiffener section disbonded, but after 1000 cycles with no change, it was decided to introduce artificial disbonds. Two methods were used: the first was to bond the stiffener with an initial disbond by inserting a piece of Teflon tape that was later removed, and the second was to use a knife to remove some of the bonding material.

Figure 3.3. Plate #4 mounted in the testing machine.

Table 3.4. Data sets recorded for Plate #4.

Data Set	Description
1	Pristine plate
2	Fully bonded stiffener section
3	After 1000 fatigue cycles
4	Pristine plate (stiffener removed)
5	Partially disbonded stiffener (tape inserted)
6	Fully bonded stiffener (disbond filled)
7	Pristine plate (stiffener removed)
8	Partially disbonded stiffener (tape inserted)
9	Partially disbonded stiffener (tape inserted)
10	Fully bonded stiffener (disbond filled)
11	Partially disbonded stiffener (with knife_

3.5 Plate #5

Plate #5, which is actually the same physical plate as Plate #4, can be seen in Figure 3.4 with the six attached transducers. Prior to fatiguing the specimen, a set of reference signals was recorded from the pristine sample. A through-hole measuring 5.1 mm in diameter was then drilled in the center of the plate, and a small starter notch was introduced on the left side of the hole as a site for crack initiation. Fatiguing continued until the largest crack was about 25 mm in length, and a total of 14 data sets were recorded. Fatigue cycles and observations of the cracks are summarized in Table 3.5, and photographs of the cracks are shown in Figure 3.4.

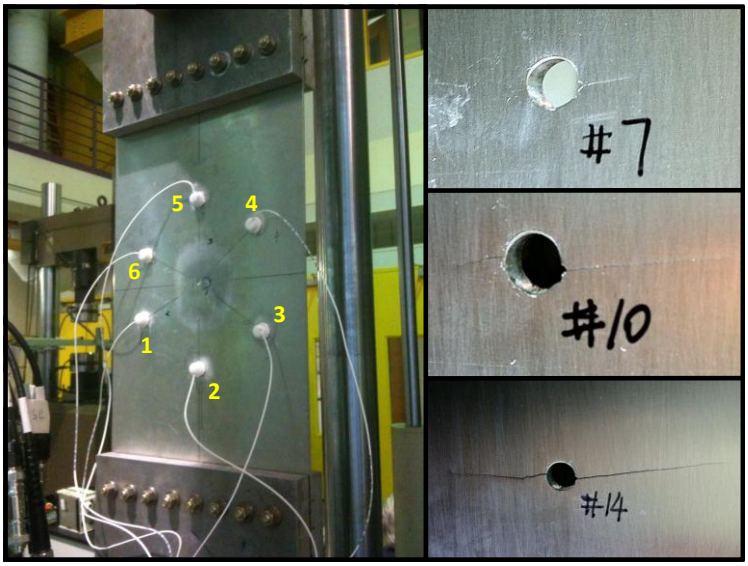

Figure 3.4. Plate #5 with attached transducers (numbered 1 through 6) mounted in the MTS machine (left), and photographs of fatigue cracks corresponding to data sets 7, 10 and 14 (right).

Table 3.5. Summary of fatiguing schedule and data acquired for Plate #5.

Data Set	Fatigue Cycles	Notes / Crack Lengths at Surface (mm)			
		Left Front	Left Back	Right Front	Right Back
1	0	Baseline, no hole, no notch			
2	0	5.1 mm diameter hole drilled			
3	0	Starter notch cut (left, front of hole)			
4	5,000	No visible cracks			
5	8,000	1.7	1.2	----	----
6	10,000	3.6	2.7	----	----
7	12,500	5.4	4.9	----	----
8	15,500	7.6	7.5	----	----
9	17,000	9.9	9.8	----	----
10	18,500	13.5	13.3	4.7	4.7
11	19,500	16.8	16.4	8.4	8.1
12	20,000	19.5	19.7	11.5	10.7
13	20,400	22.7	22.6	15.6	15.6
14	20,600	25.2	25.2	18.7	18.5

(Orientation relative to side with transducers)

After completion of fatiguing as summarized in the table above, Plate #5 was modified by gluing on a doubler, drilling holes, and adding/tightening/loosening bolts as per Table 3.6.

Table 3.6. Additional data acquired for Plate #5.

Data Set(s)	Description of Additional Plate Modifications
15-18	New baselines
19-21	Added glued on doubler
22-24	Center hole drilled through the doubler aligned with the plate center hole
25-27	Tightened bolt through the center hole
28-30	Loosened bolt through the center hole
31	Two side holes drilled, tightened bolts in all three holes
32	Tightened bolts in hole 1 and hole 2, no bolt in center hole
33	Loosened bolt in hole 1, tightened bolt in hole 2, no bolt in center hole
34	No bolt in hole 1 and hole 2, tightened bolt in center hole
35	No bolt in all three holes

3.6 Plate #6

A photograph of Plate #6 is shown in Figure 3.5, where a row of four holes can be seen within the transducer polygon. This plate was fatigued until the largest crack was about 0.5" long, and observations are reported as per Table 3.7. Upon termination of fatiguing, the plate

was insulated within a foam box with a heating pad to enable recording of load-dependent data at different temperatures. Recorded temperatures for an additional seven data sets are also found in Table 3.7.

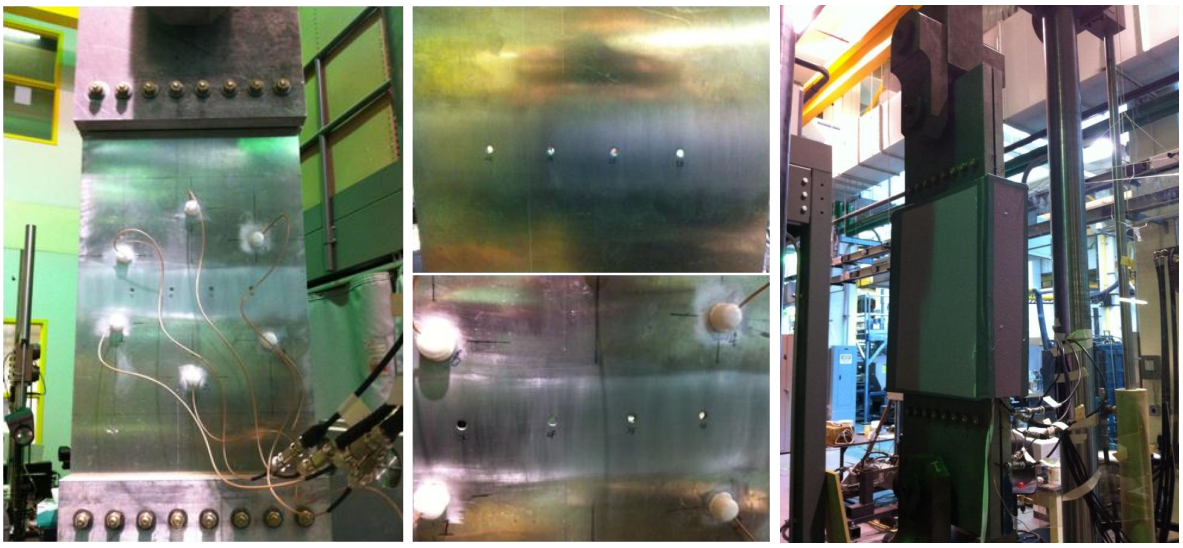

Figure 3.5. Plate #6 with attached transducers mounted in the MTS machine prior to fatiguing (left), showing close-ups of holes (center), and with foam box mounted (right). The holes on the transducer side (front of plate) are numbered 1 to 4 from left to right.

Table 3.7. Summary of fatiguing schedule and data acquired for Plate #6.

Data Set	Cycles	Notes / Crack Lengths at Surface (mm)									
		Hole 2 Front Left	Hole 2 Front Right	Hole 3 Front Left	Hole 3 Front Right	Hole 2 Back Left	Hole 2 Back Right	Hole 3 Back Left	Hole 3 Back Right Down	Hole 3 Back Right Up	Hole 4 Back Right
1	0	Baseline (no notch)									
2	0	Baseline (no notch) – One bad pair									
3	0	Baseline (no notch)									
4	0	Baseline (no notch)									
5	0	Two starter notches									
6	2,000	----	----	----	----	----	0.74	----	----	-----	----
7	2,500	----	----	----	----	-----	1.32	0.58	----	----	----
8	3,000	1.65	----	----	----	----	1.83	1.07	----	----	----
9	3,500	2.03	----	----	1.50	----	2.01	1.52	----	----	----
10	5,500	3.95	----	----	3.25	----	4.32	3.24	----	----	----
11	6,500	4.58	1.57	----	4.29	1.27	4.90	4.11	----	----	----

12	7,000	5.22	2.92	----	4.64	2.68	5.41	4.79	1.44	----	----
13	7,500	6.26	3.76	1.57	5.46	3.38	6.34	5.41	1.60	----	----
14	8,500	7.98	5.44	2.26	7.07	5.36	8.43	6.49	1.91	2.29	----
15	9,500	10.07	7.96	3.09	8.78	7.84	10.52	8.78	1.77	4.70	1.08
16	10,400	12.95	10.67	6.93	11.89	10.41	12.95	11.02	1.93	7.18	2.30
17	10,400	Data recorded at finer loading steps (2%)									
18	10,400	Temperature ~ 18.6°C									
19	10,400	Temperature ~ 21.3°C									
20	10,400	Temperature ~ 18.8°C									
21	10,400	Temperature ~ 20.1°C									
22	10,400	Temperature ~ 20.8°C									
23	10,400	Temperature ~ 20.8°C									
24	10,400	Temperature ~ 20.8°C									

(Orientation relative to side with transducers)

3.7 Plate #7

Plate #7 consisted of an initial drilled through-hole and an epoxy-bonded doubler as shown in Figure 3.6. It was fatigued until the largest crack was about 0.6" (15 mm) in length. Shortly before the test was terminated it was noticed that the doubler had become partially unbonded, at which point it was secured with bolts about 1" from each end. Observations and data acquired are summarized in Table 3.8.

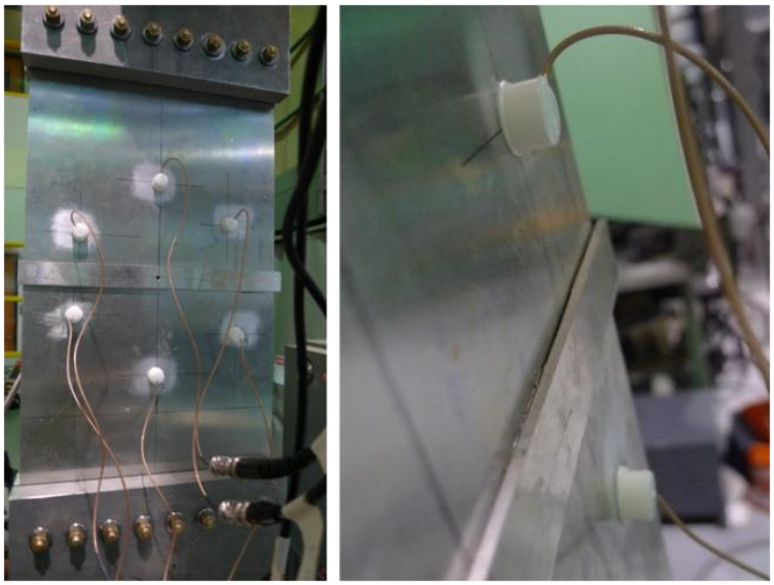

Figure 3.6. Plate #7 with bonded doubler and drilled through-hole.

Table 3.8. Summary of fatiguing schedule and data acquired for Plate #7.

Data Set	Fatigue Cycles	Crack Lengths (mm)		Data Description
		Left	Right	
1	0	---	---	Baseline with the doubler and center hole
2	0	---	---	Starter notch cut (left, front of hole)
2A	0	---	---	Data recorded at finer loading steps (2%)
3	5,000	1.5	---	Initial crack observed at the left side of center hole
4	6,500	2.6	---	
5	9,000	4.8	---	Possible transducer bonding issues at high loads
6	11,000	6.8	0.9	
7	13,000	9.1	2.7	Noticed disbond at the right edge of the doubler
8	14,000	11.5	4.6	
9	14,000	11.5	4.6	Secured doubler with bolts 1” from each end
10	14,000	11.5	4.6	
11	15,000	14.02	6.71	Continued fatiguing
12	15,700	15.46	8.50	

(Orientation relative to side with transducers)

3.8 Plate #8

Plate #8 was similar to Plate #7 except the doubler was initially bolted to the plate on either end as shown in Figure 3.7. Observations and data acquired are summarized in Table 3.9. Note that transducers #1 and #6 were removed and replaced after acquisition of data set 5, and also that all bolts were removed after data set 5.

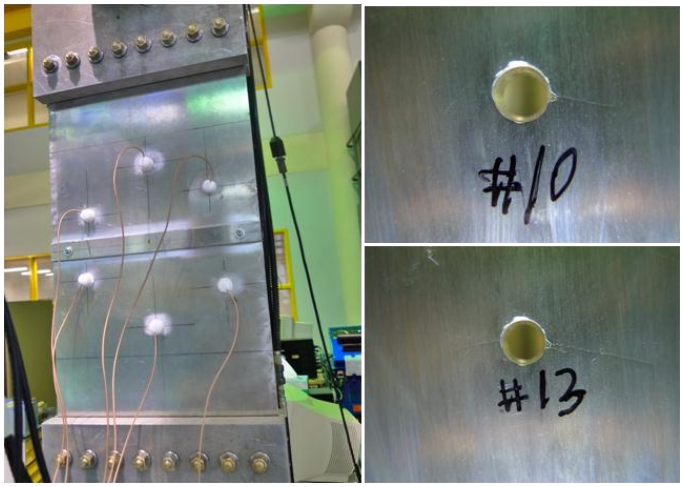

Figure 3.7. Plate #8 with bonded doubler, central drilled through-hole, and side through-holes with bolts installed.

Table 3.9. Summary of fatiguing schedule and data acquired for Plate #8.

Data Set	Fatigue Cycles	Crack Lengths (mm)		Data Description
		Left	Right	
1	0	---	---	Baseline with tightened bolts through side hole1 and 2, no bolt through center hole
2	0	---	---	One partial notch only on the plate
3	3000	---	---	
4	3000	---	---	
5	3000	---	---	
6	3000	---	---	Transducers #1 and #6 replaced; all bolts removed.
7	5000	1.07	---	Initial crack appears
8	7000	2.67	---	
9	10,000	5.03	---	
10	11,000	5.94	1.12	Second crack appears
11	13,000	7.94	2.16	
12	14,000	9.88	3.73	
13	15,000	11.73	5.61	Fatigue test ends

(Orientation relative to side with transducers)

4. Theory of Acoustoelastic Lamb Waves

In this section the theory of acoustoelastic Lamb wave propagation in a homogeneous and initially isotropic plate is developed for an applied homogeneous biaxial stress by combining the theories of bulk wave acoustoelasticity and anisotropic guided wave propagation. The resulting analytical equations are solved numerically to show the anisotropic changes in dispersion for various applied stresses, and these changes are validated via experiments using an aluminum plate.

4.1 Review of Bulk Wave Acoustoelasticity

The theory of bulk wave acoustoelasticity is first reviewed following the development of Pao and Gamer [33]. Referring to Figure 4.1, a body is deformed from its unstressed, or natural, state, to a statically deformed, or initial, state; the final state is that of wave motion superposed on the initial state. Coordinates $\boldsymbol{\xi}$ refer to a material point in the natural state, coordinates $\mathbf{X}$ refer to a material point in the initial state, and coordinates $\mathbf{x}$ to a material point in the final state. Deformations between the various states; i.e., natural to initial, natural to final, and initial to final, are given by $\mathbf{u}^{\mathrm{i}}$, $\mathbf{u}^{\mathrm{f}}$, and $\mathbf{u}$, respectively:

$$\begin{aligned} \mathbf{u}^{\mathrm{i}}(\boldsymbol{\xi}) &= \mathbf{X} - \boldsymbol{\xi}, \\ \mathbf{u}^{\mathrm{f}}(\boldsymbol{\xi}, t) &= \mathbf{x} - \boldsymbol{\xi}, \\ \mathbf{u}(\boldsymbol{\xi}, t) &= \mathbf{x} - \mathbf{X} = \mathbf{u}^{\mathrm{f}}(\boldsymbol{\xi}, t) - \mathbf{u}^{\mathrm{i}}(\boldsymbol{\xi}). \end{aligned} \tag{4.1}$$

To describe wave propagation in a stressed medium, the equation for **u,** the incremental deformation between the initial and final states in a pre-stressed medium must be obtained.

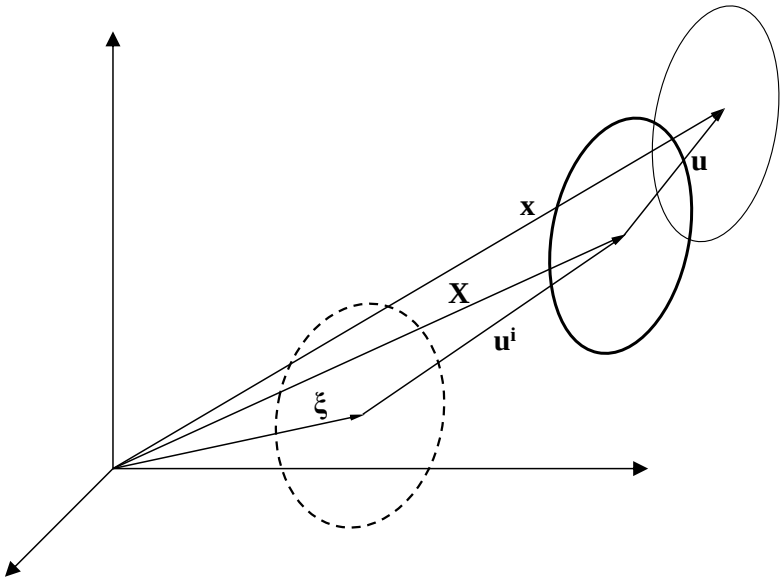

Figure 4.1. Deformation of a body from its natural (undeformed) state $\boldsymbol{\xi}$ to an initial state of static deformation $\mathbf{X}$ to a final state of wave motion $\mathbf{x}$.

Keeping the same convention as is used in [33], Greek subscripts indicate that the quantities are expressed in terms of the natural, or unstressed coordinates. Lagrangian strain tensors in the initial and final states are,

$$E^{\mathrm{i}}_{\alpha\beta} = \frac{1}{2}\left(\frac{\partial u^{\mathrm{i}}_{\alpha}}{\partial \xi_{\beta}} + \frac{\partial u^{\mathrm{i}}_{\beta}}{\partial \xi_{\alpha}} + \frac{\partial u^{\mathrm{i}}_{\lambda}}{\partial \xi_{\alpha}} \frac{\partial u^{\mathrm{i}}_{\lambda}}{\partial \xi_{\beta}} \right),$$
$$E^{\mathrm{f}}_{\alpha\beta} = \frac{1}{2}\left(\frac{\partial u^{\mathrm{f}}_{\alpha}}{\partial \xi_{\beta}} + \frac{\partial u^{\mathrm{f}}_{\beta}}{\partial \xi_{\alpha}} + \frac{\partial u^{\mathrm{f}}_{\lambda}}{\partial \xi_{\alpha}} \frac{\partial u^{\mathrm{f}}_{\lambda}}{\partial \xi_{\beta}} \right). \tag{4.2}$$

Note that summation over repeated indices is implied here and in subsequent equations. If the wave motion is small compared to the initial predeformation, the incremental strain tensor between the initial and final states is given approximately by,

$$E_{\alpha\beta} = E^{\mathrm{f}}_{\alpha\beta} - E^{\mathrm{i}}_{\alpha\beta} = \frac{1}{2}\left(\frac{\partial u_{\alpha}}{\partial \xi_{\beta}} + \frac{\partial u_{\beta}}{\partial \xi_{\alpha}} + \frac{\partial u^{\mathrm{i}}_{\lambda}}{\partial \xi_{\alpha}} \frac{\partial u_{\lambda}}{\partial \xi_{\beta}} + \frac{\partial u^{\mathrm{i}}_{\lambda}}{\partial \xi_{\beta}} \frac{\partial u_{\lambda}}{\partial \xi_{\alpha}} \right). \tag{4.3}$$

If it is assumed that the material is hyperelastic, the Lagrangian strain tensor can be related to the second Piola-Kirchoff stress tensor via a constitutive equation; here only the second and third order elastic constants are retained:

$$T^{\mathrm{i}}_{\alpha\beta} = C_{\alpha\beta\gamma\delta} E^{\mathrm{i}}_{\gamma\delta} + \tfrac{1}{2} C_{\alpha\beta\gamma\delta\varepsilon\eta} E^{\mathrm{i}}_{\gamma\delta} E^{\mathrm{i}}_{\varepsilon\eta},$$
$$T^{\mathrm{f}}_{\alpha\beta} = C_{\alpha\beta\gamma\delta} E^{\mathrm{f}}_{\gamma\delta} + \tfrac{1}{2} C_{\alpha\beta\gamma\delta\varepsilon\eta} E^{\mathrm{f}}_{\gamma\delta} E^{\mathrm{f}}_{\varepsilon\eta}. \tag{4.4}$$

Incremental stresses and strains between the initial and final states are related by subtracting the above equations and discarding higher order terms,

$$T_{\alpha\beta} = C_{\alpha\beta\gamma\delta} E_{\gamma\delta} + C_{\alpha\beta\gamma\delta\varepsilon\eta} e^{\mathrm{i}}_{\gamma\delta} e_{\varepsilon\eta} \tag{4.5}$$

The infinitesimal initial and incremental strain tensors are,

$$e^{\mathrm{i}}_{\gamma\delta} = \frac{1}{2}\left(\frac{\partial u^{\mathrm{i}}_{\gamma}}{\partial \xi_{\delta}} + \frac{\partial u^{\mathrm{i}}_{\delta}}{\partial \xi_{\gamma}} \right), \quad e_{\varepsilon\eta} = \frac{1}{2}\left(\frac{\partial u_{\varepsilon}}{\partial \xi_{\eta}} + \frac{\partial u_{\eta}}{\partial \xi_{\varepsilon}} \right) \tag{4.6}$$

Equation (4.5) is thus the incremental constitutive equation.

Consider the equation of equilibrium for the static predeformation and the equation of motion for the final state,

$$\frac{\partial}{\partial \xi_{\beta}} \left[T^{\mathrm{i}}_{\beta\alpha} + T^{\mathrm{i}}_{\beta\gamma} \frac{\partial u^{\mathrm{i}}_{\alpha}}{\partial \xi_{\gamma}} \right] = 0, \quad \frac{\partial}{\partial \xi_{\beta}} \left[T^{\mathrm{f}}_{\beta\alpha} + T^{\mathrm{f}}_{\beta\gamma} \frac{\partial u^{\mathrm{f}}_{\alpha}}{\partial \xi_{\gamma}} \right] = \rho^{0} \frac{\partial^{2} u^{\mathrm{f}}_{\alpha}}{\partial t^{2}} \tag{4.7}$$

where ρ^0 is the density in the natural state. The equation of motion for the incremental displacement is obtained by subtracting these two equations and neglecting one higher order term [33]. The resulting equation of motion for the incremental displacement is,

$$\frac{\partial}{\partial \xi_\beta}\left[T_{\alpha\beta} + T^{\mathrm{i}}_{\beta\gamma}\frac{\partial u_\alpha}{\partial \xi_\gamma} + T_{\beta\gamma}\frac{\partial u^{\mathrm{i}}_\alpha}{\partial \xi_\gamma}\right] = \rho^0 \frac{\partial^2 u_\alpha}{\partial t^2} \tag{4.8}$$

Further simplification is possible by assuming that both the material and the static predeformation are homogeneous, and then substituting Eq. (4.5), the incremental constitutive equation, into Eq. (4.8). The resulting equation of motion for the incremental displacement is,

$$A_{\alpha\beta\gamma\delta}\frac{\partial^2 u_\gamma}{\partial \xi_\beta \partial \xi_\delta} = \rho^0 \frac{\partial^2 u_\alpha}{\partial t^2} \tag{4.9}$$

where

$$A_{\alpha\beta\gamma\delta} = C_{\alpha\beta\gamma\delta} + C_{\beta\delta\varepsilon\eta}e^{\mathrm{i}}_{\varepsilon\eta}\delta_{\alpha\gamma} + C_{\alpha\beta\lambda\delta}\frac{\partial u^{\mathrm{i}}_\gamma}{\partial \xi_\lambda} + C_{\lambda\beta\gamma\delta}\frac{\partial u^{\mathrm{i}}_\alpha}{\partial \xi_\lambda} + C_{\alpha\beta\gamma\delta\varepsilon\eta}e^{\mathrm{i}}_{\varepsilon\eta} \tag{3.10}$$

Equation (4.9) appears almost identical to the usual elastic wave equation, but it should be noted that **A** does not have the same symmetries as the stiffness tensor **C.** The only symmetry is $A_{ijkl} = A_{klij}$; in general, $A_{ijkl} \neq A_{jikl} \neq A_{ijlk}$.

4.2 Theory of Lamb Wave Acoustoelasticity

Development of the theory for propagation of Lamb waves in pre-stressed plates requires combining the equation of motion and constitutive equation developed for bulk waves in the previous section with the theory for Lamb wave propagation in an anisotropic plate. The equations derived in the process closely match those of Nayfeh and Chimenti [34] for anisotropic Lamb waves.

The geometry and coordinate system used in this paper are illustrated in Figure 4.2. Referring to the figure, the initial stresses are specified in the primed coordinate system, and a Lamb wave propagating along any arbitrary angle φ from the x_1' direction is considered. The unprimed coordinate system is rotated through the same angle φ to form the primed coordinate system, and analysis is performed in the unprimed system to simplify the mathematics. For an applied biaxial stress along the x_1' and x_2' directions, the initial stress tensor can be written as,

$$\mathbf{T}' = \begin{bmatrix} \sigma_{11} & 0 & 0 \\ 0 & \sigma_{22} & 0 \\ 0 & 0 & 0 \end{bmatrix} \tag{4.11}$$

It is expressed in the unprimed system via a rotational transformation,

$$T^{\mathrm{i}}_{ij} = \beta_{im}\beta_{jn}T^{\mathrm{i}}_{mn}{}' \tag{4.12}$$

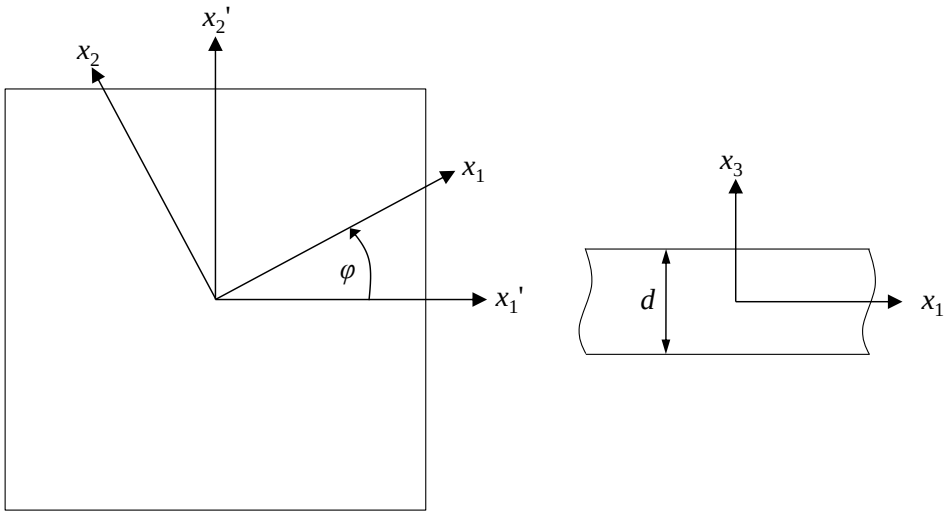

Figure 4.2. Geometry for Lamb wave propagation in a pre-stressed plate. Stresses are applied along the principal directions in the primed coordinate system, and Lamb waves propagate along the x_1 axis.

where β_{ij} is the cosine of the angle between the x_i and the x_j' axes. For convenience, in this and subsequent equations, lower case Roman subscripts are used instead of Greek subscripts to represent quantities in the natural coordinate system. In particular, all quantities are expressed in terms of the natural coordinates; for example, x_j is used instead of ξ_j.

Assuming that the initial strains are small, the constitutive equation relating initial stresses and strains given in Eq. (4.4) can be simplified to,

$$T_{ij}^{\mathrm{i}} = C_{ijkl} e_{kl}^{\mathrm{i}} \tag{4.13}$$

For a given applied stress field, the strains in the unprimed system can be calculated by inverting this equation. From this point forward, all quantities are expressed in the unprimed system.

The **A** tensor as given by Eq. (4.10) can be simplified further by noting that the displacement derivatives can be expressed in terms of strains because for the stresses given in Eq. (4.11), the rotation terms are zero for all angles φ. Thus,

$$\frac{\partial u_j^{\mathrm{i}}}{\partial x_k} = e_{jk}^{\mathrm{i}} \tag{4.14}$$

and

$$A_{ijkl} = C_{ijkl} + C_{jlmn} e_{mn}^{\mathrm{i}} \delta_{ik} + C_{ijml} e_{km}^{\mathrm{i}} + C_{mjkl} e_{im}^{\mathrm{i}} + C_{ijklmn} e_{mn}^{\mathrm{i}} \tag{4.15}$$

The incremental stress-strain relation of Eq. (4.5) can similarly be simplified to

$$T_{ij} = B_{ijkl}\frac{\partial u_k}{\partial x_l}, \quad B_{ijkl} = C_{ijkl} + C_{ijml}e^{\mathrm{i}}_{km} + C_{ijklmn}e^{\mathrm{i}}_{mn} \tag{4.16}$$

Acoustoelastic Lamb wave propagation for a homogeneous and biaxial stress field requires solving the wave equation for the incremental displacements as given by Eq. (4.9) subject to stress-free boundary conditions at $x_3 = \pm d/2$ with the tensor **A** given by Eq. (4.15) and the stresses given by Eq. (4.16). This problem differs from Lamb wave propagation in anisotropic media in two regards: (1) as previously noted, the tensor **A** does not have the same symmetries as the stiffness tensor **C**, and (2) the boundary conditions at the plate surfaces are now written in terms of the incremental displacements.

Following [34], the approach to solving this problem is to assume solutions of the form,

$$u_j = U_j e^{i\xi(x_1 + \alpha x_3 - ct)} \tag{4.17}$$

where ξ is the wavenumber in the x_1 direction, c is the phase velocity along the x_1 axis and α is the ratio of x_3 to x_1 wavenumbers. For a specific value of c, these solutions correspond to up-going and down-going bulk waves in the $x_1 - x_3$ plane of the plate, which are then summed together to form the Lamb wave. This approach is sometimes referred to as the partial wave technique [35].

Substitution of Eq. (4.17) into Eq. (4.9) yields a form of the Christoffel equations,

$$K_{mn}(\alpha)U_n = 0, \tag{4.18}$$

where the parameters K_{mn} are given by,

$$\begin{aligned}
K_{11} &= c^2\rho^0 - A_{1111} - \alpha^2 A_{1313}, \quad & K_{12} &= K_{21} = -A_{1112} - \alpha^2 A_{1323}, \\
K_{22} &= c^2\rho^0 - A_{1212} - \alpha^2 A_{2323}, \quad & K_{13} &= K_{31} = -\alpha(A_{1133} + A_{1331}), \\
K_{33} &= c^2\rho^0 - A_{1313} - \alpha^2 A_{3333}, \quad & K_{23} &= K_{32} = -\alpha(A_{1233} + A_{1332}).
\end{aligned} \tag{4.19}$$

It can be seen that K_{mn}=K_{nm}. For existence of non-trivial solutions for the displacement amplitudes U_n, the determinant of the K matrix must go to zero, which produces a 6th order equation in α with six solutions α_q, q = 1…6. The coefficients of the odd powers of α are all zero, resulting in a cubic equation in α^2 given by

$$P_6\alpha^6 + P_4\alpha^4 + P_2\alpha^2 + P_0 = 0, \tag{4.20}$$

where the coefficients can be found in [36]. For a specific value of the Lamb wave phase velocity c, solving this cubic equation yields six values of α, which correspond to three up-going bulk waves and three down-going bulk waves.

The next step is to satisfy the stress-free boundary conditions on the plate surfaces as per Eq. (4.16). The approach taken here is similar to that taken in [34], and consists of constructing displacement ratios of U_2 and U_3 to U_1 for each of the six values of α,

$$V_q = \frac{U_{2q}}{U_{1q}}, \quad W_q = \frac{U_{3q}}{U_{1q}}, \quad q = 1,2\ldots 6. \tag{3.21}$$

Equation (4.18) enables each ratio to be expressed as a function of the K_{mn} and the corresponding α_q. The total displacement field of the Lamb wave is the sum of the displacements of the six partial waves,

$$\{u_1, u_2, u_3\} = \sum_{q=1}^{6} \{1, V_q, W_q\} U_{1q} e^{i\xi(x_1 + \alpha_q x_3 - ct)}. \tag{4.22}$$

Similarly, an expression for the stresses can be derived by substituting Eq. (4.22) into Eq. (4.16). The three stress components in the x_3 direction are then written as a sum of stresses due to the six individual bulk waves,

$$\{T_{33}, T_{13}, T_{23}\} = \sum_{q=1}^{6} i\xi \{D_{1q}, D_{2q}, D_{3q}\} U_{1q} e^{i\xi(x_1 + \alpha_q x_3 - ct)} \tag{4.23}$$

where the parameters D_{mq} are given by,

$$\begin{aligned} D_{1q} &= B_{3311} + B_{3312} V_q + \alpha_q B_{3333} W_q, \\ D_{2q} &= \alpha_q \left(B_{1313} + B_{1323} V_q \right) + B_{1331} W_q, \\ D_{3q} &= \alpha_q \left(B_{1323} + B_{2323} V_q \right) + B_{1332} W_q. \end{aligned} \tag{4.24}$$

Applying the stress-free boundary conditions at the surface of the plate requires setting T_{13}, T_{23} and T_{33} to zero at $x_3 = \pm d/2$, and yields six equations in terms of the six displacement amplitudes, U_{1q}, of the six partial waves, q = 1,2…6. The determinant of coefficients must go to zero to obtain nontrivial solutions for these six displacement amplitudes. This determinant is,

$$\begin{vmatrix} D_{11}E_1 & D_{12}E_2 & D_{13}E_3 & D_{14}E_4 & D_{15}E_5 & D_{16}E_6 \\ D_{21}E_1 & D_{22}E_2 & D_{23}E_3 & D_{24}E_4 & D_{25}E_5 & D_{26}E_6 \\ D_{31}E_1 & D_{32}E_2 & D_{33}E_3 & D_{34}E_4 & D_{35}E_5 & D_{36}E_6 \\ D_{11}\tilde{E}_1 & D_{12}\tilde{E}_2 & D_{13}\tilde{E}_3 & D_{14}\tilde{E}_4 & D_{15}\tilde{E}_5 & D_{16}\tilde{E}_6 \\ D_{21}\tilde{E}_1 & D_{22}\tilde{E}_2 & D_{23}\tilde{E}_3 & D_{24}\tilde{E}_4 & D_{25}\tilde{E}_5 & D_{26}\tilde{E}_6 \\ D_{31}\tilde{E}_1 & D_{32}\tilde{E}_2 & D_{33}\tilde{E}_3 & D_{34}\tilde{E}_4 & D_{35}\tilde{E}_5 & D_{36}\tilde{E}_6 \end{vmatrix} = 0, \tag{4.25}$$

where $E_q = e^{i\xi\alpha_q d/2}$ and $\tilde{E}_q = e^{-i\xi\alpha_q d/2}$. After several number of row and column operations, Eq. (4.25) decouples into two equations,

$$f_s(\omega, c) = D_{11}G_1 \cot(\gamma\alpha_1) + D_{13}G_3 \cot(\gamma\alpha_3) + D_{15}G_5 \cot(\gamma\alpha_5) = 0, \tag{4.26}$$

$$f_a(\omega,c) = D_{11}G_1 \tan(\gamma\alpha_1) + D_{13}G_3 \tan(\gamma\alpha_3) + D_{15}G_5 \tan(\gamma\alpha_5) = 0. \quad (4.27)$$

The first equation corresponds to the symmetric modes and the second one corresponds to the antisymmetric modes. In both equations $\gamma = \xi d/2 = \omega d/(2c)$, where ω is the angular frequency. The parameters G_m are given as

$$G_1 = D_{23}D_{35} - D_{33}D_{25},\ G_3 = D_{31}D_{25} - D_{21}D_{35},\ G_5 = D_{21}D_{33} - D_{31}D_{23} \quad (4.28)$$

Solving Eqs. (4.26) and (4.27) yields the dispersion curves relating phase velocity and angular frequency for the symmetric and antisymmetric Lamb wave modes, respectively. Solving these equations is not trivial; a description of the numerical method is given in [36].

4.3 Selected Analytical Results

This section presents dispersion curves generated by solving Eqs. (4.26) and (4.27) numerically for specific materials. The first material considered is 6061-T6 aluminum, which was selected to match subsequent experiments. Material constants used are listed in Table 4.1, and the third order elastic constants were taken from [37]. It should be noted that although third order elastic constants are available in the literature for several aluminum alloys [37,38,39], their values are quite variable. It is not clear whether the variability is caused by differences in experimental methods or actual material variations. The second material considered was steel because of its widespread use. Unfortunately third order elastic constants for steel are not widely reported; the ones used here are also summarized in Table 4.1 and are for Hecla 37 steel [39].

Table 4.1. Material constants for 6061-T6 aluminum [24,37] and Hecla 37 steel [39].

Parameter	Value *6061-T6 AL*	Value *Hecla 37 Steel*	Units
λ	54.308	111	GPa
μ	27.174	821	GPa
l	-281.5	-461	GPa
m	-339.0	-636	GPa
n	-416.0	-708	GPa
ρ^0	2704	7823	kg/m^3

Figures 4.3(a) and 4.3(b) present the family of symmetric and antisymmetric dispersion curves for aluminum under a uniaxial stress of $\sigma_{11} = 100$ MPa and for waves propagating at an angle of 45° to the stress direction; note that the SH_0 mode is not shown. To illustrate the variation of the function values as they go to zero, $\log|f_s(\omega,c)|$ and $\log|f_a(\omega,c)|$ have been plotted in the background for both plots. These dispersion curves appear virtually identical to the ones obtained using the Rayleigh-Lamb equations for the no-load case since the velocity changes due to the applied stress are not noticeable at this scale. These and all subsequent curves refer to phase velocities computed in the natural, or undeformed, coordinate system, which is consistent with the derivations of Section 4.2.

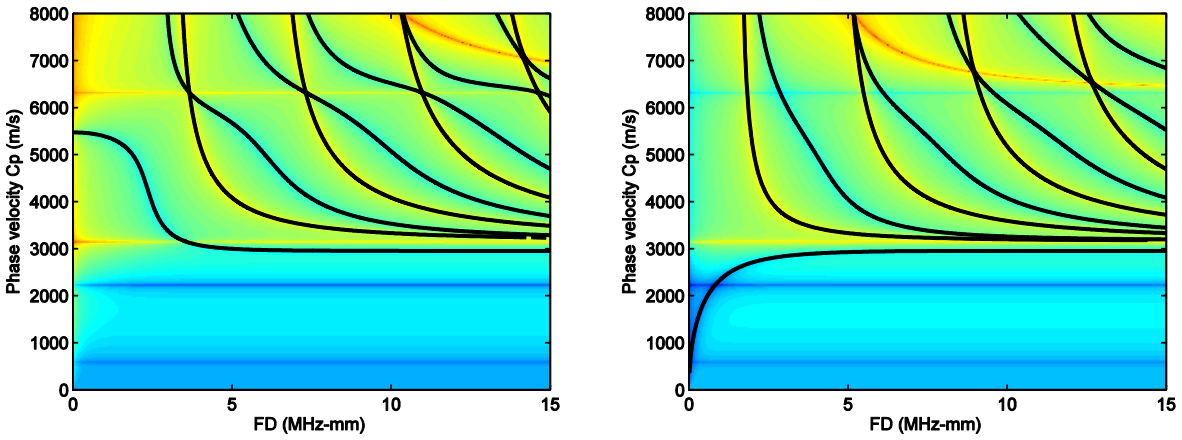

Figure 4.3. Dispersion curves for waves propagating in aluminum at an angle of 45° to an applied uniaxial applied stress of 100 MPa. (a) Symmetric modes, and (b) anti-symmetric modes.

Figure 4.4 presents the variation of phase velocity of the S_0 mode at 250 kHz with angle for a range of biaxial stresses and for a plate thickness of 6.35 mm. Note that the load is applied along the *y* axis so that waves propagating along the direction of applied load are at 90°. An interesting prediction made by this plot is that the angle at which the phase velocity change is zero (about 27°) is independent of stress. It can also be seen that at a specific angle, the change of phase velocity is linear with load.

Figure 4.5 compares phase velocity changes as a function of frequency for the S_0 mode at varying uniaxial stresses σ_{11} for waves propagating along the loading direction. This plot shows large changes in phase velocity for lower frequencies that reduce and flatten in the high frequency region. It is evident that the change of phase velocity is linear with load at a specific frequency.

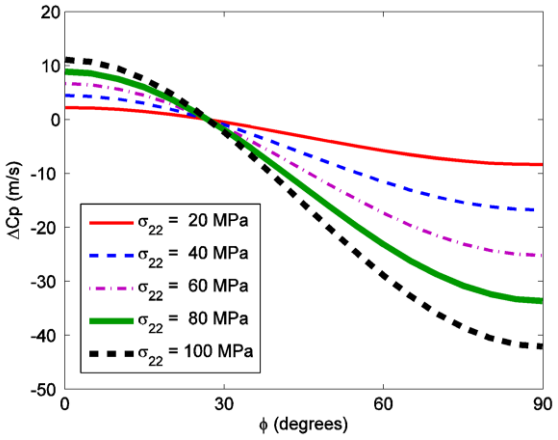

Figure 4.4. Change of phase velocity for the S_0 mode at 250 kHz for various loads and angles.

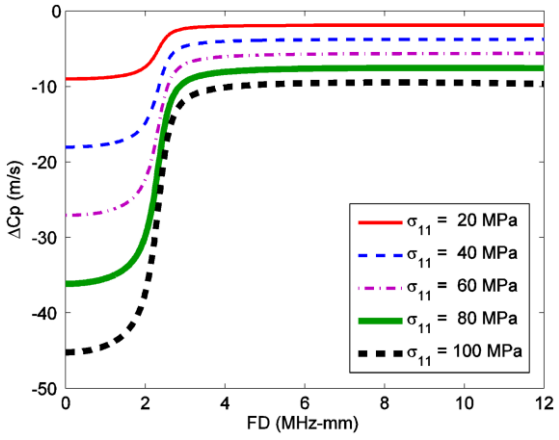

Figure 4.5. Change of phase velocity for the S_0 mode for propagation along the loading direction.

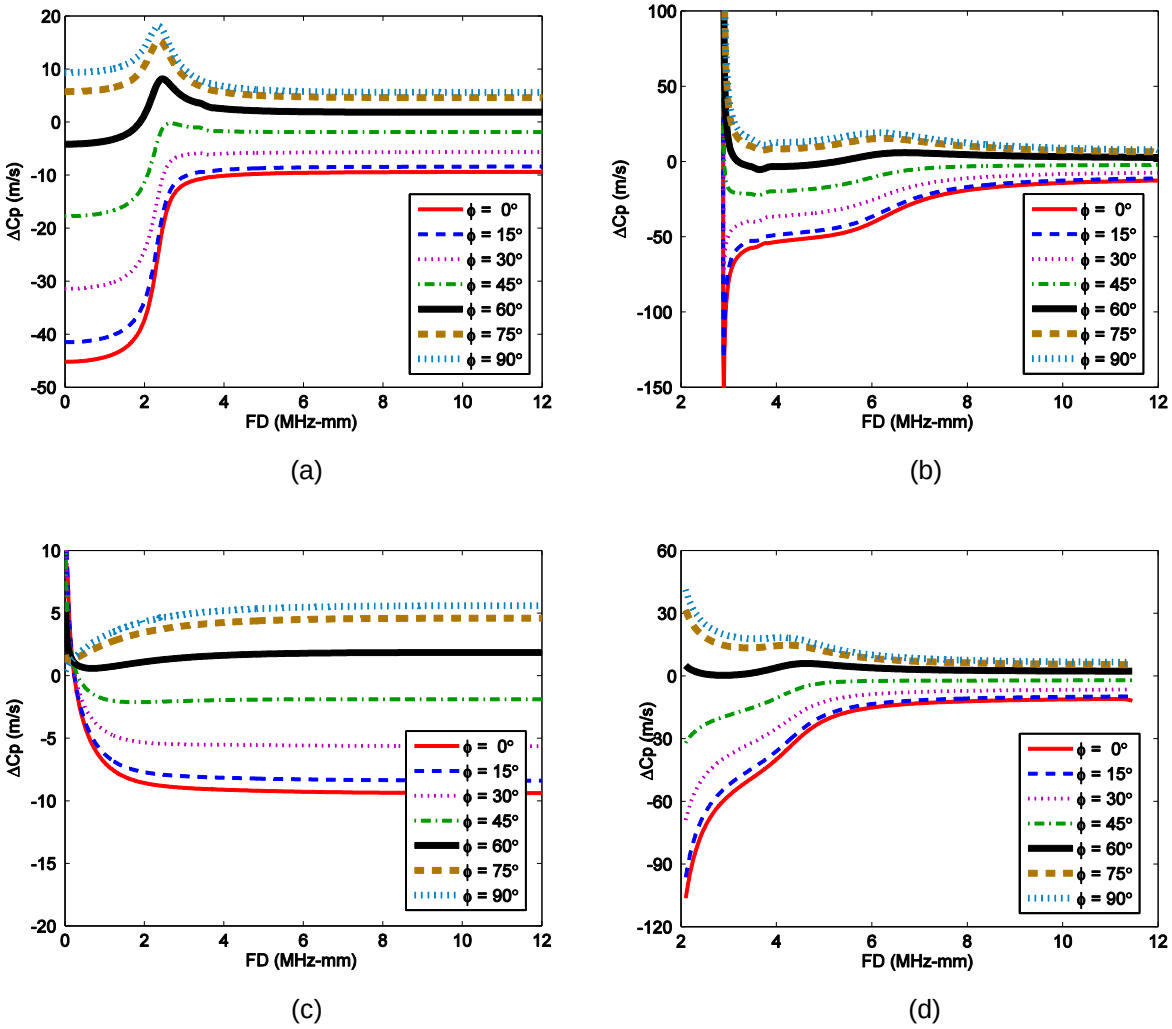

Figure 4.6. Changes in phase velocity versus frequency for waves propagating in aluminum at various angles to a 100 MPa uniaxial load applied at 0°. (a) S_0, (b) S_1, (c) A_0, and (d) A_1 mode.

Figures 4.6(a) through 4.6(d) compare the phase velocity change with frequency at different angles for the S_0, S_1, A_0 and A_1 Lamb wave modes, respectively. The plot for A_0 is particular interesting in that it predicts isotropic phase velocities for the A_0 mode for the frequency-thickness product of approximately 187 MHz-mm, although at this frequency the velocity change from the unstressed condition is non-zero. This phenomenon should not be confused as isotropic wave propagation since the group velocity at this frequency is certainly angle dependent.

Figure 4.7 is a plot of the S_0 and SH_0 modes for an applied uniaxial stress of 100 MPa and propagation at 45° to the loading direction. The S_0 and SH_0 modes split and form two new continuous modes at their original point of intersection (from the unstressed case) when a stress is applied. Because of symmetry, this splitting does not occur at either 0° or 90°, and is similar to that which also occurs for anisotropic materials [40,41]. Other symmetric and antisymmetric modes similarly interact with higher order SH modes. In the earlier plots, this splitting was not shown to facilitate comparison of the perturbed modes to those of the unstressed material.

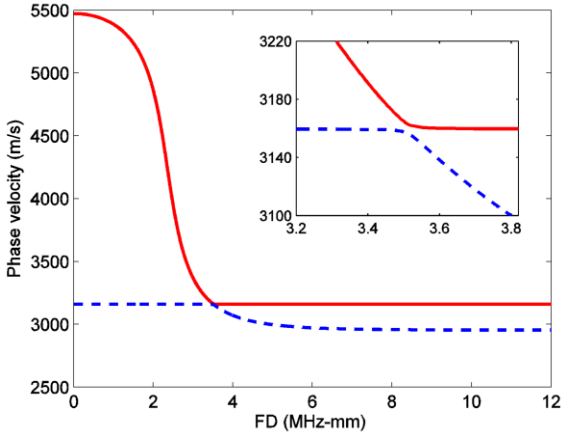

Figure 4.7. Splitting of the S_0 and SH_0 modes for propagation at 45° to the loading direction.

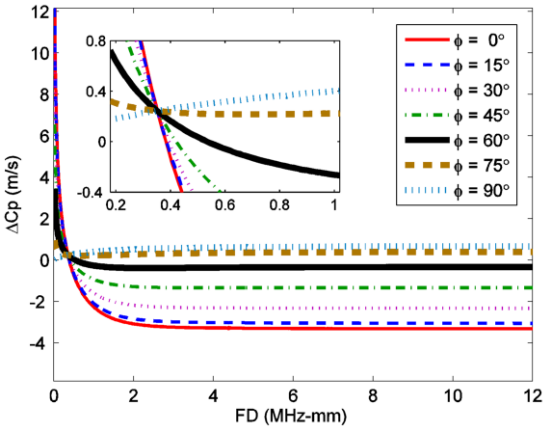

Figure 4.8. Change in phase velocity for the A_0 mode in steel propagating at an angle to an applied uniaxial load.

Figure 4.8 shows the A_0 mode for steel under a uniaxial stress of $\sigma_{11} =$ 200 MPa. Steel also shows the isotropic phase velocities at lower frequencies for the A_0 mode at a frequency-thickness product of approximately 0.35 MHz-mm. Additional results for steel are not shown because they are qualitatively the same as for aluminum.

4.4 Experimental Results

Data were analyzed from Plate #2, which were obtained as described in Section 3.2. The following three frequencies were utilized to produce an unambiguous first arrival of the indicated Lamb wave mode: 250 kHz (S_0 mode), 400 kHz (A_1 mode), and 600 kHz (S_1 mode). Signals were recorded from 9 of the 45 possible transmit-receive pairs as shown in Figure 3.1(b) at eleven uniaxial loads (0 MPa to 57.5 MPa in steps of 5.75 MPa).

Time shifts were measured by identifying a zero crossing in the center of each direct arrival echoes, and then tracking that zero crossing as a function of applied uniaxial load. For a particular time shift, the corresponding change in phase velocity can be calculated as,

$$\Delta c_p = -\frac{c_p^2 \Delta t}{d}. \tag{4.29}$$

Although there is also a change of distance, it does not appear in Eq. (4.29) because all computations are in the natural, or undeformed, coordinate system.

Figure 4.9(a) shows the linear variation of the changes in phase velocity with stress for propagation of the three Lamb wave modes along the direction of applied stress (the *y* axis). The results are further corroborated by experimental measurements using transducer #1 as a transmitter and transducer #6 as a receiver, which show similar linear changes in phase velocity. Figure 4.9(b) shows the variation of phase velocity with angle for the case of uniaxial stress of $\sigma_{22} = 57.5$ MPa. The experimental values were obtained by fitting a line to the time shift versus load curve, and then calculating the time shift at 57.5 MPa from the linear fit. Both theoretical and experimental data closely follow a sinusoidal profile. The systematic differences between theory and experiment are probably due to the well-known difficulties in accurately obtaining

third order elastic constants. The linear dependence of phase velocity changes with load and sinusoidal dependence with angle of propagation are expected since that is the case for bulk waves, but validation of both characteristics is reassuring.

Figure 4.10, which is analogous to Figure 4.9(b), shows the variation of phase velocity with angle but with the theoretical curves calculated using different (but plausible) values for the TOECs. For these values, selected as l = -181 MPa, m = -289 MPa, and n = -336 MPa, the S_0 and A_1 theoretical curves are in excellent agreement with the experimental data, and the S_1 curve is in reasonable agreement. This significant improvement not only supports the speculation that the deviation between theory and experiment is largely explained by errors in TOECs, it also suggests that guided wave measurements could be used to estimate TOECs.

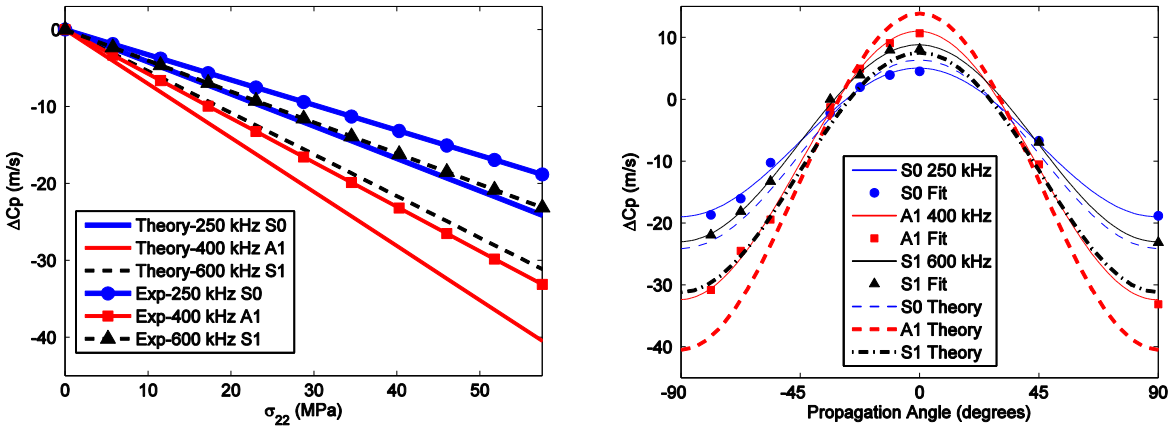

Figure 4.9. Comparison of theory and experiment for propagation in aluminum for a uniaxial load at 90°. (a) Changes in phase velocity versus load for waves propagating at an angle of 90°, and (b) changes in phase velocity versus propagation angle for an applied load of 57.5 MPa.

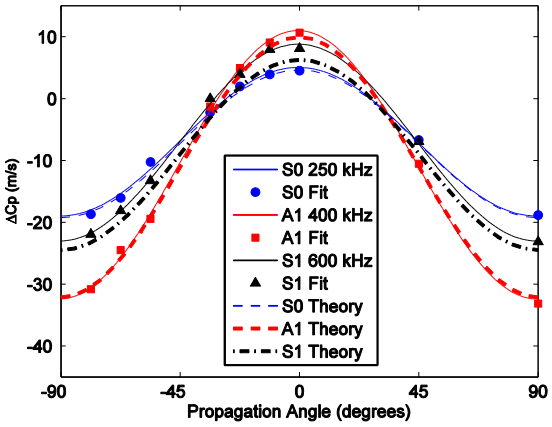

Figure 4.10. Comparison of theory and experiment for an applied uniaxial load of 57.5 MPa at 90° using modified TOECs (l = -181 GPa, m = -289 GPa, and n = -336 GPa).

4.5 Section Summary: Lamb Wave Acoustoelasticity

Described here is the theory for acoustoelastic Lamb wave propagation, and both numerical and experimental results are shown for the multiple Lamb wave modes. Unlike bulk waves, the acoustoelastic behavior is frequency dependent. Experimental results that measure changes in phase velocity as a function of both load and propagation angle agree reasonably well with theory. Both numerical and experimental data show the expected linear dependence of phase velocity changes with load and sinusoidal dependence with angle of propagation, all at a single frequency. However, systematic differences between theory and experiment indicate that additional measurements should be performed to independently measure third order elastic constants for the specific material under consideration.

The robustness of the Lamb wave results as a function of propagation angle suggest that Lamb wave measurements may provide an alternative means of measuring third order elastic constants. This would be challenging because unlike bulk wave measurements, there is no analytical expression relating third order elastic constants to measured time shifts, much less a closed form solution for the inverse problem. Thus, any means of using Lamb wave data to obtain third order elastic constants would have to be numerical in nature with the resulting issues of existence and uniqueness.

Additional experiments are also needed to verify some of the interesting theoretical predictions, particularly those shown in Figure 4.4(c) regarding isotropic phase velocities changes in the low frequency region for the A_0 mode. Future theoretical work should consider extension of this theory to materials of higher symmetry, which is believed to be straightforward but tedious. In terms of numerical work, there are certain regions in the anti-symmetric spectrum that may indicate the presence of roots (SH_0 like solutions), although they do not correspond to any mode for the unstressed case. Most likely these are false roots are caused by imperfections in the numerical method, but they need further investigation.

5. Inversion of Acoustoelastic Lamb Wave Data

This section considers the inversion of acoustoelastic Lamb wave data, primarily to estimate biaxial stresses. Previously published methods using Lamb waves to monitor stress levels consider only guided waves propagating parallel or perpendicular to the direction of an applied, uniaxial stress. However, for operation under realistic conditions, near-homogeneous stresses in plate-like structures are in general biaxial with unknown principal directions. Degtyar and Rokhlin [42] developed an analogous approach to simultaneously calculate stresses by inverting the angle dependence of phase velocities as measured with bulk waves.

Also considered in this section is the capability of simultaneously estimating temperature changes and applied loads. Two specific cases are considered: (1) discriminating a 2D isotropic stress change from a temperature change, and (2) simultaneously estimating a temperature change and a uniaxial load.

5.1 Theory

The primary effect of an applied load on guided wave propagation is a time shift Δt of a received guided wave signal, which is caused by both changes in phase velocity and dimensions of the plate. As is well-known for bulk wave acoustoelasticity [18], analysis can take place in either a *natural* coordinate system, where all spatial variables are measured relative to the unstressed material, or an *initial* coordinate system, where variables are relative to the stressed specimen. Here the natural system is convenient to use because the transducers are permanently affixed to the plate and in the natural system, the separation distance does not change. Thus, the change in phase velocity Δc_p in this natural system can be calculated from the measured time shift Δt as per Eq. (4.29). This equation is used to extract phase velocity changes from experimentally measured time shifts Δt.

To describe guided wave propagation in an aluminum plate of thickness h with biaxial applied stresses in the plane of the plate, a coordinate system is introduced as defined in Fig. 5.1. The unknown biaxial stresses σ_{11} and σ_{22} are assumed to be applied along the x_1 and x_2 axes of the rectilinear coordinate system x_i, from which a measurement coordinate system, indicated by x_i', is rotated by an angle α. It is further assumed that ultrasonic guided waves are propagating along a direction in the x_1-x_2 plane that makes an angle θ with respect to the x_1 axis and θ' with respect to the x_1' axis.

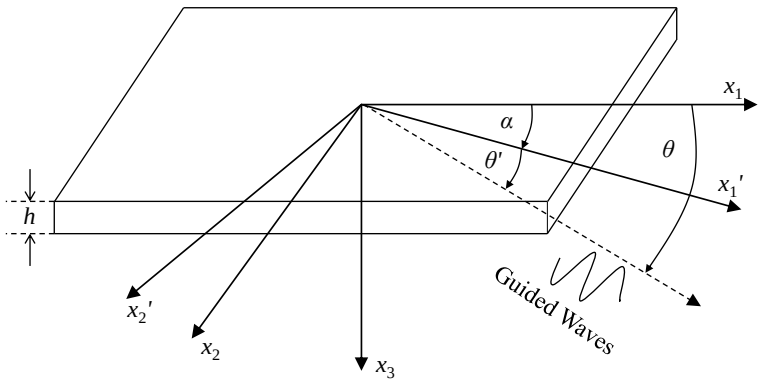

Figure 5.1. Geometry for guided wave propagation in a pre-stressed aluminum plate.

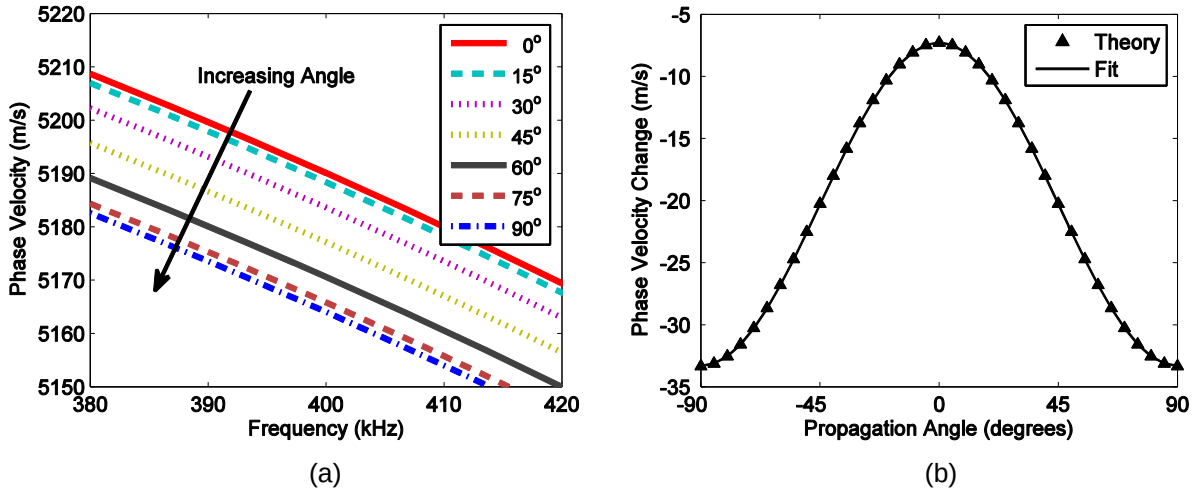

Figure 5.2. (a) Dispersion curves for the S_0 mode at different propagation angles when σ_{11} = 30 MPa and σ_{22} = 80 MPa. (b) Changes of phase velocity for the S_0 mode at 400 kHz as a function of propagation angle when σ_{11} = 30 MPa and σ_{22} = 80 MPa.

As described in Section 4, theory has been developed as part of this project to calculate dispersion curves for Lamb wave propagation in pre-stressed plates with biaxial applied loads. Using software developed by Gandhi [36], dispersion curves for different propagating angles are plotted in Fig. 5.2(a) over a narrow frequency range for the S_0 fundamental guided wave mode, which illustrates the anisotropic effect caused by an applied anisotropic load. Fig. 5.2(b) shows changes of phase velocity with respect to propagation angle for this same mode and a frequency of 400 kHz. It can be seen that there is a sinusoidal relation between angle of propagation and change in phase velocity Δc_p.

Based on this sinusoidal dependence, equations that describe the relation between phase velocity change and propagation angle for uniaxial applied stresses at 0° and 90° have the following forms:

$$\Delta c_p(\theta)\big|_{\sigma_{22}=0} = \sigma_{11}(K_1 \cos^2\theta + K_2 \sin^2\theta) \tag{5.1}$$

$$\Delta c_p(\theta)\big|_{\sigma_{11}=0} = \sigma_{22}(K_3 \cos^2\theta + K_4 \sin^2\theta) \tag{5.2}$$

In these equations, Δc_p is the change of phase velocity, θ is the direction of guided wave propagation in the principal (unprimed) coordinate system, and K_1, K_2, K_3 and K_4 are the four acoustoelastic constants for the particular frequency, mode and applied stress direction. Similar equations have been used for bulk and surface waves although the corresponding acoustoelastic constants are independent of frequency [18]. For an isotropic plate, the four acoustoelastic constants can be reduced to two (i.e., $K_1 = K_4$, $K_2 = K_3$) because of symmetry. We hypothesize that the linear combination of Eqs. (5.1) and (5.2) describes the change of phase velocity for an applied biaxial stress:

$$\Delta c_p(\theta) = (K_1\sigma_{11} + K_2\sigma_{22})\cos^2\theta + (K_2\sigma_{11} + K_1\sigma_{22})\sin^2\theta. \tag{5.3}$$

This equation is written in the unprimed coordinate system where the principal axes of the applied stress are aligned with the coordinate axes. However, measurements are made in the primed coordinate system, which is rotated by an angle α from the principal axis system. In this system, changes in phase velocity are,

$$\begin{aligned}\Delta c_p(\theta') &= (K_1\sigma_{11} + K_2\sigma_{22})\cos^2(\theta' + \alpha) + (K_2\sigma_{11} + K_1\sigma_{22})\sin^2(\theta' + \alpha) \\ &= a_0 + a_1\cos(2\theta') + a_2\sin(2\theta').\end{aligned} \tag{5.4}$$

The coefficients a_i are,

$$a_0 = \tfrac{1}{2}(K_1 + K_2)(\sigma_{11} + \sigma_{22}), \tag{5.5}$$

$$a_1 = \tfrac{1}{2}(K_1 - K_2)(\sigma_{11} - \sigma_{22})\cos(2\alpha), \tag{5.6}$$

$$a_2 = -\tfrac{1}{2}(K_1 - K_2)(\sigma_{11} - \sigma_{22})\sin(2\alpha). \tag{5.7}$$

These equations suggest a strategy to estimate the principal values and direction of the applied stresses. First, acoustoelastic constants K_1 and K_2 are estimated by least-squares from known uniaxial applied loads via Eq. (5.1) or (5.2) using measurements of phase velocity changes at multiple angles of propagation. Second, for similar measurements made at an unknown load, the coefficients a_0, a_1 and a_2 can be determined by least-squares using Eq. (5.4). Finally, the applied stresses σ_{11} and σ_{22} and the angle α are solved by inverting Eqs. (5.5), (5.6) and (5.7) for the unknown quantities:

$$\alpha = \frac{1}{2}\tan^{-1}\left(-\frac{a_2}{a_1}\right), \tag{5.8}$$

$$\sigma_{11} = \frac{a_0\cos(2\alpha)(K_1 - K_2) + a_1(K_1 + K_2)}{\cos(2\alpha)(K_1^2 - K_2^2)}, \tag{5.9}$$

$$\sigma_{22} = \frac{a_0\cos(2\alpha)(K_1 - K_2) - a_1(K_1 + K_2)}{\cos(2\alpha)(K_1^2 - K_2^2)}, \tag{5.10}$$

If a temperature change occurs simultaneously with a change in load, Eq. (5.4) includes an additional term to describe the change in phase velocity caused by temperature:

$$\Delta c_p(\theta') = (K_1\sigma_{11} + K_2\sigma_{22})\cos^2(\theta' + \alpha) + (K_2\sigma_{11} + K_1\sigma_{22})\sin^2(\theta' + \alpha) + \alpha_T\Delta T. \tag{5.11}$$

In this equation ΔT is the change in temperature and α_T is a constant for a specific mode and frequency. For the case of a 2D isotropic load, the two stress components are equal and the change in phase velocity becomes isotropic,

$$\Delta c_p(\theta') = (K_1 + K_2)\sigma + \alpha_T \Delta T. \tag{5.12}$$

Thus, for a given guided wave mode and frequency, it is not possible to simultaneously determine the temperature change and the isotropic load.

For the case of a uniaxial load applied along the x_2 direction, the change in phase velocity is,

$$\begin{aligned}\Delta c_p(\theta') &= \sigma_{22}\left[K_2 \cos^2(\theta' + \alpha) + K_1 \sin^2(\theta' + \alpha)\right] + \alpha_T \Delta T \\ &= a_0 + a_1 \cos(2\theta') + a_2 \sin(2\theta').\end{aligned} \tag{5.13}$$

The constants a_i are,

$$a_0 = \tfrac{1}{2}(K_1 + K_2)\sigma_{22} + \alpha_T \Delta T, \tag{5.14}$$

$$a_1 = -\tfrac{1}{2}(K_1 - K_2)\sigma_{22} \cos(2\alpha), \tag{5.15}$$

$$a_2 = \tfrac{1}{2}(K_1 - K_2)\sigma_{22} \sin(2\alpha). \tag{5.16}$$

The change in phase velocity caused by the load is clearly anisotropic, with an additional isotropic contribution caused by the temperature change. Inversion of these equations yields,

$$\alpha = \frac{1}{2}\tan^{-1}\left(-\frac{a_2}{a_1}\right), \tag{5.17}$$

$$\Delta T = \frac{a_0 \cos(2\alpha)(K_1 - K_2) + a_1(K_1 + K_2)}{\alpha_T \cos(2\alpha)(K_1 - K_2)}, \tag{5.18}$$

$$\sigma_{22} = \frac{-2a_1}{\cos(2\alpha)(K_1 - K_2)}, \tag{5.19}$$

Thus, if there is *a priori* knowledge that the load is uniaxial, then the load and temperature change can be simultaneously determined.

5.2 Numerical Verification

The proposed strategy for estimating biaxial loads depends upon the hypothesis that changes in phase velocity due to a biaxial load are a linear combination of the two contributions for the uniaxial principal components. To verify this hypothesis, numerical simulations are performed to assess its validity. The changes of phase velocity at 400 kHz for the S_0 mode of guided waves in a homogeneous and isotropic aluminum plate of thickness 3.175 mm were chosen to be consistent with the later experimental verification. The material properties of the plate for numerical simulation are described in Table 5.1. Note that the software calculates all phase velocity changes in the natural (unstressed) coordinate system.

Table 5.1. Density and elastic constants of aluminum used for simulations.

Property	Value and Units
λ	50.281 GPa
μ	25.902 GPa
l	-252.2 GPa
m	-324.9 GPa
n	-351.2 GPa
ρ	2700 kg/m^3

First, phase velocity changes Δc_p were calculated for multiple uniaxial stress conditions as $\sigma_{11} = 0$ and σ_{22} increasing from 0 to 100 MPa in steps of 10 MPa; the propagation angle θ varied from 0 to 90 degrees in steps of 5 degrees. Second, acoustoelastic constants K_1 and K_2 were estimated by least-squares using Eq. (5.2) using the multiple known uniaxial stresses and corresponding phase velocity changes Δc_p obtained from the first step; their values were consistent for all loads considered. Third, theoretical phase velocity changes were calculated as a function of propagation angle for multiple cases of α, σ_{11} and σ_{22}. Finally, K_1 and K_2 determined from the second step were used in Eq. (5.4) to approximate the changes of phase velocity for the multiple cases of α, σ_{11} and σ_{22}.

The approximate results calculated as per Eq. (5.4) were found to be in excellent agreement with the theoretical phase velocity changes Δc_p for all cases considered. Typical results are shown in Fig. 5.3 for two cases: (1) $\alpha = 30°$, $\sigma_{11} = 50$ MPa, $\sigma_{22} = 100$ MPa, and (2) $\alpha = 90°$, $\sigma_{11} = 10$ MPa, $\sigma_{22} = 40$ MPa. The root mean square errors for these two cases are 0.0663m/s and 0.0112m/s, respectively, and are typical for all cases considered. Therefore, the assumed sinusoidal dependence and linear combination of uniaxial loads as expressed in Eqs. (5.3) and (5.4) are taken to be correct.

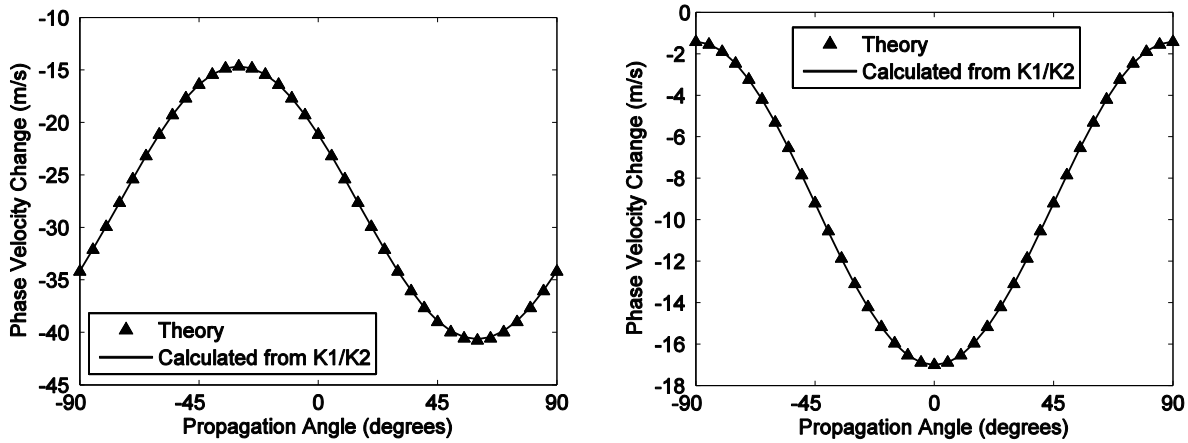

Figure 5.3. Phase velocity changes for the S_0 mode at 400 kHz versus propagation angle. (a) $\sigma_{11} = 50$ MPa, $\sigma_{22} = 100$ MPa, and $\alpha = 30$ degrees. (b) $\sigma_{11} = 10$ MPa, $\sigma_{22} = 40$ MPa, and $\alpha = 90$ degrees.

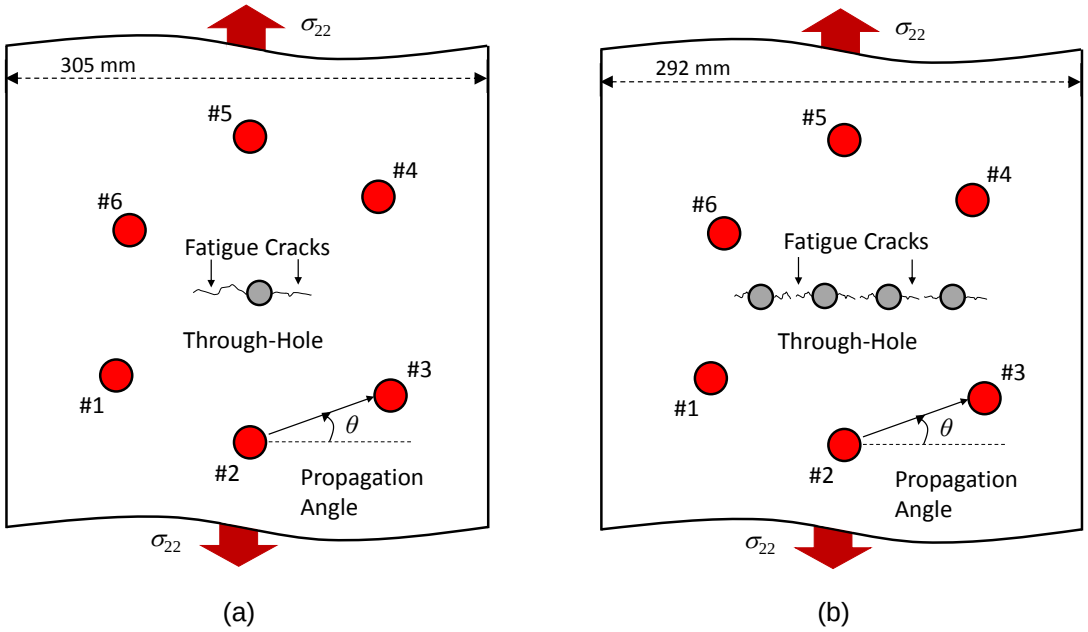

Figure 5.4. Drawing of the specimen and transducer geometry for (a) Plate #5 and (b) Plate #6 (not to scale).

5.3 Experiments and Results for Biaxial Load Estimation

Results are shown here using fatigue test data from Plate #5 and Plate #6 as described in Sections 3.5 and 3.6, respectively. Each transducer pair corresponds to guided wave propagation along a particular direction, which corresponds to the line connecting the transducers; see Figure 5.4 for sketches of the plates and transducers. Measured signals were filtered by a 7 cycle, Hanning windowed, 400 kHz tone burst signal as described in [32]. The 400 kHz S_0 Lamb wave mode was chosen for analysis because it has clear first arrivals from all the transducer pairs and it is also the dominant mode at this frequency with a very good signal-to-noise ratio. The only other possible mode at 400 kHz is the slower A_0 mode, and the echoes were not sufficiently distinct to accurately extract phase velocity changes.

5.3.1 Calibration and error analysis

The calibration procedure was performed to calculate the acoustoelastic constants K_1 and K_2 using data recorded from the first data set for both fatigue tests. Figure 5.5(a) shows the received S_0 signals from transducer pair 2-5 (i.e., transmitting on #2 and receiving on #5) of data set #1 from Plate #5 at different loads. The zero crossings of these direct arrivals were extracted as a function of applied load and are plotted in Fig. 5.5(b); it can be seen that the small time shifts relative to zero load are linear with load over the entire load range. The corresponding changes of phase velocity Δc_p for the 11 loading conditions and 15 transducer pairs in data set #1 were calculated by Eq. (4.29) from the calculated time shifts, nominal values of c_p obtained at zero-load from dispersion curves, and measured transducer separation distances. The data of Δc_p calculated from all the transducer pairs were then used in Eq. (5.2) to estimate constants K_1 and K_2 from all known uniaxial loads via the best sinusoidal fit.

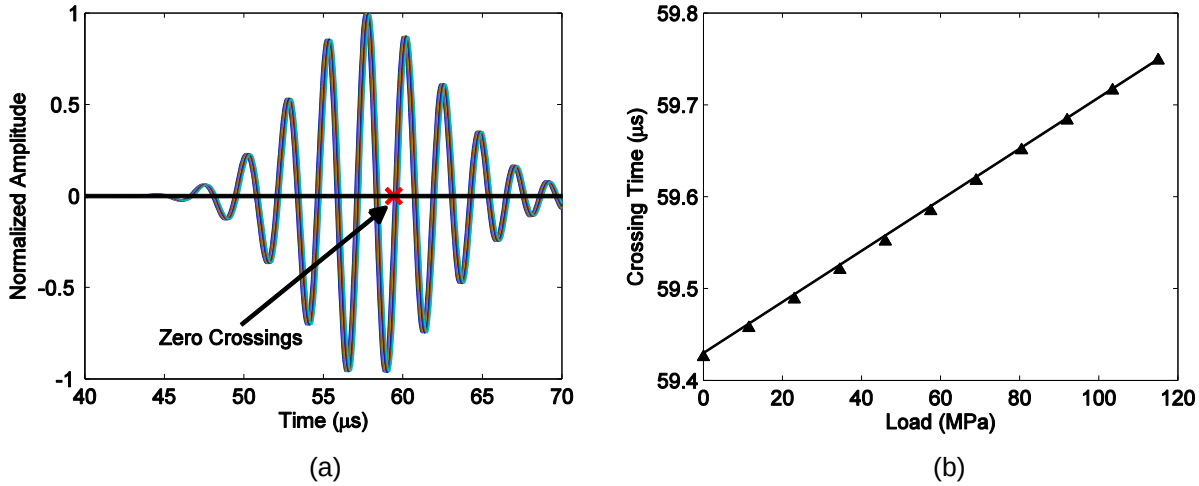

Figure 5.5. (a) First arrivals of transducer pair #2−5, data set #1 (no holes, no cracks), Plate #5, for the 11 uniaxial loading conditions. (b) Zero crossing times with respect to loads for transducer pair #2−5, data set #1 (line connects first and last points).

Figure 5.6 shows the sinusoidal fit for phase velocity changes Δc_p with respect to the angle of propagation for the load of 92 MPa. To evaluate the fit, the root mean square (RMS) error between the experimental and fitted data as shown in Figure 5.6 was computed using the estimated values of K_1 and K_2 obtained from all of the uniaxial loads. The small value of 0.5037m/s indicates an excellent sinusoidal fit, and the corresponding values of K_1 and K_2 (-3.42×10^{-7} m/s/Pa and 0.69×10^{-7} m/s/Pa, respectively) are thus assumed to be accurate. The same calibration procedure was applied to data set #1 of fatigue test 2, although the specimen during calibration was not pristine (the four holes were pre-drilled). The acoustoelastic constants K_1 and K_2 were found to be -3.77×10^{-7} m/s/Pa and 0.71×10^{-7} m/s/Pa, respectively, which are very close to those values calculated from the first specimen.

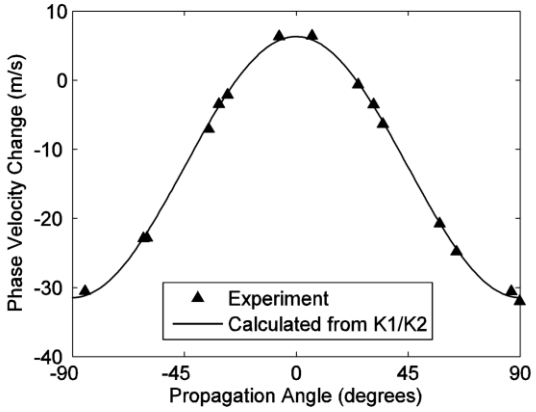

Figure 5.6. Experimental data and sinusoidal fit of phase velocity changes versus angle for data set 1 of Plate #5.

Once K_1 and K_2 are obtained, applied stresses and directions can be estimated from the phase velocity changes Δc_p obtained from later data sets using Eqs. (5.4), (5.8), (5.9) and (5.10). However, as the cracks grow in the plate and open under load, the received ultrasonic signals are affected by the guided waves interacting with and scattering from the cracks. As shown in Figure 5.7 for transducer pair 2-5 of data set #9 from Plate #5, the relationship between time shift and applied load is no longer linear over the full range of applied loads. As the time shift data become skewed by the opening cracks, there are resulting errors in the phase velocity changes Δc_p. These errors affect the sinusoidal fit of Eq. (5.4) and subsequent determination of both the a_i and the recovered stress information.

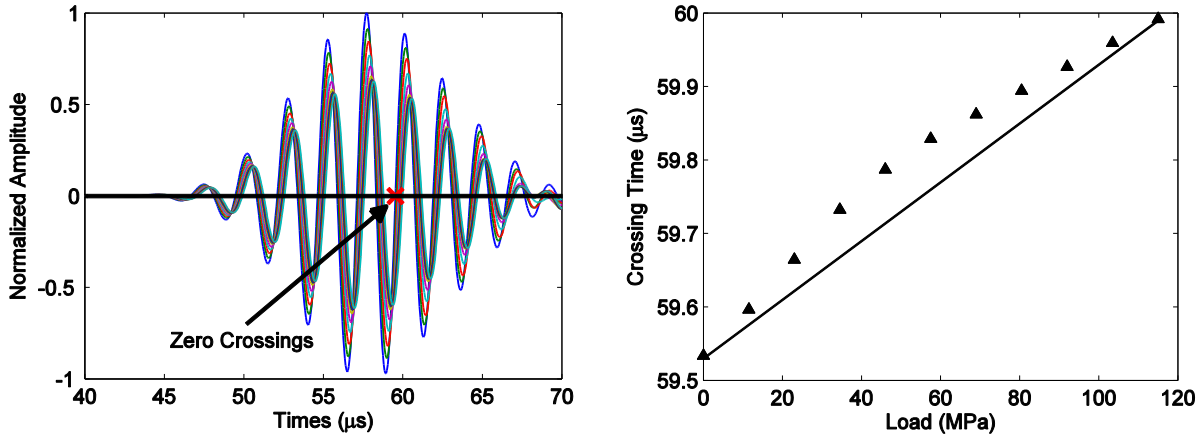

Figure 5.7. (a) First arrivals of transducer pair #2−5, data set #9, Plate #5, for the 11 uniaxial loading conditions. (b) Zero crossing times with respect to loads for transducer pair #2−5, data set #9 (line connects first and last points).

To calculate error bars for estimated stress results, consider the following least squares minimization for determining a_0, a_1 and a_2 based upon Eq. (5.4):

$$E = \sum_{i=1}^{N} \left\{ \Delta c_p(\theta_i') - \left[a_0 + a_1 \cos(2\theta_i') + a_2 \sin(2\theta_i') \right] \right\}^2, \tag{5.20}$$

where N is the number of data points. The resulting values of a_0, a_1 and a_2 can be expressed as a linear combination of the $\Delta c_p(\theta'_i)$, the change of phase velocity measured by the i*th* transducer pair:

$$\begin{bmatrix} a_0 \\ a_1 \\ a_2 \end{bmatrix} = \mathbf{C}^{-1} \begin{bmatrix} 1 & 1 & & 1 \\ \cos(2\theta_1') & \cos(2\theta_2') & \cdots & \cos(2\theta_N') \\ \sin(2\theta_1') & \sin(2\theta_2') & & \sin(2\theta_N') \end{bmatrix} \begin{bmatrix} \Delta c_p(\theta_1') \\ \Delta c_p(\theta_2') \\ \vdots \\ \Delta c_p(\theta_N') \end{bmatrix}, \tag{5.21}$$

where the **C** matrix is defined as [22],

$$\mathbf{C} = \begin{bmatrix} N & \sum_{i=1}^{N} \cos(2\theta_i') & \sum_{i=1}^{N} \sin(2\theta_i') \\ \sum_{i=1}^{N} \cos(2\theta_i') & \sum_{i=1}^{N} \cos^2(2\theta_i') & \sum_{i=1}^{N} \cos(2\theta_i') \sin(2\theta_i') \\ \sum_{i=1}^{N} \sin(2\theta_i') & \sum_{i=1}^{N} \cos(2\theta_i') \sin(2\theta_i') & \sum_{i=1}^{N} \sin^2(2\theta_i') \end{bmatrix}. \tag{5.22}$$

The variance associated with each a_j can then be calculated by:

$$\sigma^2(a_j) = \sum_{i=1}^{N} \sigma_i^2 \left(\frac{\partial a_j}{\partial \Delta c_p(\theta_i')} \right)^2 . \tag{5.23}$$

Here σ_i is the standard deviation of $\Delta c_p(\theta'_i)$, the change in phase velocity measured from the i*th* transducer pair. These standard deviations are all assumed to be equal, and are set to the sample standard deviation of the errors of $\Delta c_p(\theta'_i)$ from the sinusoidal fit performed for each unknown load. Thus, when there are no cracks and the fit is very good, the standard deviation is low, and as cracks grow and affect the guided wave signals, the fit becomes worse and the standard deviation increases.

Finally, the standard deviation of estimated stresses and directions are computed from the variance of parameters a_0, a_1 and a_2 as follows,

$$\sigma^2(\sigma_{nn}) = \sum_{j=0}^{2} \sigma^2(a_j) \left(\frac{\partial \sigma_{nn}}{\partial a_j} \right)^2 \quad \text{and} \quad \sigma^2(\alpha) = \sum_{j=0}^{2} \sigma^2(a_j) \left(\frac{\partial \alpha}{\partial a_j} \right)^2 . \tag{5.24}$$

This procedure was implemented for both fatigue tests to obtain error bars on final results.

5.3.2 Plate #5 Results

The accuracy of the estimated loads is driven by the sinusoidal fit of $\Delta c_p(\theta_i)$. As was seen in Figure 5.6, this fit is typically very good when there are no cracks. In contrast, Figure 5.8 shows typical data from Plate #5 for two different loads when cracks are present. If the data points (all solid and open triangles) are compared to the sinusoidal fit (dashed lines), there are clearly significant errors for some of the data points. These errors are particularly large for transducer pairs whose path of direct propagation lies close to the site of cracking.

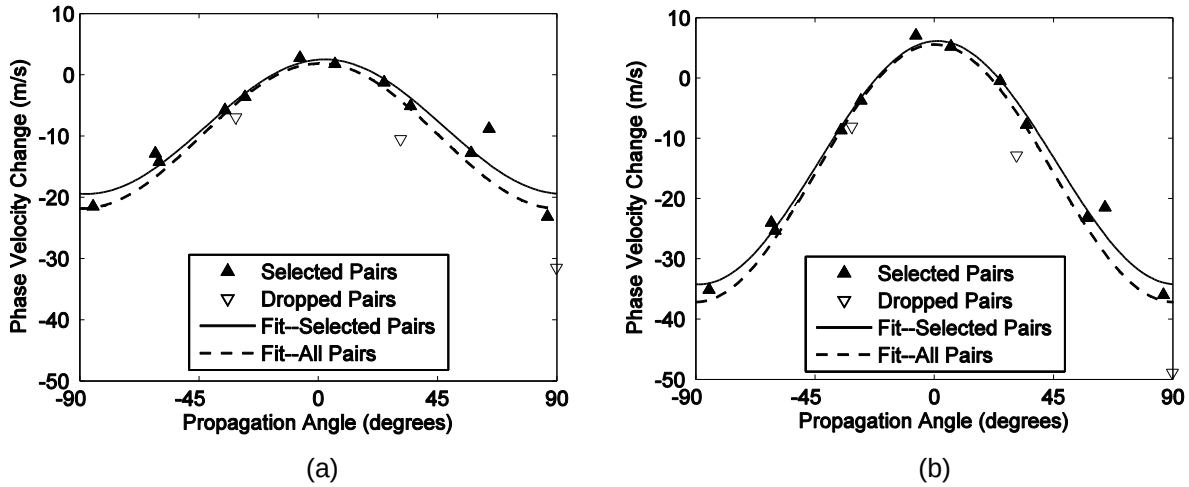

Figure 5.8. Experimental data and sinusoidal fit of phase velocity changes for data set #9 of Plate #5. (a) σ_{11} = 0 MPa, σ_{22} = 46 MPa, (b) σ_{11} = 0 MPa, σ_{22} = 92 MPa.

To minimize the effects of opening cracks on stress estimates, data from some of the transducer pairs were eliminated. As shown in Fig. 5.4(a), it can be seen that the direct arrivals for three transducer pairs travelled directly through the cracked region: 1-4, 2-5, and 3-6. Data from these three pairs were excluded from the sinusoidal fit as shown by the solid line in Figure 5.8; the three excluded data points are denoted by open triangles. The standard deviation of Δc_p was estimated from the errors relative to the sinusoidal fits, parameters a_0, a_1, and a_2 were calculated using Eq. (5.4), and σ_{11}, σ_{22} and α were calculated from Eqs. (5.8), (5.9) and (5.10). The corresponding errors were estimated for both cases (with and without eliminating data) using Eq. (5.24).

Figure 5.9 shows estimated principal stress components and direction plotted as a function of data set number. For Fig. 5.9(a), the actual values are σ_{11} = 0 MPa, σ_{22} = 46 MPa, and α = 0°; for Fig. 5.9(b) they are σ_{11} = 0 MPa, σ_{22} = 92 MPa, and α = 0°. It can be seen that elimination of the three transducer pairs reduces the impact of cracks and significantly improves the accuracy of the recovered values, particularly σ_{22}.

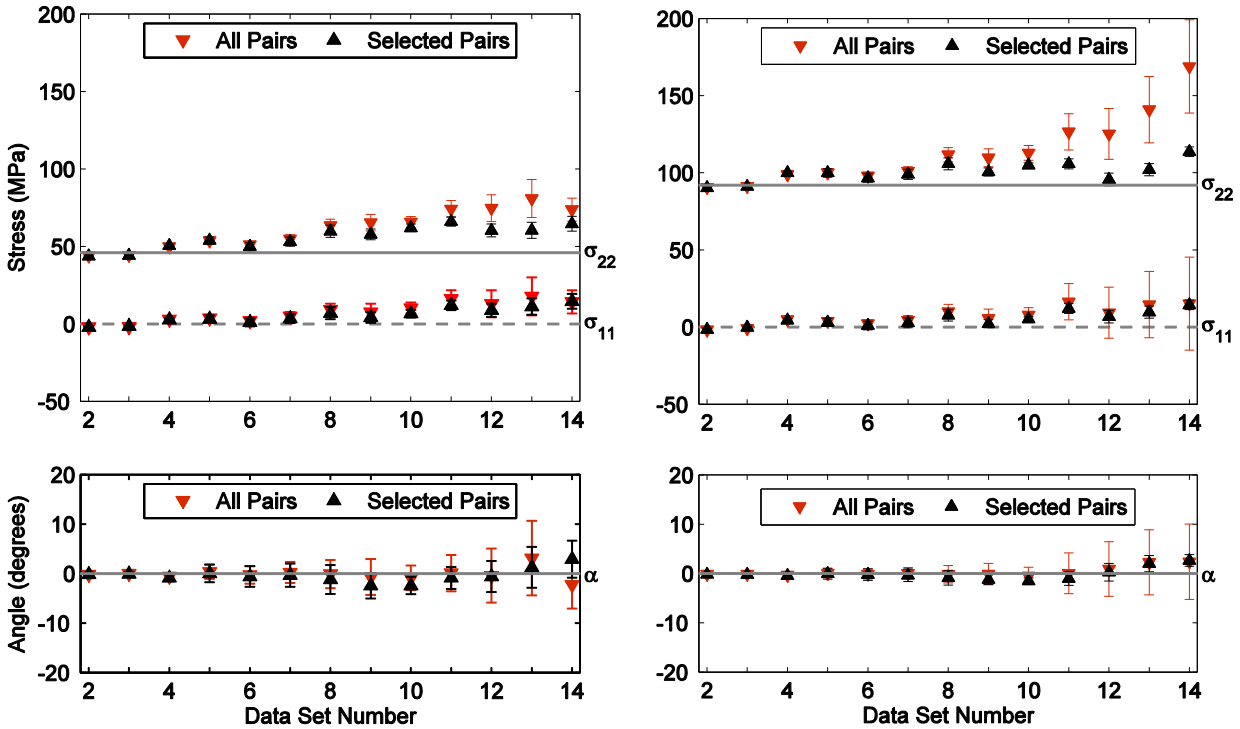

Figure 5.9. Estimated stresses and orientation angles for all data sets of Plate #5. (a) σ_{11} = 0 MPa, σ_{22} = 46 MPa, α = 0 degrees. (b) σ_{11} = 0 MPa, σ_{22} = 92 MPa, α = 0 degrees.

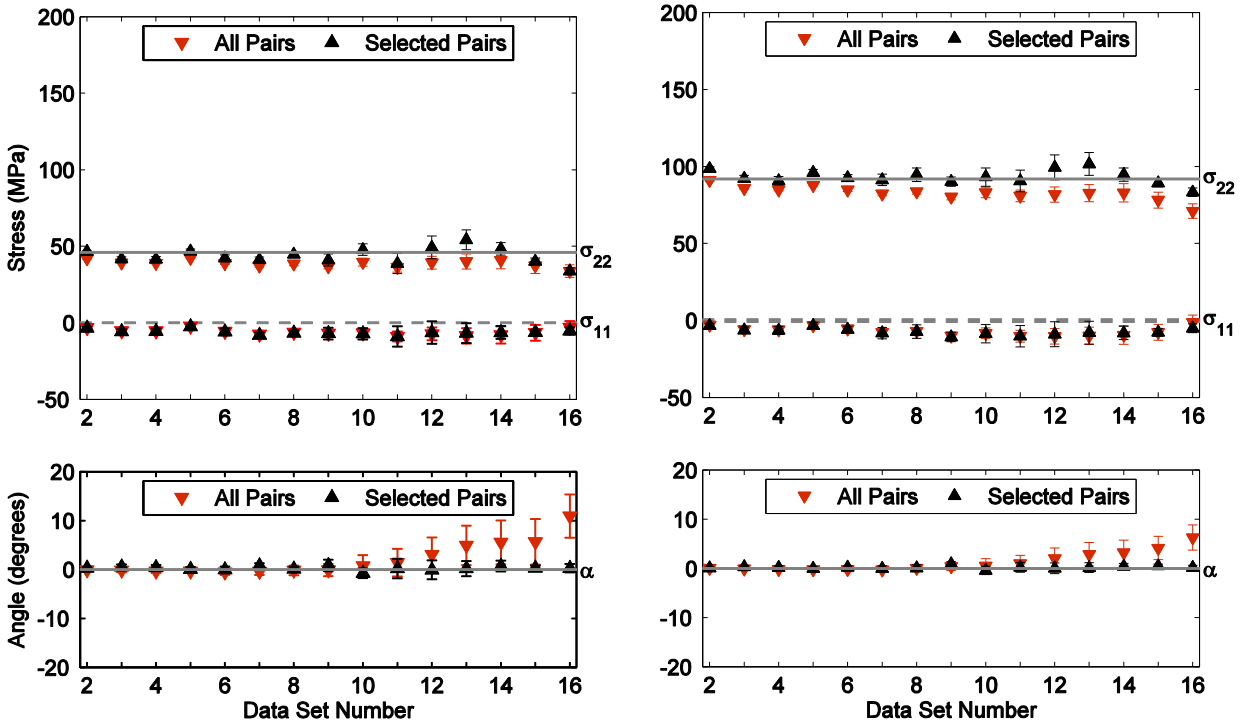

Figure 5.10. Estimated stresses and orientation angles for all data sets of Plate #6. (a) σ_{11} = 0 MPa, σ_{22} = 46 MPa, α = 0 degrees. (b) σ_{11} = 0 MPa, σ_{22} = 92 MPa, α = 0 degrees.

5.3.3 Plate #6 Results

The distribution and growth of cracks for Plate #6 is much more complicated because the four holes provide additional sites of crack initiation. A total of eight cracks initiated and grew around the region of holes during the fatigue test. However, the same idea of eliminating transducer pairs whose paths intersected with cracks was still effective. The difference is that only the six transducer pairs corresponding to waves propagating near the periphery of the transducer polygon were used; the nine transducer pairs 1-4, 2-5, 3-6, 1-6, 3-4, 1-5, 3-5, 2-4 and 2-6 were eliminated. Figure 5.10 shows estimated loads and directions compared with actual applied stresses for two different loading cases. As expected, elimination of transducer pairs gives better results, particularly for α, the applied stress direction.

5.4 Combined Estimation of Loads and Temperature

Numerical results are presented for two special cases of a temperature change occurring simultaneously with an applied load. For both cases, the temperature dependence was simulated by modeling the changes in temperature of the thickness and bulk wave speeds [43].

5.4.1 *Temperature change and 2D isotropic load*

As shown in Eq. (5.12), phase velocity changes caused by both temperature and a 2D isotropic load are isotropic (i.e., no angular dependence), and are thus not distinguishable using a single mode and frequency. Here we examine the dependence of multiple modes and frequencies on such an isotropic change to investigate whether the load-dependent behavior differs from that caused by temperature.

A typical example is taken to be a 2D isotropic load of $\sigma_{11} = \sigma_{22} = 115$ MPa and a temperature change of 35°C (25°C to 60°C). This temperature change was selected to yield the same change in phase velocity for the S_0 mode at 400 kHz as the load of 115 MPa. First, dispersion curves for the S_0, A_0, S_1 and A_1 modes were calculated for the baseline condition (no load at 25°C), under an isotropic load of 115 MPa at 25°C, and at no load and 60°C. The baseline dispersion curves were then subtracted from the other two cases, and these differential dispersion curves are shown in Figure 5.11(a). It can be seen that for the S_0 mode in the neighborhood of 500 kHz, the frequency dependence of the dispersion changes are in the opposite directions for a temperature change versus an isotropic load. Figure 5.11(b) shows a zoomed version of the S_0 curves from 0 to 600 kHz.

These curves imply that a temperature change could be distinguished from an isotropic load by monitoring the change in the S_0 phase velocity in this region. A complicating factor is that the S_0, A_0 and A_1 modes all have very similar group velocities at about 610 kHz, and thus all measurements of the S_0 mode must take place below that to avoid overlapping echoes of different modes. Also, the S_0 mode by itself will not provide enough information to characterize a combination of an isotropic load and a temperature change. It may be possible to combine S_0 measurements with changes of one or more additional modes to simultaneously decouple the two effects; additional numerical and experimental work is needed to further investigate this possibility. Regardless, changes are small and it is anticipated that measurements will be difficult.

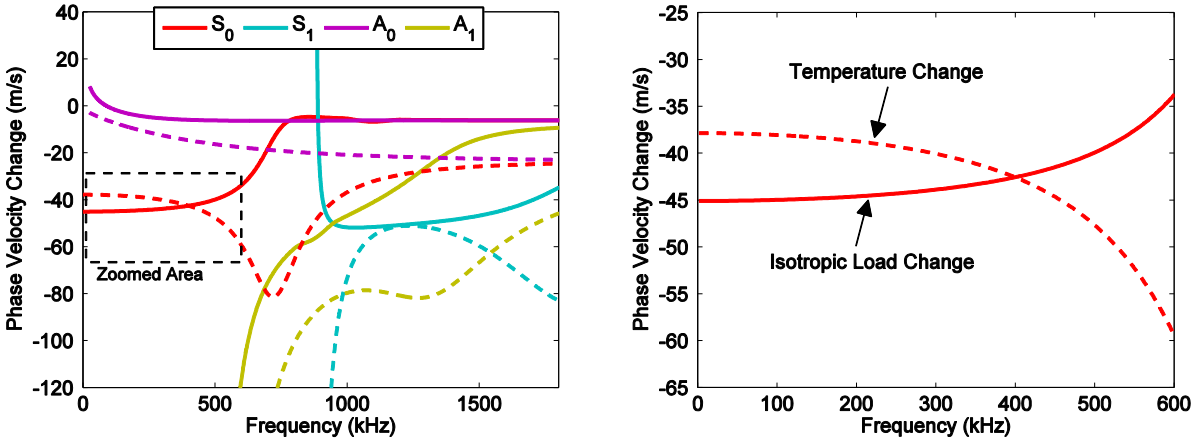

(a) (b)

Figure 5.11. (a) Phase velocity changes after subtraction of baseline dispersion curves for the first four modes. Solid lines: $\sigma_{11} = \sigma_{22} = 115$ MPa; Dashed lines: $\Delta T = 35$ °C. (b) Zoomed in phase velocity changes of the S_0 mode below 600 kHz.

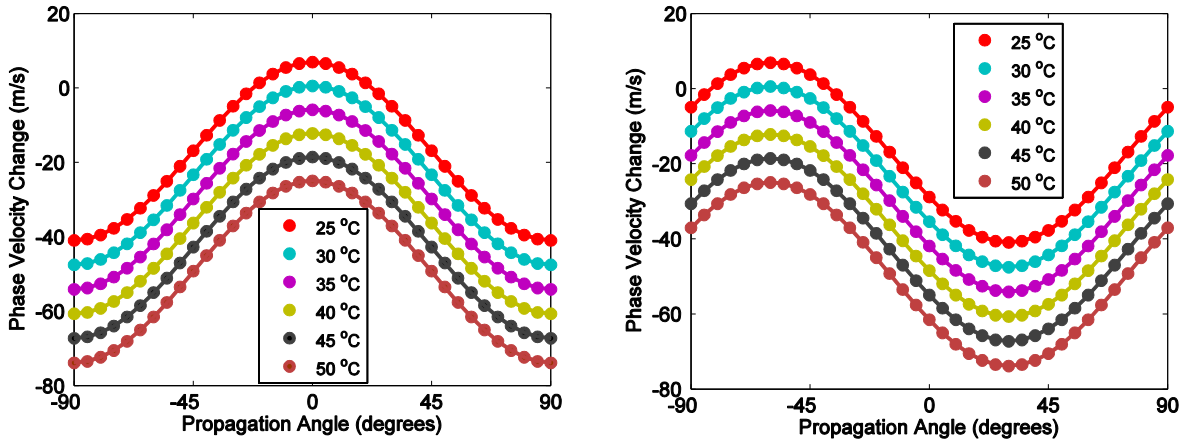

Figure 5.12. Phase velocity changes for the S_0 mode at 400 kHz under temperature variations for a uniaxial load of σ_{22} = 92 MPa. (a) α = 0°, and (b) α = 60°.

5.4.2 Combined temperature change and uniaxial load

Phase velocity changes caused by a combined temperature change and a uniaxial load are anisotropic. As indicated by Eqs. (5.17), (5.18) and (5.19), the angular dependence of the phase velocity changes from a single mode and frequency can be used to estimate both the temperature change and the load (magnitude and direction). This strategy is evaluated numerically.

Figure 5.12 shows two examples of phase velocity changes for the S_0 mode at 400 kHz caused by a combination of a temperature change and a uniaxial load. These simulations use temperature-dependent bulk wave speeds and plate thickness to calculate phase velocity changes; it is assumed that third order elastic constants are not temperature dependent. If can be seen that the primary effect of the temperature changes is to raise (or lower) the entire curve by an amount proportional to the temperature change.

The data of Figure 5.12(b) are used to evaluate the efficacy of the proposed estimation strategy. First, the constant α_T is estimated from the constant temperature data (α_T = -1.2846m/s/°C), and the constants K_1 and K_2 are estimated from the uniaxial loading data ($K_1 = -4.4433\times10^{-7}$ m/s/Pa and $K_2 = 0.7575\times10^{-7}$ m/s/Pa). These constants are then used in Eqs. (5.17), (5.18) and (5.19) to calculate the temperature, stress magnitude, and stress direction from the angular dependence of the group velocity. Results are shown in Table 5.2, and the accuracy of the recovered parameters is quite good. The largest error is about 2.2% for the estimated stress at the biggest temperature change.

5.5 Section Summary: Inversion of Lamb Wave Acoustoelastic Data

Results from both fatigue tests show that the proposed method of estimating applied biaxial stresses from a spatially distributed array of guided wave transducers can provide accurate results when cracks are not present along the paths of propagation. As cracks grow and interfere with received signals, the accuracy of the estimates decreases, which is mitigated by removing some of the data. While the accuracy may not be as good as what can be achieved using, for

example, dedicated strain gages, the method has the advantage of not requiring additional transducers.

This method is of particular interest for the case where a spatially distributed transducer array is attached on a plate-like structure since multiple transducer pairs correspond to guided waves propagating at various angles. It can be used to estimate loads in conjunction with sparse array imaging of damage by using the same transducers and recorded signals. Measuring phase velocity changes Δc_p at multiple angles in the measurement coordinate system has the advantage of estimating the unknown direction of the applied stress, which cannot be achieved from measurements along a single direction. Furthermore, only two acoustoelastic constants are needed to estimate unknown applied stresses and directions, and these two constants can be estimated from a single uniaxial loading case.

Results of a preliminary numerical investigation to simultaneously estimate load and temperature changes show some promise but also highlight the difficulty of this problem. If there is *a priori* information that the applied load is uniaxial, the numerical results indicate that a homogeneous temperature change can be estimated simultaneously with the load magnitude and direction. Results from considering a 2D isotropic load combined with a homogeneous temperature change indicate that it may be possible to separately estimate an arbitrary biaxial load and a temperature change if data from multiple modes and frequencies are considered. It is anticipated that the measurements may be prohibitively difficult.

Recommended future work includes performing experimental measurements incorporating true biaxial loads, adapting the estimation strategy to anisotropic materials, and performing controlled tests with varying loads and temperatures. It may also be possible to develop an algorithm to automatically mitigate the impact of cracks on ultrasonic signals when the locations of the cracks are unknown.

Table 5.2. Recovered temperatures and stresses for an applied uniaxial load of 92 MPa at 60°.

Actual Temperature (°C)	Estimated Temperature (°C)	Estimated Stress (MPa)	Estimated Angle (degrees)
25	25.0	92.1	60.0
30	30.0	92.5	60.0
35	35.0	92.8	60.0
40	39.9	93.3	60.0
45	44.9	93.6	60.0
50	49.9	94.0	60.0

6. Load-Differential Methods

In this section load-differential imaging methods are motivated by first evaluating the effect of loads on imaging methods using damage-free baselines, and then considering load-differential methods whereby the "baseline" is from the same damage state but a different load.

6.1 Experiments

Load-differential results are reported from Plates #5, #6, #7 and #8, which are described in Sections 3.5, 3.6, 3.7 and 3.8. Data from Plate #5 are analyzed in considerable detail, whereas only partial results are given for the other three plates. For all plates received signals were filtered to yield the equivalent narrow-band tone burst response as described in [32]. A 3-cycle Hanning windowed tone burst response centered at 100 kHz was selected because of the purity of the A_0 mode and its sensitivity to through-thickness cracks.

6.2 Analysis Methodology

The delay-and-sum imaging algorithm as applied to differenced signals is used to visualize information obtained from the transducer arrays, and is reviewed in this section (see [8] for additional details). Consider two sets of data recorded from all transducer pairs of a sparse array at different times. These two different times could correspond to before and after introduction of damage, or before and after a change in environmental or operational conditions. The 15-signal set recorded at the first time is referred to as the reference signals and the set recorded later as the current signals.

Consider sensor pair *ij* where the *i*th transducer (the transmitter) is located at (x_i,y_i), and the *j*th transducer (the receiver) is located at (x_j,y_j). If a scatterer is introduced at location (x,y), the delay time, which corresponds to the time of the wave propagating from the transmitter to the receiver by way of the scatterer, is:

$$t_{xy}^{ij} = \frac{\sqrt{(x_i - x)^2 + (y_i - y)^2} + \sqrt{(x_j - x)^2 + (y_j - y)^2}}{c_g}, \tag{6.1}$$

where c_g is the group velocity. Let $s_{ij}(t)$ refer to the differenced signal computed by subtraction of the reference signal from the current signal for sensor pair *ij*. The signal $s_{xy}(t)$ is calculated as the sum of the differenced signals delayed by the appropriate time shifts resulting from the scattering path going through the point (x,y):

$$s_{xy}(t) = \sum_i \sum_j s_{ij}(t - t_{xy}^{ij}). \tag{6.2}$$

The image value at pixel (x,y) is calculated as

$$E_{xy} = \int_{t_1}^{t_2} s_{xy}^2(t)dt, \tag{6.3}$$

where t_1 and t_2 are the start and end times of the selected time window. Although the differenced signal in Eq. (6.3) can be either the raw (RF) signal or the envelope-detected (rectified) signal,

here we only consider the envelope-detected signals. The group velocity c_g is estimated from the arrival times of the direct waves propagating between all transducer pairs as described in [8]. Values for t_1 and t_2 are calculated to yield a single sample time window centered at the nominal peak of the scattered arrival.

6.3 Imaging with Damage-Free Reference Signals

The imaging algorithm is first applied to Plate #5 using residual signals computed from damage-free reference signals. Consider images constructed from data set 2 (current signals) and data set 1 (damage-free reference signals), between which the only difference is drilling of the center through-hole. Figure 6.1 shows three images that were generated from current signals and reference signals recorded at identical loads. These and subsequent figures were created with a pixel resolution of 4 mm. At the matched loads of 0%, 50% and 100%, the three images are almost identical because the static load has minimal effects on the through-hole.

The results are much different when the same imaging algorithm is applied to the same data sets but under mismatched loads. Figure 6.2 shows three images also constructed between data sets 1 and 2, where the reference signals were recorded at zero load and the current signals were recorded at 20%, 60% and 100% loads. Although there is a 20% load mismatch for Figure 6.2(a), the image is not significantly degraded as compared to the images of Figure 6.1 and the center hole is clearly observed. However, as the load mismatch increases, the image with a 60% load mismatch is obviously degraded as Figure 6.2(b) shows with the largest amplitude features in the image being artifacts near the plate edges. The image of Figure 6.2(c) with a 100% load mismatch is degraded to a degree that the hole is no longer detectable.

Image degradation under mismatched loads is explained by considering the effects of applied loads on guided wave propagation. There are two primary effects: (1) specimen dimension changes, and (2) guided wave speed changes due to the acoustoelastic effect. Both of these changes perturb the time of arrival of individual echoes, and thus result in significant residual signals from baseline subtractions regardless of whether damage has also been introduced.

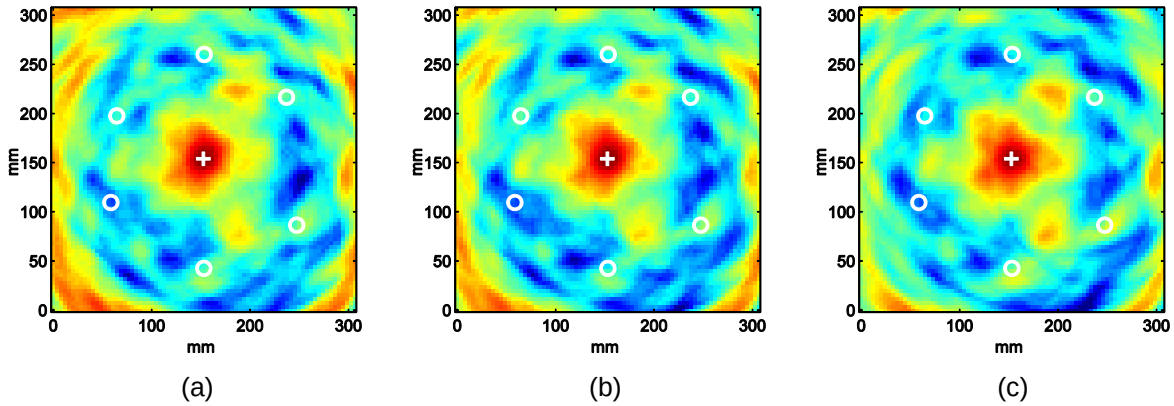

Figure 6.1. Images from Plate #5 generated between data set 1 (baseline signals) and data set 2 (current signals, after hole drilled) at matched loads. (a) 0 MPa (0% load), (b) 57.5 MPa (50% load), and (c) 115 MPa (100% load). All three images are shown on the same 10 dB color scale.

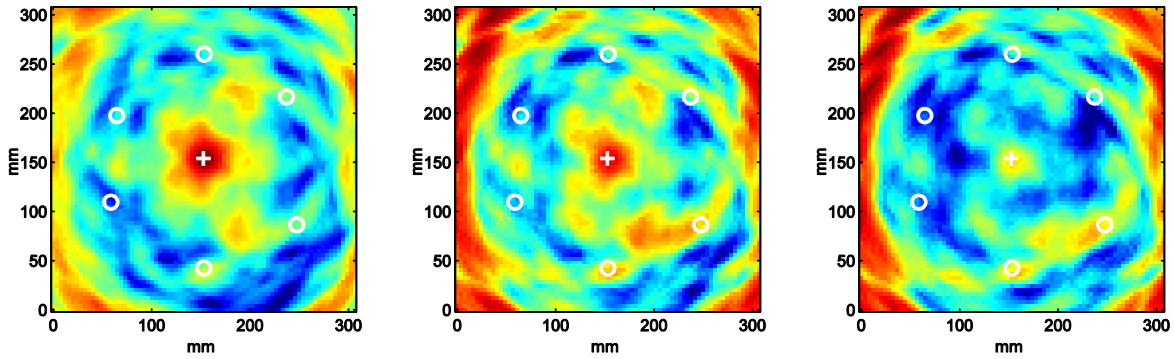

(a) (b) (c)

Figure 6.2. Images from Plate #5 generated between data set 1 (baseline signals) and data set 2 (current signals, after hole drilled) at mismatched loads. Each image is shown on a 10 dB color scale normalized to its maximum amplitude. (a) 0/23 MPa (0/20% load), (b) 0/69 MPa (0/60% load), and (c) 0/115 MPa (0/100% load).

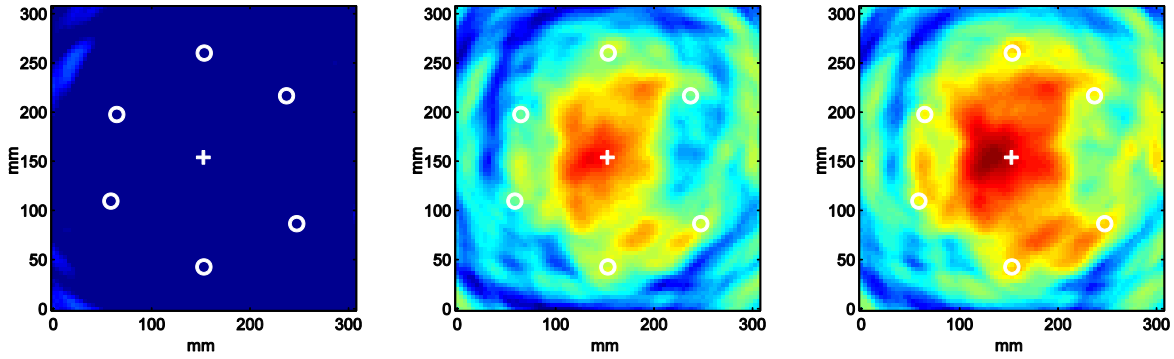

(a) (b) (c)

Figure 6.3. Images from Plate #5 generated between data set 3 (baseline signals) and data set 7 (current signals, 5.4 mm long fatigue crack) at matched loads. (a) 0 MPa (0% load), (b) 57.5 MPa (50% load), and (c) 115 MPa (100% load). All three images are shown on the same 10 dB color scale (-58 dB to -48 dB).

Now consider images obtained from data set 7 (current signals) and data set 3 (reference signals), where the primary difference between the two data sets is a 5.4 mm long single crack. Unlike Figure 6.1, which illustrates that matched applied loads have only very small effects on the through-hole, Figure 6.3 shows the much more significant effects that applied loads can have on a fatigue crack. As shown in Figure 6.3(a), the crack is not detectable at zero load because it is still tightly closed. By increasing the applied load, clear crack detection is obtained as the crack opens. Figure 6.3(b) is generated at 60% load and Figure 6.3(c) is generated at 100% load, showing that higher loads open the crack more completely and thus the images are improved.

Figure 6.4 shows images from data set 3 and data set 7 under mismatched loads where current signals were all recorded at 0% load but reference signals were recorded at 20%, 60% and 100% loads. The crack is closed at zero load and thus the guided waves propagate through it with almost no measurable effect. This situation produces images that are equivalent to those

that would be obtained if there were no damage and thus illustrate the effects of applied loads only. These images show that the mismatched loads generate stronger artifacts around the image edges; however, the maximum residual signal energy from these artifacts, as shown in Figure 6.4(c) for the greatest load mismatch, is about 3 dB less than that from the opened crack shown in Figure 6.3(c).

Figure 6.5 shows the images of data set 3 and date set 7 under mismatched loads where current signals were recorded at 100% load and reference signals were recorded at 0%, 40% and 80% loads. As shown in Figures 6.5(a) and 6.5(b), the crack is not clearly detected when the loads are significantly mismatched even though it is fully opened. The image of Figure 6.5(c), which has only a 20% load mismatch, clearly shows the crack and is not significantly degraded from Figure 6.3(c). These results, along with those shown in Figure 6.2(a) for the hole, indicate that load mismatches of up to 20% (23 MPa) can be tolerated.

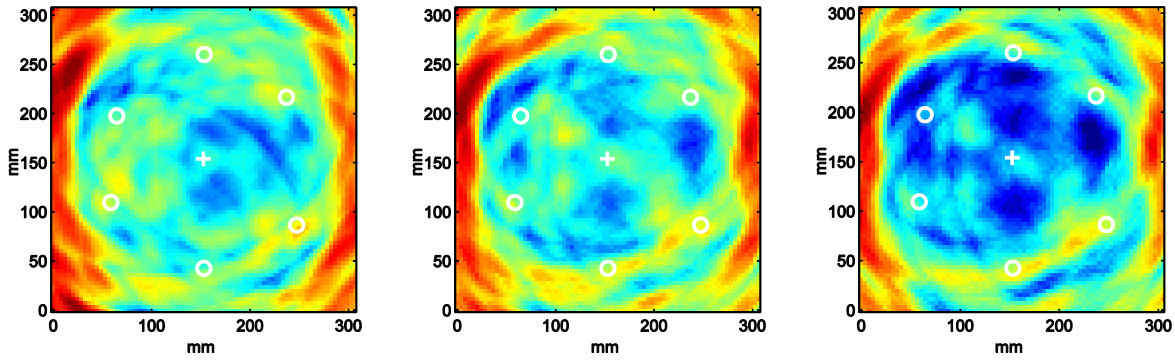

(a) (b) (c)

Figure 6.4. Images from Plate #5 generated between data set 3 (baseline signals) and data set 7 (current signals, 5.4 mm long fatigue crack) at mismatched loads. Each image is shown on a 10 dB color scale normalized to its maximum amplitude. (a) 23/0 MPa (20/0% load), (b) 69/0 MPa (60/0% load), and (c) 115/0 MPa (100/0% load).

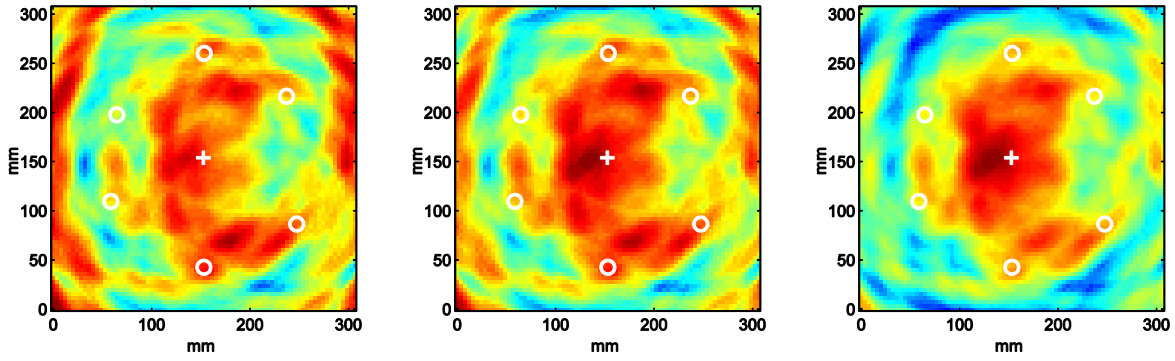

(a) (b) (c)

Figure 6.5. Images from Plate #5 generated between data set 3 (baseline signals) and data set 7 (current signals, 5.4 mm long fatigue crack) at mismatched loads. Each image is shown on a 10 dB color scale normalized to its maximum amplitude. (a) 0/115 MPa (0/100% load), (b) 46/115 MPa (40/100% load), and (c) 92/115 MPa (80/100% load).

6.4 Load-Differential Imaging

The results of the previous section motivate an alternative approach for fatigue crack detection and localization – load-differential imaging. For this method, signals recorded at one load are the "reference signals" and the signals recorded at the same damage state but at a slightly increased tensile load are the "current signals". Differences between the signals are thus caused by a combination of crack opening effects and loading effects. Figures 6.2(a) and 6.5(c) indicate that a 20% load difference (or less) will not adversely affect imaging of damage; here a 10% load difference is considered. Reference signal loads start from 0% and end at 90% with a increment of 10%, and the current signal loads range from 10% to 100% accordingly; a total of 10 differential-load pairs are thus considered for each data set.

6.4.1. Pair-wise load-differential signals

Figure 6.6 shows received signals at 11 loads from two transducer pairs of data set 10, where two cracks are present. Signals for each transducer pair are normalized by the peak amplitude of the first arrival at 0% load, when cracks are assumed to be less opened or possibly even closed. The top plot shows signals from transducer pair 2-5 (i.e., transmitting on 2 and receiving on 5), where the incident wave is broadside to the cracks and received signals are thus strongly affected by opening of the cracks with load. There is an abrupt amplitude drop between 0% load and 10% load within the time window of the first arrival of A_0 mode, which is between 80 and 110 us. The signals amplitude continues to decrease as loads increase and further open the cracks. The bottom plot shows signals from the transducer pair 1-3, where the direct path does not go through the cracked area and thus the signals are less affected by the cracks. The signal amplitude and shape change with load between 90 and 120 us, which corresponds to the path of propagation from the transmitter to the cracks to the receiver.

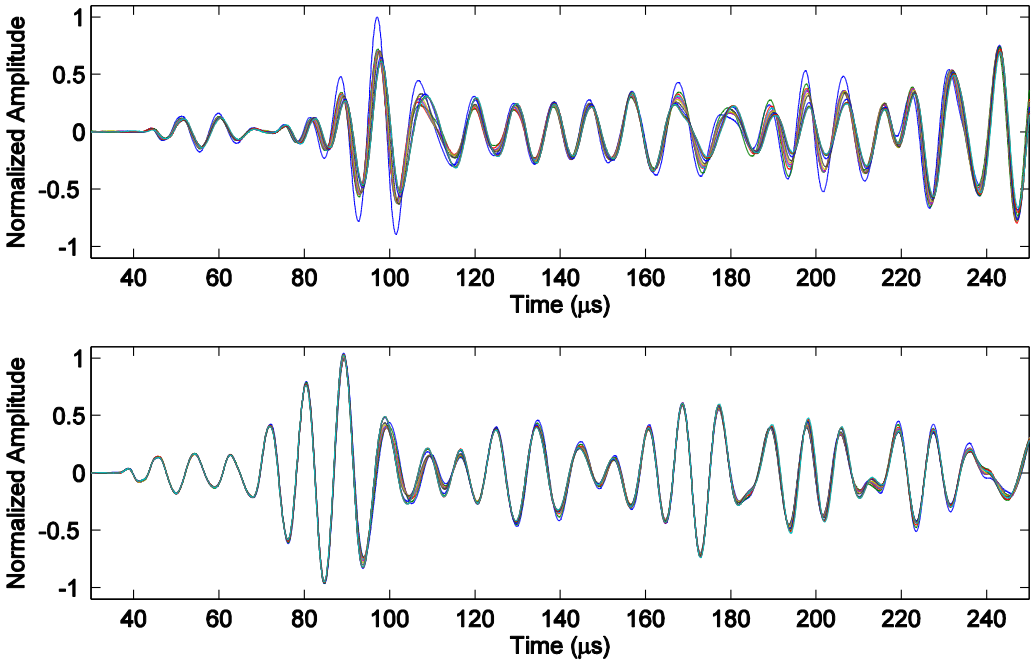

Figure 6.6. Signals recorded from data set 10 of Plate #5 at 11 loads ranging from 0 to 115 MPa (0 to 100%). Transducer pair 2-5 (top), and transducer pair 1-3 (bottom).

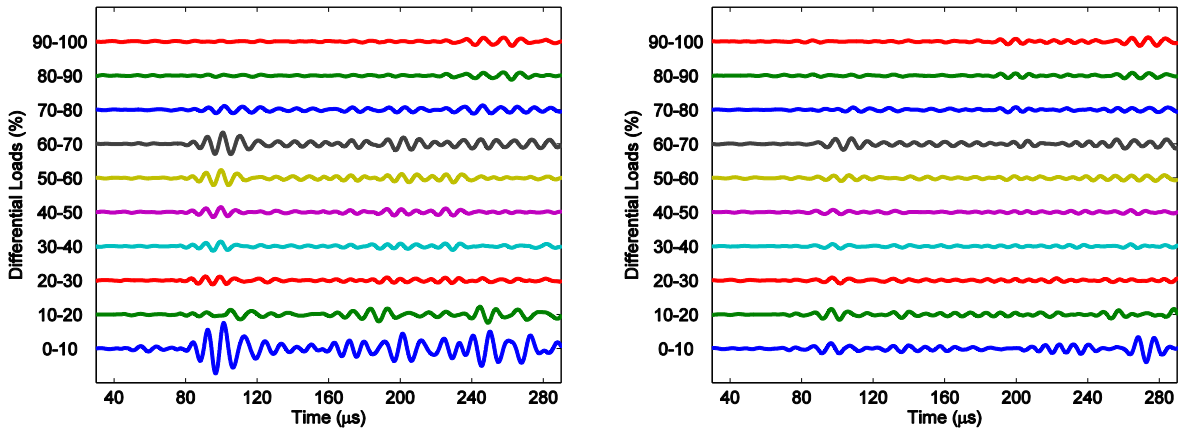

Figure 6.7. Differential signals from data set 10 of Plate #5 at ten differential loads (0-to-10%, 10-to-20%, … 90-100%). (a) Transducer pair 2-5, and (b) transducer pair 1-3.

Figure 6.7 shows waterfall plots of the ten load-differential signals for transducer pairs 2-5 and 1-3, where signals are normalized as previously described prior to subtraction. Figure 6.7(a) shows more clearly that the larger crack on one side of the hole opens up at 10% load and blocks the transmitting guided wave, resulting in the large amplitude change of the first arrival. At about 70% load the smaller crack on the other side opens up and decreases the signal amplitude further. For Figure 6.7(b), the residual signals correspond to guided waves reflected from the crack site. Similar effects can be observed as one crack opens at lower load and another crack opens at higher load.

6.4.2 Load-differential images

Load-differential signals such as shown in Figure 6.7 can be used as the differenced signals in Eq. (2) to generate ten load-differential images for each data set, which correspond to differential loads ranging from 0-10% to 90-100%. Figure 6.8 is the image collage constructed from all 14 data sets recorded from the fatigue test where all images are shown on the same 30 dB color scale. Note that the data set is the row (increasing top-to-bottom), and the differential load is the column (increasing left-to-right). The 40 images from the first four data sets are very similar because there are no cracks even though there are significant changes to the specimen (i.e., introduction of the drilled hole and starter notch). The first crack is barely seen at ~40% load from the images of data set 6, and is clearly visible by data set 7. From data set 7 to 9, images that show the crack appear at progressively lower loads, which is consistent with the crack growing as fatiguing continues and thus becoming easier to open at lower loads. For data set 10, the crack on one side of the hole starts to open at very low loads (0-10% load), whereas the crack on the other side of the hole opens up at higher loads (50-60% load); both cracks are completely opened at 90% load. Images from data sets 11 through 14 continue to show that the cracks become easier to open at low loads as both cracks keep growing. By data set 14 both cracks are very large, but there is still some evidence that they are not opening simultaneously.

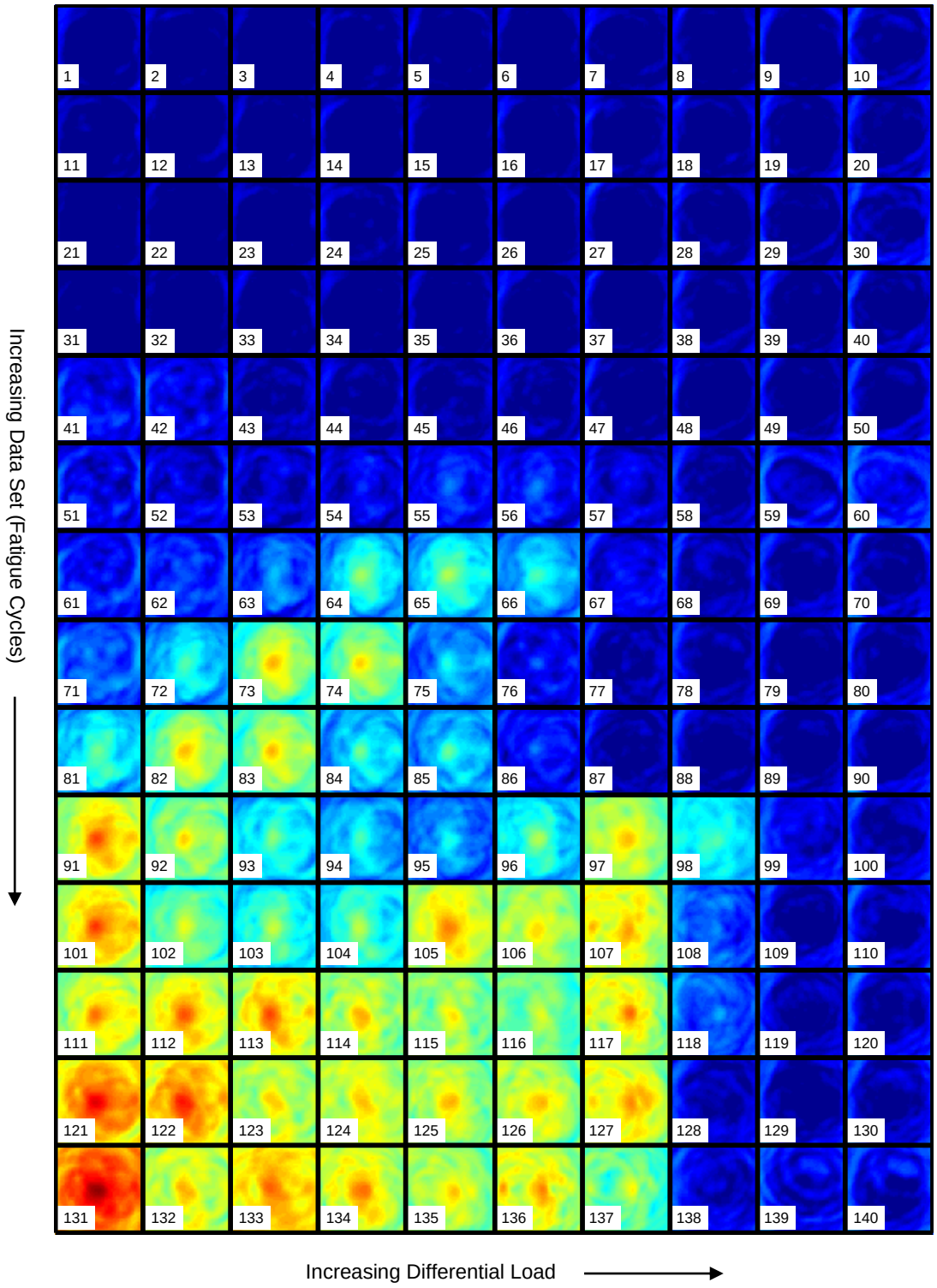

Figure 6.8. Load-differential images of the first 14 data sets from Plate #5 plotted on a fixed 30 dB scale normalized to the overall peak amplitude (-21 to +9 dB).

The load-differential images are also capable of discriminating between the two cracks on either side of the hole. Figure 6.9 shows three images from data 12 at differential loads of 20-30%, 30-40%, and 60-70%, respectively. Figure 6.9(a) clearly shows that one crack on the left side of the hole opens as the load changes from 20% to 30% load. From 30% to 40% load, as shown in Figure 6.9(b), the left side crack, which is almost fully opened, does not change very much and the crack on the right side of the hole starts to open up. Finally, as can be seen in Figure 6.9(c), from 60% to 70% load the right crack opens significantly.

6.4.3 Composite load-differential images

A composite image can readily be generated for each data set by averaging a series of load-differential images. This composite image, while perhaps not as useful for locating individual cracks as a single load-differential image, does capture in one image the cumulative effects of the applied loads. Figure 6.10 shows a collage of composite images from all data sets that were generated by averaging the ten load-differential images from each data set on a pixel-by-pixel basis. Note that the first three composite images are from data sets recorded prior to fatiguing but with differing structural conditions (i.e., no hole, hole, hole plus notch). It can be seen from these images that the fatigue crack is visible by data set 6 and is clearly evident at data set 7. Cracking is obviously increasing as fatiguing progresses.

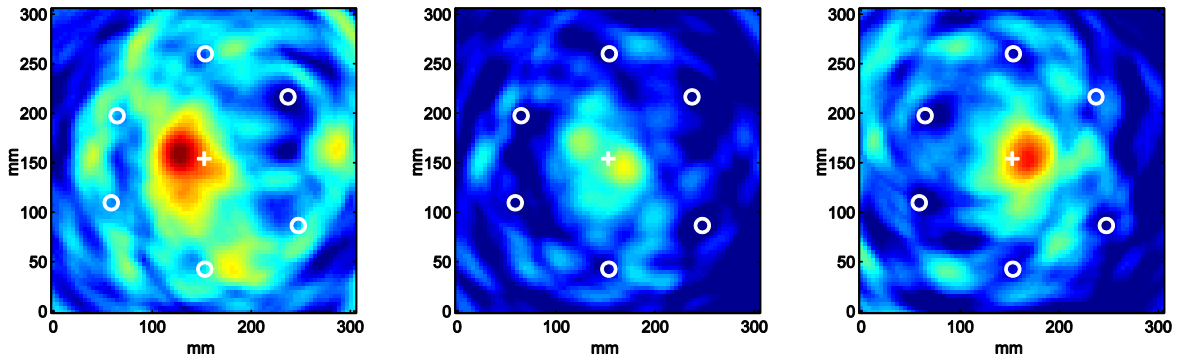

Figure 6.9. Load-differential images generated from data set 12 of Plate #5. (a) 23/34.5 MPa (20/30%), (b) 34.5/46 MPa (30/40%), and (c) 69/80.5 MPa (60/70%). All three images are shown on the same 10 dB color scale.

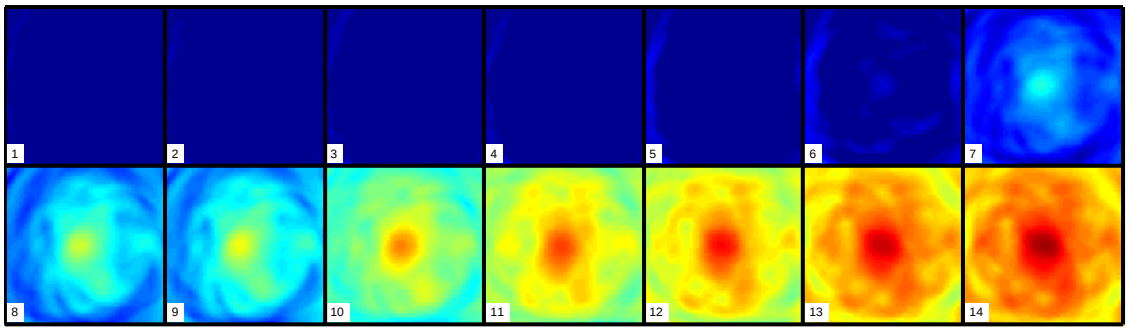

Figure 6.10. Composite load-differential images from all 14 data sets of Plate #5. All images are shown on the same 20 dB color scale (-18 dB to +2 dB).

6.5 Load-Differential Imaging of Additional Specimens

Results from additional specimens demonstrate the potential and challenges of load-differential imaging. Note that prior to computing each load-differential image, including those of Figure 6.8, all signals from both data sets were normalized by the same scale factor so that the reference data set signals had composite unity energy. This normalization was done so that images obtained from the nominally identical specimens used for this project could be compared. It was also done because there were several unexplained amplitude jumps during several of the tests, which resulted in overall level shifts of the images prior to normalization.

6.5.1 Plate #3 – Transducer Problems

The first plate that was fatigue tested as part of this project was Plate #3. Figure 6.11 contains the load-differential images for data sets 2-11, the ones recorded prior to replacing the bare PZT disc transducers. In this figure the anomalous images caused by transducer problems are obvious (i.e., apparent in data sets 4, 8, 10 and 11). Despite these problems, evidence of growing cracks can be readily seen in data sets 7-10.

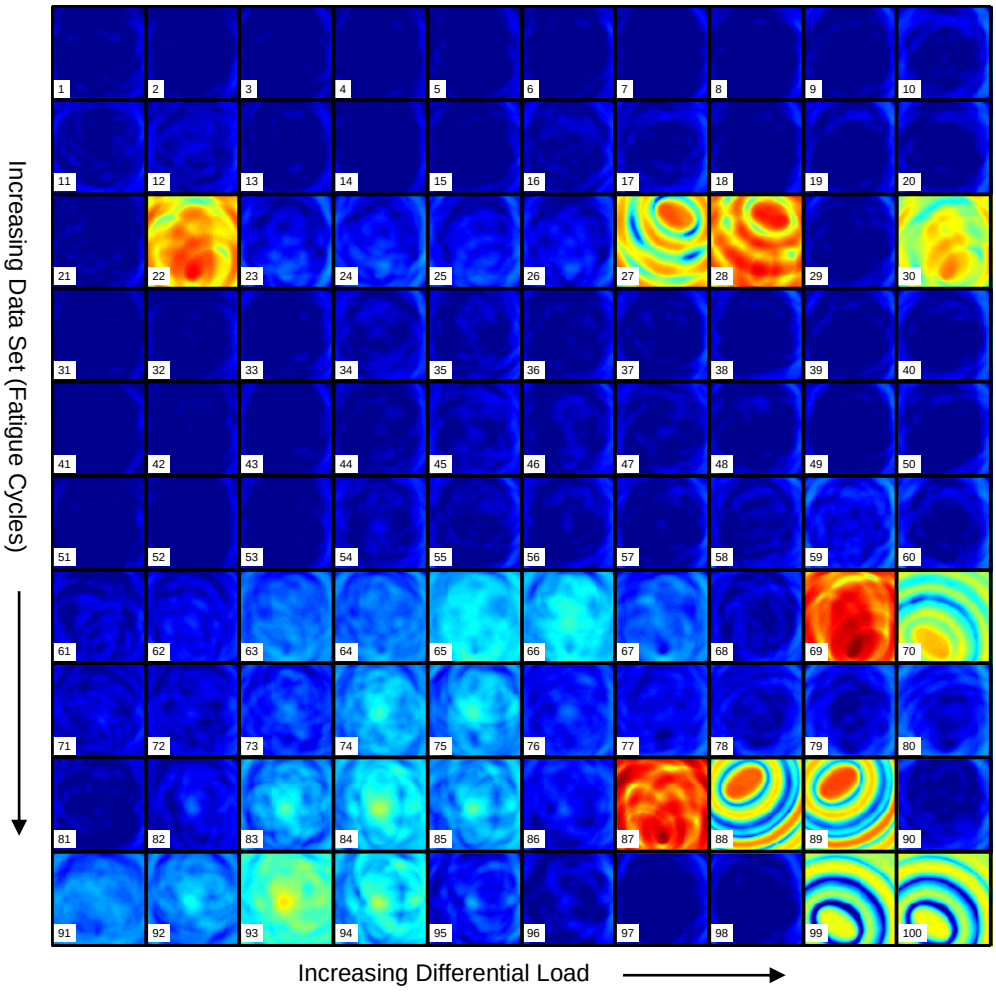

Figure 6.11. Load-differential images of the first ten data sets from Plate #3 plotted on a fixed 30 dB scale (-21 to +9 dB).

The six PZT discs were removed and replaced with identical discs that were protected with a backing compound composed of epoxy mixed with micro-bubbles. Earlier tests indicated that all backing materials evaluated had an adverse effect on signal quality, with the primary symptoms of decreased amplitude and increased ringing. The micro-bubble mixture appeared to be the best compromise. Figure 6.12 shows load-differential images from data sets 13-19 of Plate #3 on the same 30 dB scale as used for Figure 6.11. These results are rather disappointing in that the overall background noise level of the images appears to be quite high, and there is still evidence of transducer problems in two images of data set 16 (middle row). The specific elliptical pattern seen in these two images strongly suggests that data from a single transducer pair is bad; in particular, pair 5-6 located in the upper left corner.

Despite the problems seen in Figure 6.12, evidence of growing cracks is still readily apparent. A comparison of data sets 13 and 14 (first two rows) shows that the first crack is opening at lower loads, indicating that it is growing. Evidence of a smaller, second crack that is opening at higher loads can be seen in data set 15 (third row), and it is growing and thus opening at lower loads in the subsequent data sets.

The data of Figure 6.12 is re-plotted in Figure 6.13 with two changes: (1) transducer pair 5-6 was removed from all images, and (2) the data are shown on a 20 dB scale (from -11 to +9 dB) to lessen the visual effect of the higher noise background. The images of this figure compare well with those of Figure 6.8, clearly showing the initiation of the second crack and the growth of both cracks.

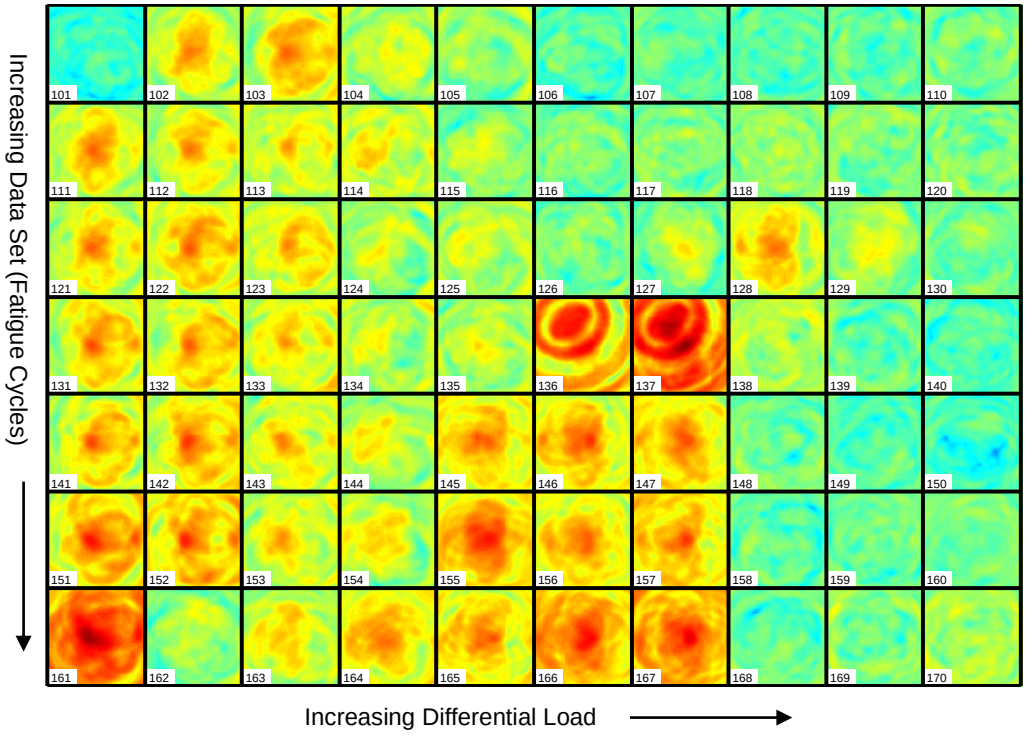

Figure 6.12. Load-differential images of the final seven data sets from Plate #3 plotted on a fixed 30 dB scale (-21 to +9 dB).

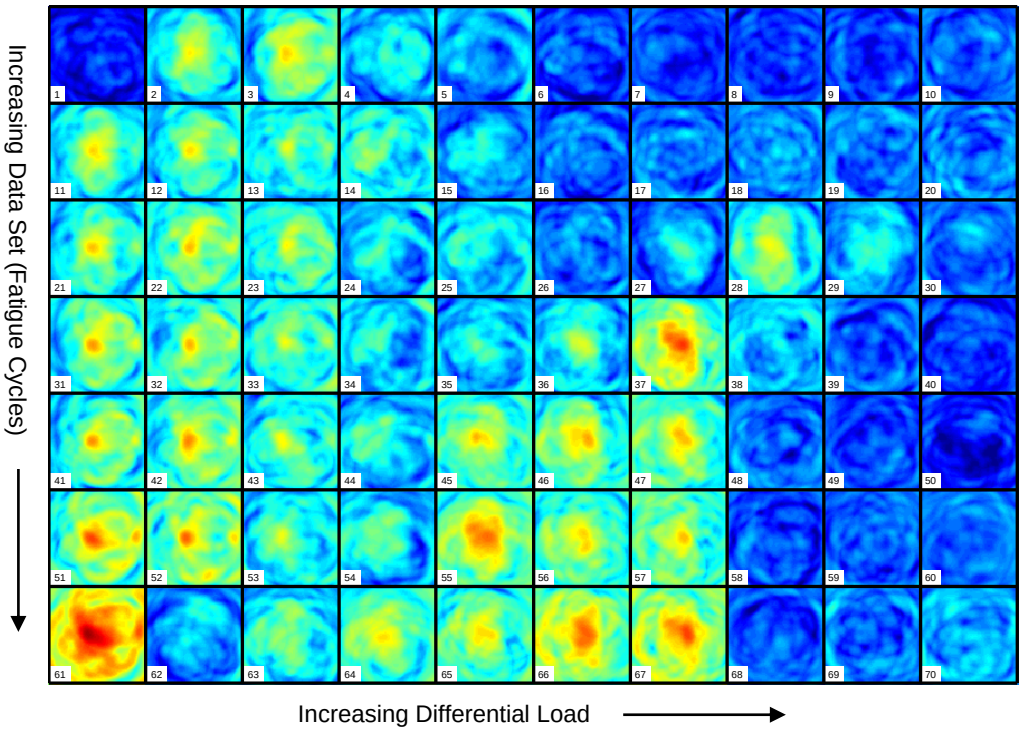

Figure 6.13. Load-differential images of the final seven data sets from Plate #3 with transducer pair 5-6 removed and plotted on a fixed 20 dB scale (-11 to +9 dB).

Composite images were obtained by averaging each data set as described in Section 6.4.3. First, the bad images from the first ten data sets were set to zero (in data sets 4, 8, 10 and 11). Also, since the transducers were changed and there was a shift in level between data sets 11 and 13, the level of the first ten composite images was adjusted by raising their amplitudes by 6 dB. This provided a reasonable transition between data sets 11 and 13. All composite images from Plate #3 are shown in Figure 6.14, and the growth of the crack is evident.

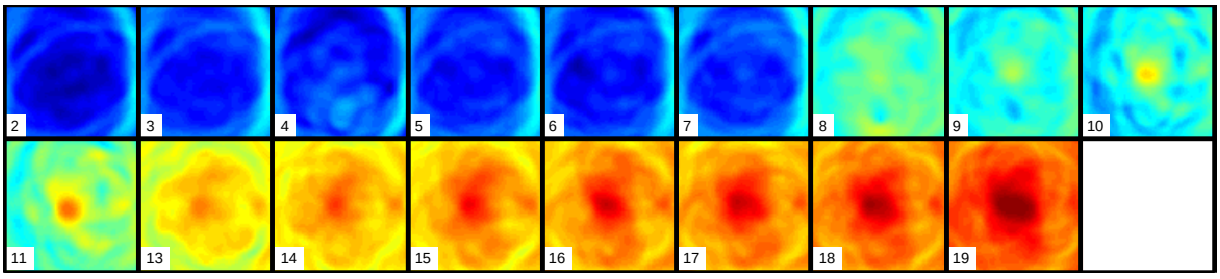

Figure 6.14. Composite load-differential images from all 17 data sets of Plate #3. All images are shown on the same 20 dB color scale (-18 dB to +2 dB).

6.5.2 Plate #4 – No cracks

Load-differential images are shown in Figure 6.15 for Plate #4. This plate had a short section of a "T"-shaped stiffener bonded to the plate, and disbonds were artificially introduced. The purpose of this specimen was initially to disbond the stiffener section under load, but after 1000 cycles it remained well-bonded. Several artificial bonds were introduced in the hope that they would change under load.

The load-differential images of Figure 6.15 do show some variations with both data set and differential loading level, but nothing that suggests opening of a marginal bond with load. This observation is not surprising since the disbonds were created artificially (as opposed to via fatigue). Some of the faint elliptical patterns are indicative of possible transducer pair problems, but are not large enough in amplitude to be of concern.

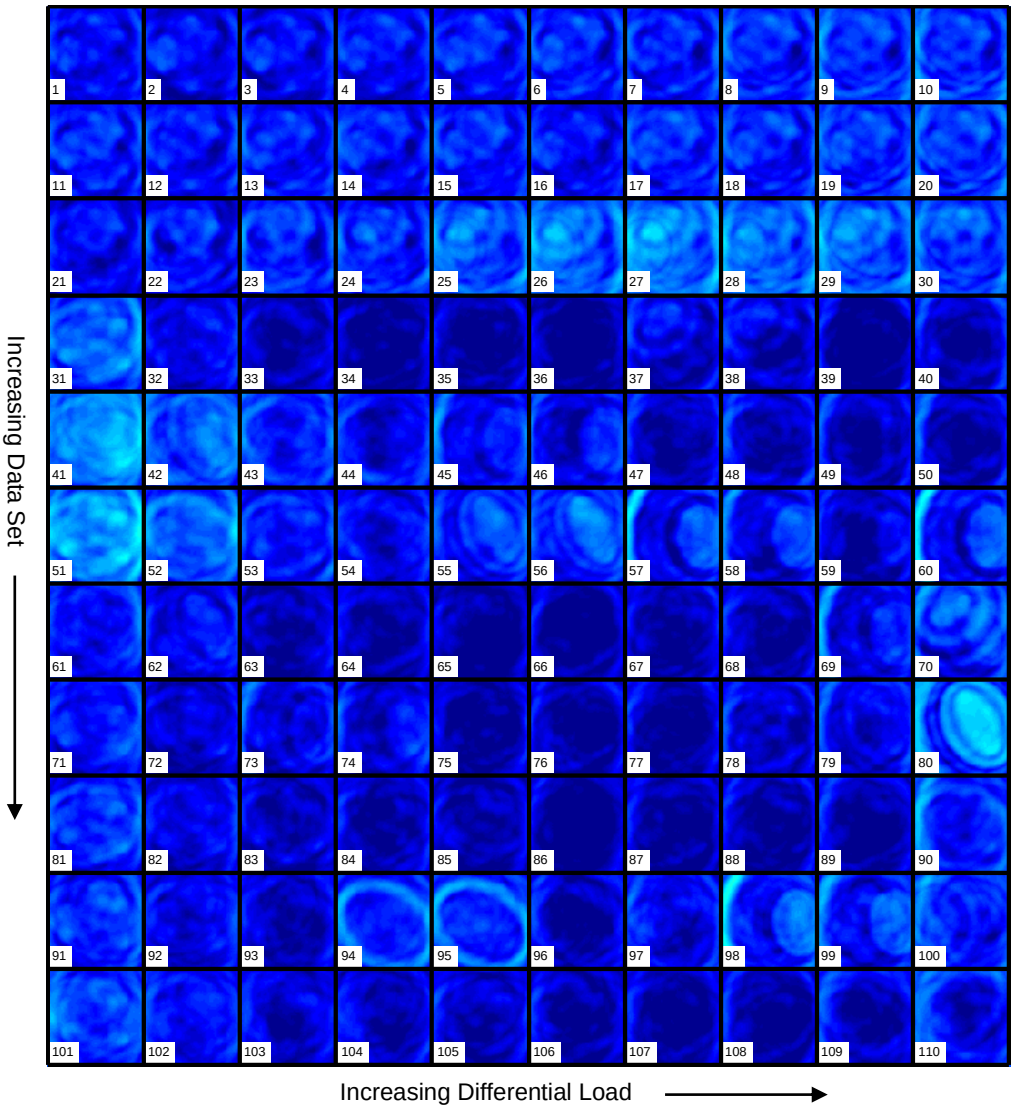

Figure 6.15. Load-differential images of all 11 data sets from Plate #4 plotted on a fixed 30 dB scale (-21 to +9 dB).

Composite images were created by averaging the individual load-differential images for each data set, and are shown in Figure 6.16. These composite images are shown on the same scale as those for Plates #3 and #5, and corroborate the conclusion that the disbond conditions are not changing significantly with load.

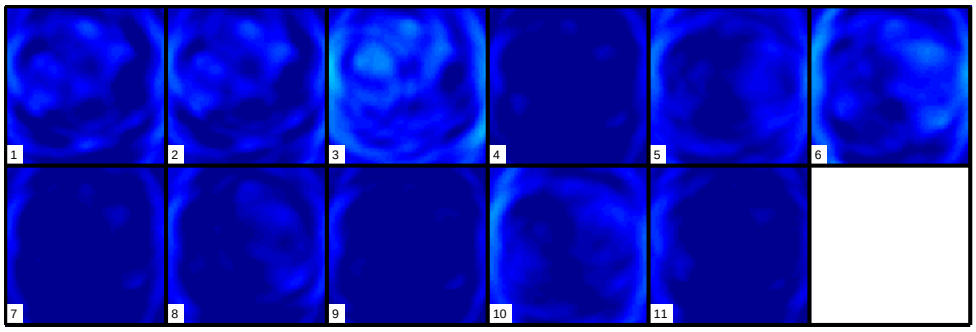

Figure 6.16. Composite load-differential images from all 11 data sets of Plate #4. All images are shown on the same 20 dB color scale (-18 dB to +2 dB).

6.5.3 Plate #5 – Added doubler and fasteners

After termination of fatiguing, a doubler was bonded to Plate #5 as described in Section 3.5 and additional 21 data sets of load-dependent data were recorded (data sets 15-35). No additional fatiguing was performed so there was no additional crack growth. However, since 21 sets of load-dependent data were recorded, the plate was subjected to significant static loads that may have introduced plastic deformation. In particular, it is likely that the cracks were held open under load enough times so that the degree of crack closure when the load was released decreased over the time of the test.

Figure 6.17 shows load-differential images for data sets 14 through 24. Recall that data set 14 corresponds to the final fatigue cycles, data sets 15-18 are of the unchanged specimen after fatiguing was terminated, data sets 19-21 are after a doubler was bonded to the plate, and data sets 22-24 are after a center hole was drilled through the doubler (aligned with the existing hole in the plate). There are no surprises in this figure. Data sets 15-18 have less of a load response for the lowest differential loading step, most likely because of the crack not closing to its previous degree after the static loads of data set 14. The images from data sets 19-24, which are after bonding of the doubler, are of lower amplitude. This is not unexpected and is caused by a combination of two effects: (1) the bonded doubler partially restrains the crack from responding to load changes, and (2) there is some scattering of the incident waves from the doubler.

Figure 6.18 shows load-differential images for data sets 25 through 35. The most dramatic changes can be seen in data sets 25-27 after insertion and tightening of a center bolt. This change almost entirely obscures the crack response because the tightened bolt keeps it from fully opening under load. After the bolt is loosened, in data sets 28-30, the crack response is again evident. The various bolt changes in data sets 31-34 cause similar effects. Data set 35, after all bolts are removed, again shows a larger amplitude crack response. The adhesion of the doubler around the crack site has probably become unbonded because of the multiple loading cycles.

These results, although not completely realistic of a built-up structure, do partially indicate the potential efficacy of load-differential imaging. In a real structure, it is probable that local disbonding and fastener loosening/movement would either precede or occur along with significant cracking; otherwise, it is unlikely that the local strains would be large enough for large cracks to form. The experiments with Plate #5 have not fully investigated this, but do show that successful load-differential imaging can take place with a bonded doubler in place.

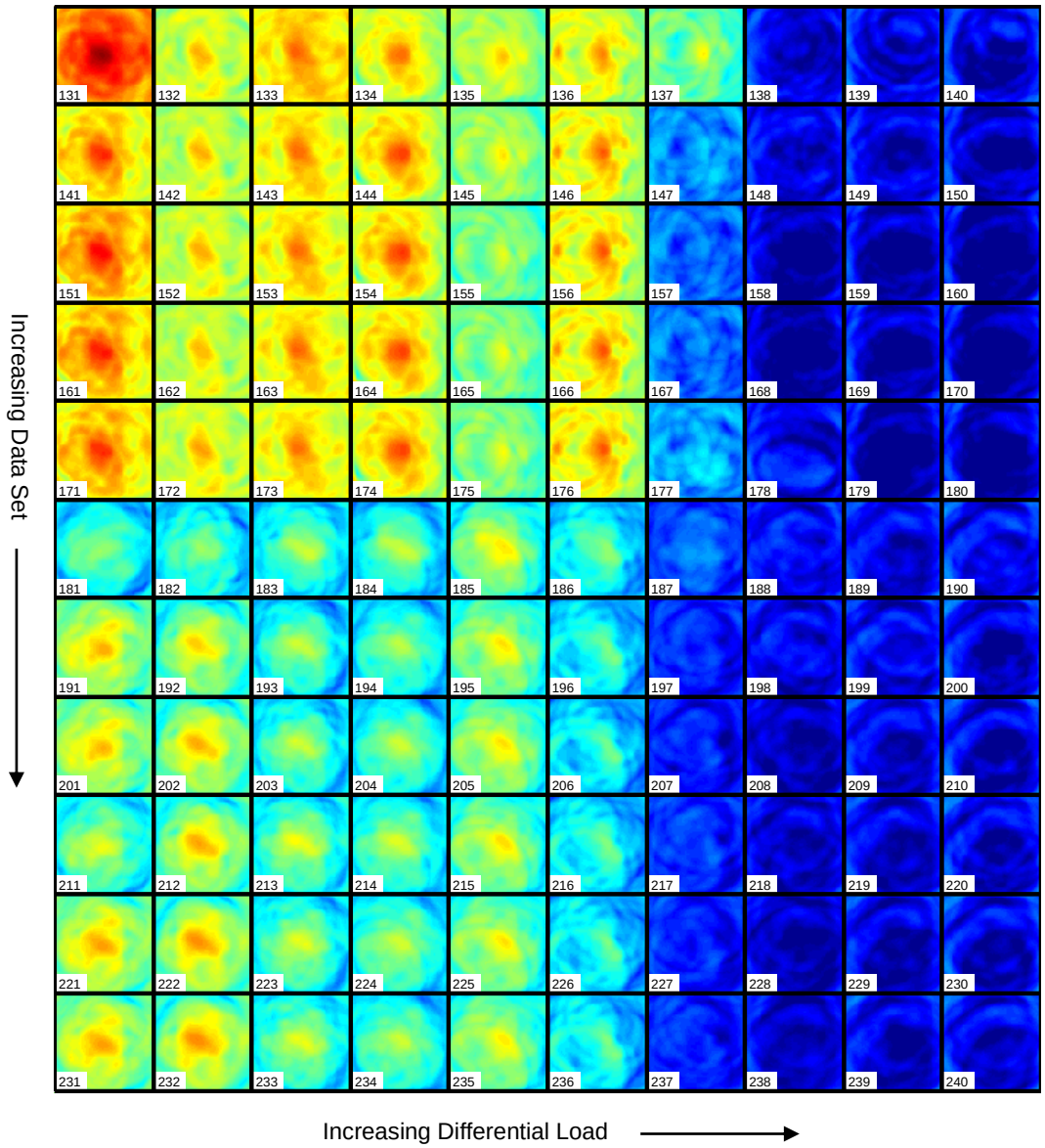

Figure 6.17. Load-differential images of data sets 14-24 from Plate #5 plotted on a fixed 30 dB scale (-21 to +9 dB).

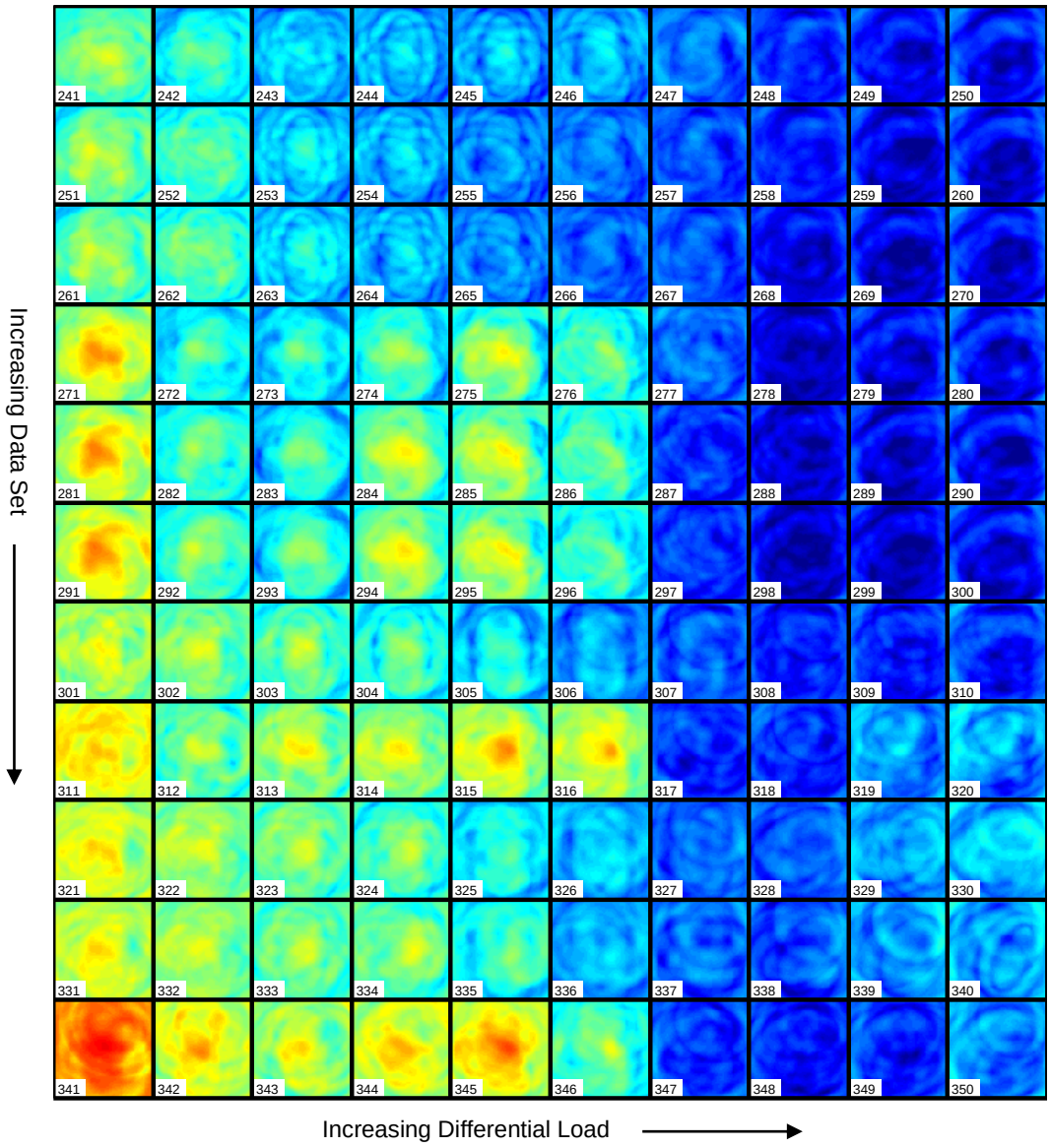

Figure 6.18. Load-differential images of data sets 25-35 from Plate #5 plotted on a fixed 30 dB scale (-21 to +9 dB).

Figure 6.19 shows composite images from all 35 data sets of Plate #5, including those already shown in Figure 6.10. Although the details of the ten load-differential images for each data set are not displayed, many of the same deductions can be made. This figure illustrates the usefulness of the composites images for showing the "big picture" effects of the load-differential imaging method.

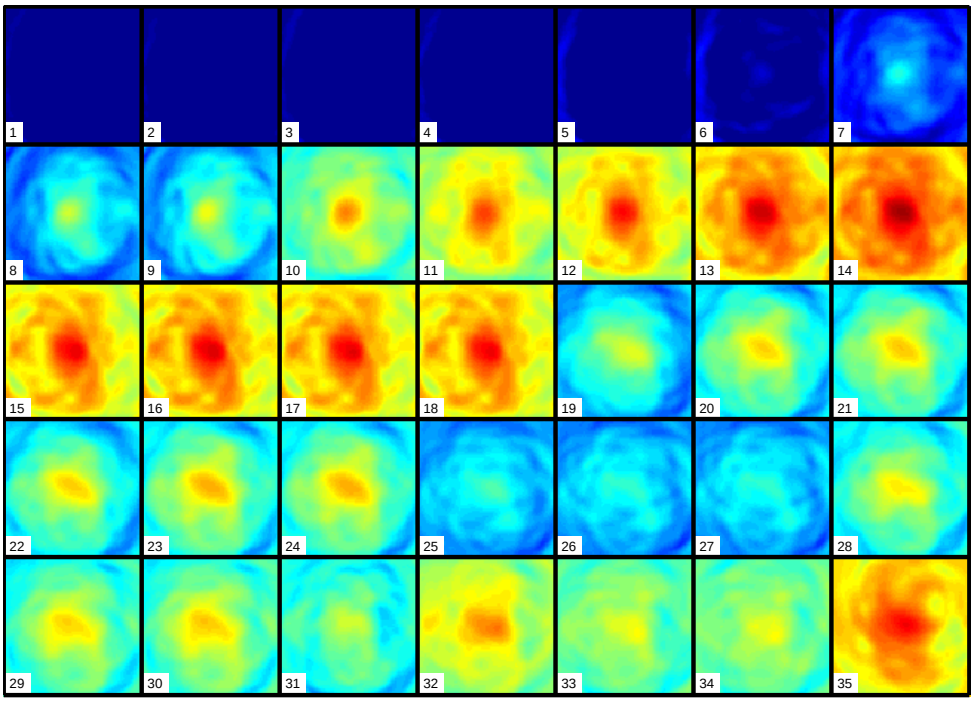

Figure 6.19. Composite load-differential images from all 35 data sets of Plate #5. All images are shown on the same 20 dB color scale (-18 dB to +2 dB).

6.5.4 Plate #6 – Multiple holes and crack initiation sites

The original intent of Plate #6 was to include multiple holes so that signals would include both multiple scattering from the holes and multiple cracks. Notches were made in two of the four holes (outside of the two inner holes) with the expectation that cracks would primarily grow from these two notches. However, that was not the case as can be seen from Table 3.7 in Section 3.6. Crack growth was very complicated with multiple cracks growing from the two inner holes, and ultimately cracks also grew from one of the other holes.

Figure 6.20 shows load-differential images from data sets 3 through 16, which is from the undamaged condition up through the end of fatiguing. Data sets 1 and 2 are not shown; data set 2 has one bad signal that results in two differential images with elliptical artifacts. Data set 1 does not show any loading effects, as would be expected prior to fatiguing. The background noise level in these images indicates possible transducer problems, although there are not any data sets that are clearly bad. Data set 9 is ambiguous in terms of whether load-dependent activity is caused by bad transducers versus cracking; data set 11 is the first one with unambiguous indications of cracking. At this point there are six cracks with the largest ones about 5 mm in length (on the surface). This point of detection is similar to that achieved with Plates #3 and #5, where unambiguously detected crack lengths were about 3 and 5 mm, respectively. Subsequent data sets show progression of cracking combined with possible transducer degradation issues as manifested by the characteristic elliptical patterns on the images.

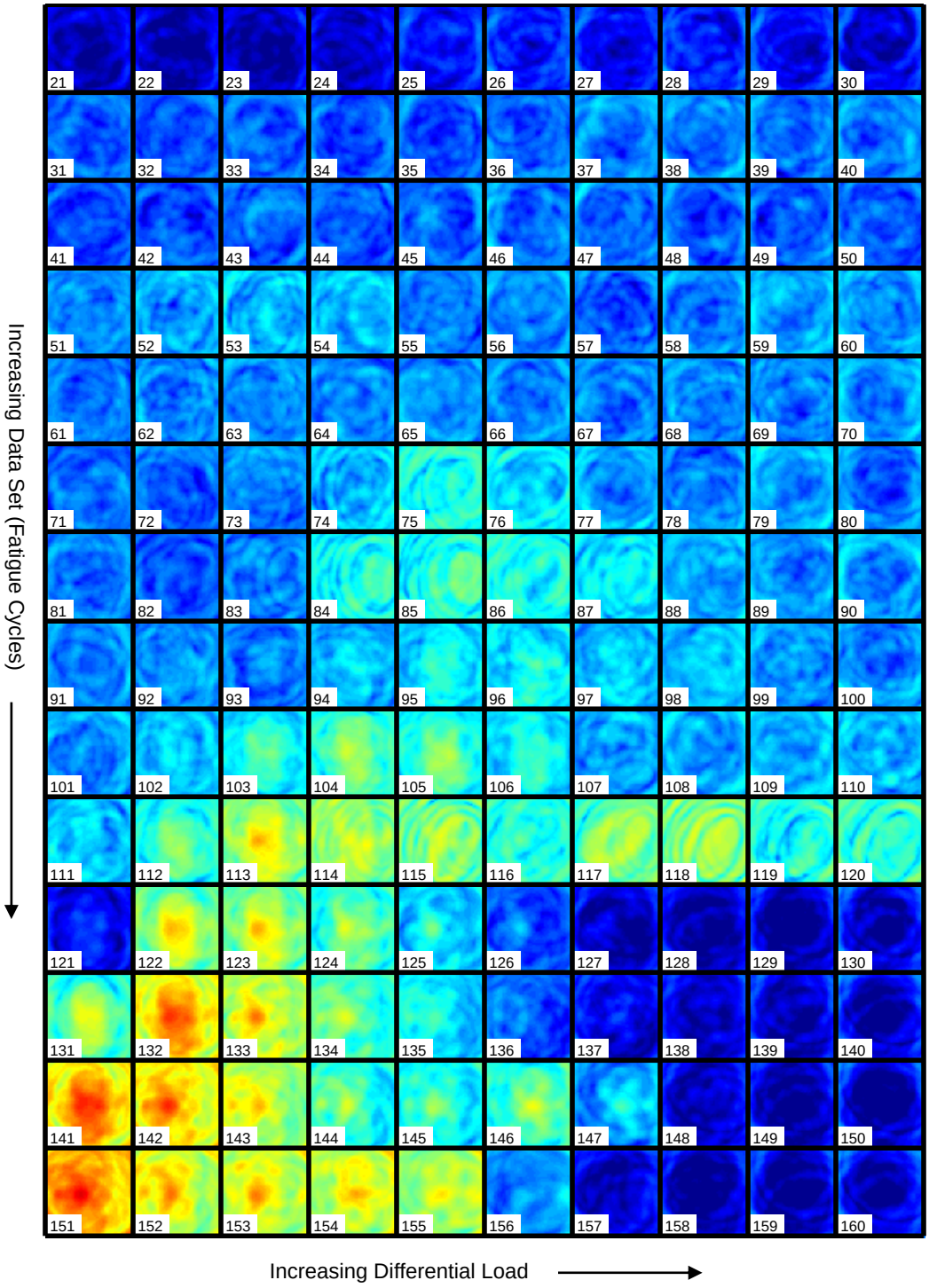

Figure 6.20. Load-differential images of data sets 3-16 from Plate #6 plotted on a fixed 30 dB scale (-21 to +9 dB).

Figure 6.21 shows load-differential images from data sets 16 and 18 through 25, which include the last data set after fatiguing terminated (16) and all of the remaining ones. Data sets 18 through 25 are at nominally the same structural conditions (cracks) but were recorded at slightly different temperatures. The temperature was increased by enclosing the specimen in an insulated box containing a heating pad. The entire testing machine acted as a heat sink and it was not possible to raise the temperature more than about 2.5 °C. In addition, the amplitude changed by several dB between the various measurements because of an uncontrolled amplifier problem. It can be seen that the load-differential images for data sets 16 and 18-21 are very close to each other, illustrating that this method is inherently not dependent upon temperature. However, data sets 22-24 do show some changes, most likely due to permanent deformation caused by the extended static loadings.

Figure 6.22 shows composite load differential images from all 23 data sets of Plate #6. These images are consistent with the individual ones of Figure 6.20 and 6.21. Data from this plate illustrate that load-differential imaging can be effective in the presence of complexity caused by both multiple scatterers and multiple cracks, and that it is not dependent upon temperature.

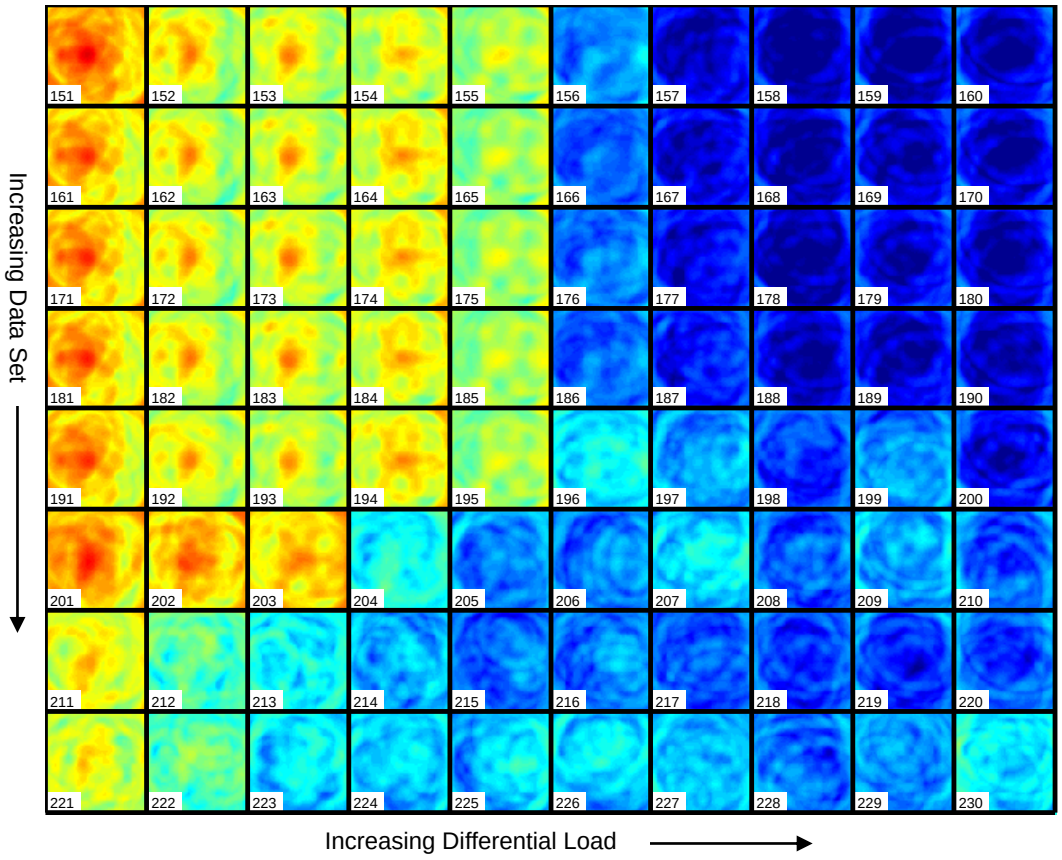

Figure 6.21. Load-differential images of data sets 16 and 18-24 from Plate #6 plotted on a fixed 30 dB scale (-21 to +9 dB).

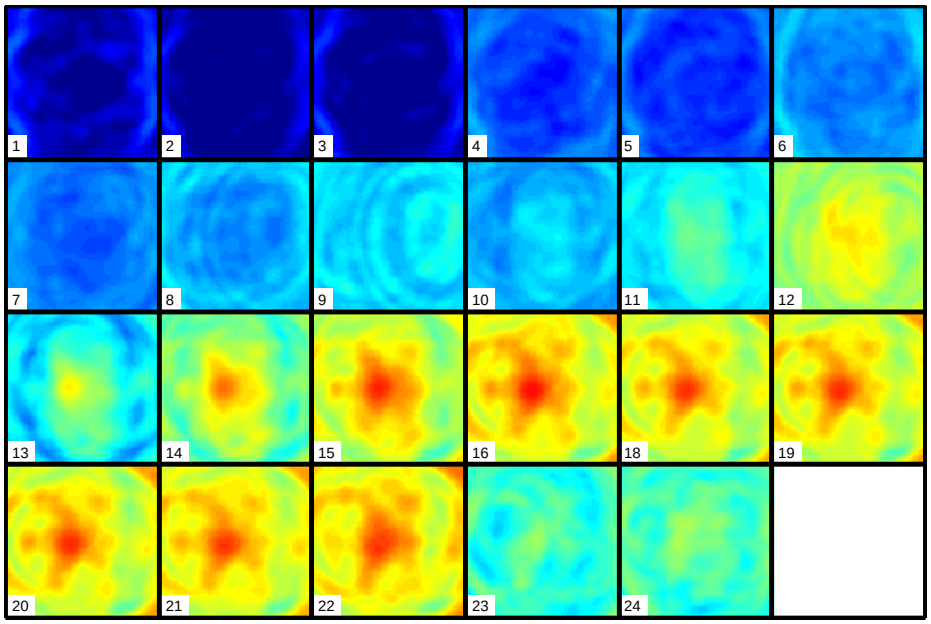

Figure 6.22. Composite load-differential images from all 23 data sets of Plate #6 (1-16 and 18-24). All images are shown on the same 20 dB color scale (-18 dB to +2 dB).

6.5.5 Plate #7 – Added doubler and fasteners

The initial state of Plate #7 included a bonded doubler with a drilled through-hole. A starter notch was made in the plate (not the doubler) as a site for initiation of cracking. The plate was fatigued until the maximum crack length was about 11 mm, at which point it was observed that the doubler had become partially unbonded at one end. Then two holes were drilled about 1" from each end of the doubler, and bolts were installed to secure the doubler to the plate. Fatiguing continued until the crack grew to about 15 mm in length.

Figure 6.23 shows load differential images from all 12 data sets of Plate #7. The doubler was bonded to the plate prior to taking any data, and the first two data sets show some initial bonding changes in the doubler. In particular, data set 2 shows the right end of the doubler becoming partially disbonded, as can be seen from the higher amplitude indications on the right side of the image as the loads increase. This disbonding was not noticed when it occurred, so fatiguing began after data set 2 was recorded. Data sets 3 and 4 do not show any more evidence of the doubler disbonding, and the first evidence of cracking can be seen in data set 5 at high load levels. The crack continues to grow as is evidenced by the higher amplitude localization taking place at progressively lower loads. After data set 7 the disbonding of the doubler was visually observed, and after data set 8 the doubler was secured by drilling holes and installing bolts about 1" from either end. Fatiguing continued with data sets 11 and 12, and the installed bolts appeared to have minimal effects on the load-differential images. Fatiguing was discontinued after data set 12 when the largest crack was about 15 mm in length.

Composite images are shown in Figure 6.24 for all 12 data sets. In the composite images it is clear that the doubler disbonding stabilized after data set 2 with no further load-differential effects. Evidence of cracking is seen at data set 5, as was the case for the individual load-differential images, and at this point the largest crack was about 5 mm in length. Drilling of the holes and installation of the bolts to secure the doubler are not apparent in these images, illustrating the insensitivity of the method to structural changes that are not load-dependent.

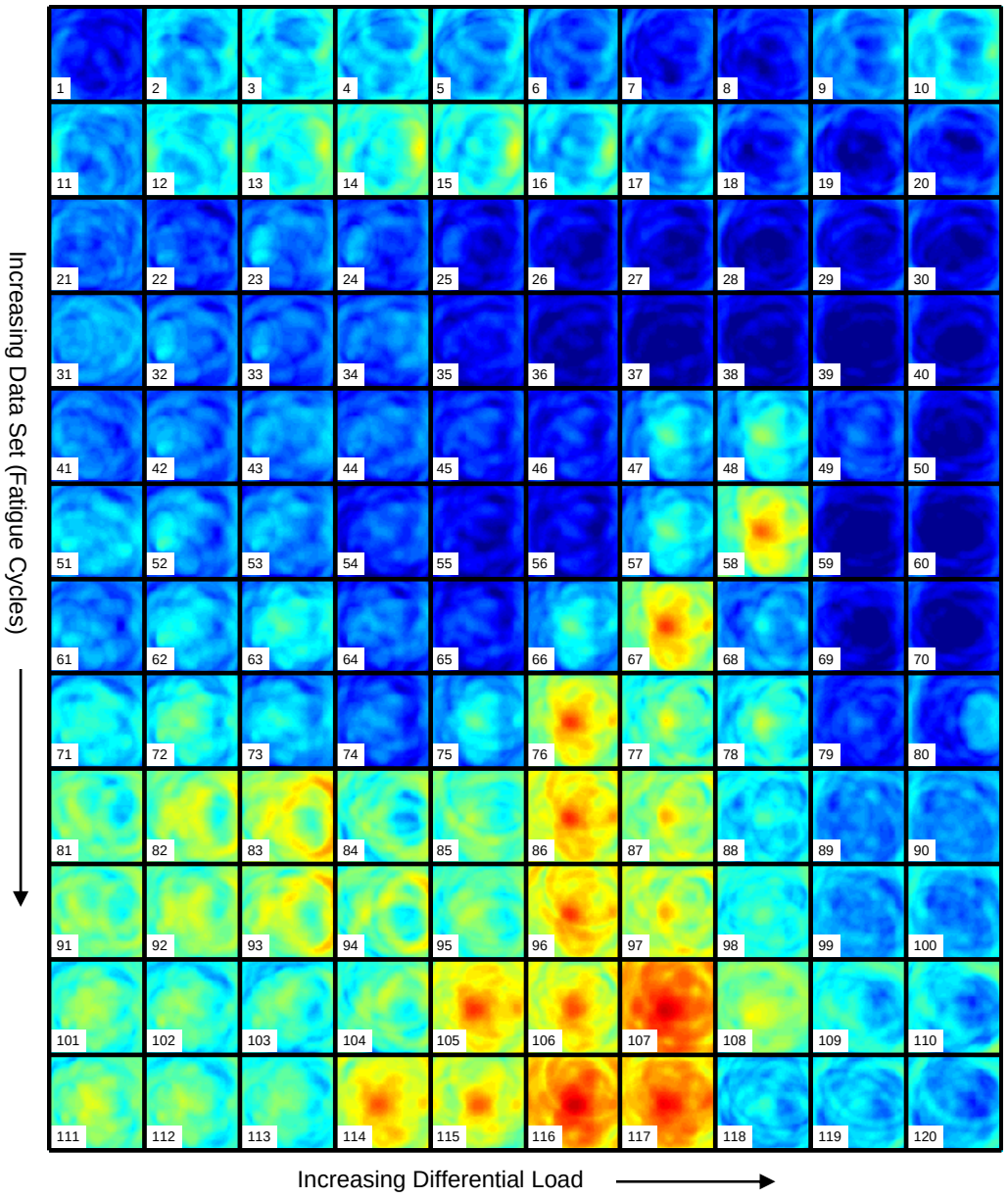

Figure 6.23. Load-differential images of all 12 data sets from Plate #7 plotted on a fixed 30 dB scale (-21 to +9 dB).

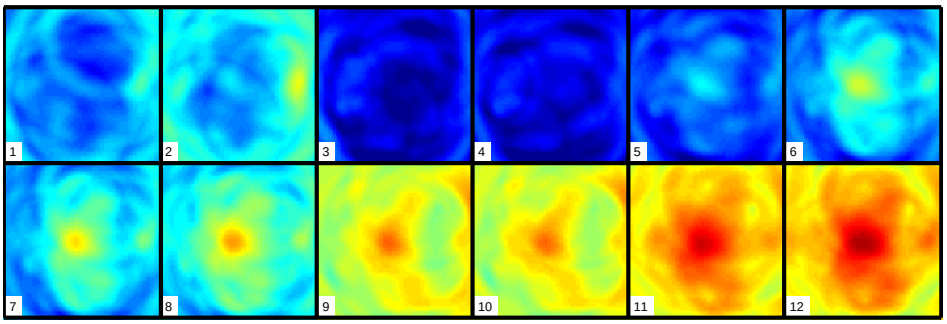

Figure 6.24. Composite load-differential images from all 12 data sets of Plate #7. All images are shown on the same 20 dB color scale (-18 dB to +2 dB).

6.5.6 Plate #8 – Added doubler and fasteners plus transducer problems

The intent was for Plate #8 to be similar to Plate #7 with a bonded and bolted doubler. Based upon the experience with Plate #7, the doubler was initially both bonded to the plate and bolted at both ends; no bolt was inserted in the center hole. Two data sets were recorded prior to fatiguing, and both appeared to be reasonable with no significant load-dependent changes. Fatiguing began, and after 3000 cycles data were again recorded. This data showed load-dependent changes that did not appear to be related to cracking or disbonding; transducer problems were suspected. Two additional data sets were recorded, and it was decided to replace transducers #1 and #6. After they were replaced, the two bolts were removed and fatiguing was restarted. Data were recorded until the maximum crack length was about 12 mm.

Figure 6.25 shows all load-differential images from the 13 data sets of Plate #8, and results are difficult to interpret. There are no patterns in the data that appear to be related to cracks, which have the characteristic signature of opening at lower loads as the crack size increases. Since the visual observations clearly showed typical crack growth, the cracking must be obscured by either unstable bonding of the doubler, transducer variations, or a combination of the two. The composite load-differential images of Figure 6.26 are similarly inconclusive. The first two data sets show a stable specimen, and the next three indicate load-dependent changes. The elliptical pattern of data set 6 indicates a problem with transducer pair 5-6. Subsequent data sets show increased load variations as fatiguing progresses, but the localization in the image is not suggestive of cracking in the center of the plate.

This final fatigue test, although not providing a positive result, does point out the importance of having a relatively stable specimen. The experience of the authors on other projects is that real aerospace specimens are more structurally stable in terms of bonds and interfaces than specimens fabricated in the laboratory [44]. The results from Plate #8 also point out the need of having robust transducer diagnostics to definitively either identify or rule out transducer problems. In the tests performed here, the method described in [45] was used for transducer diagnostics; it was generally effective but not always able to identify subtle transducer problems.

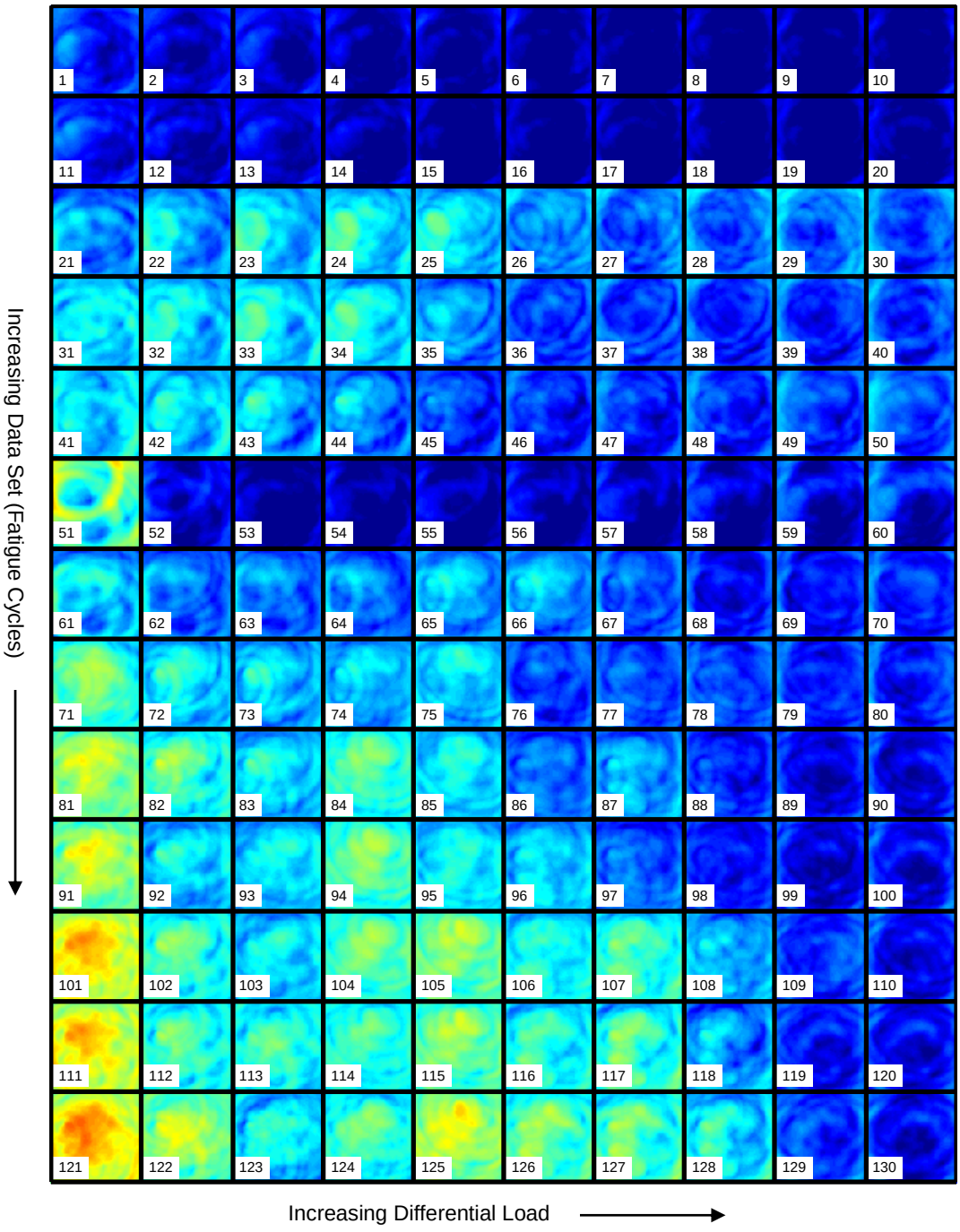

Figure 6.25. Load-differential images of all 13 data sets from Plate #8 plotted on a fixed 30 dB scale (-21 to +9 dB).

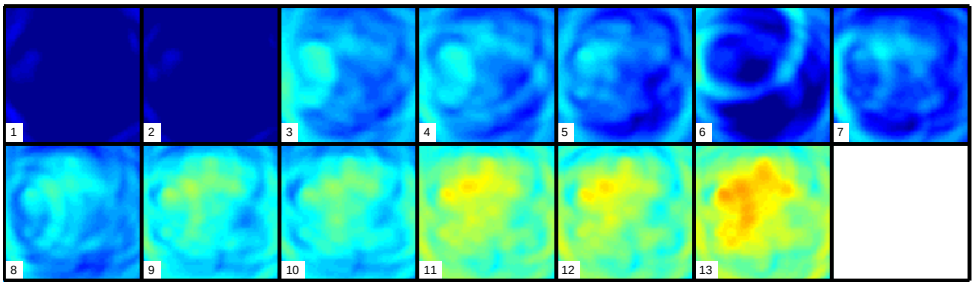

Figure 6.26. Composite load-differential images from all 13 data sets of Plate #8. All images are shown on the same 20 dB color scale (-18 dB to +2 dB).

6.6 Section Summary: Load-Differential Imaging

This section has reported the positive and negative effects of loads on ultrasonic guided wave imaging systems that are based upon changes from damage-free reference signals. A large mismatched load causes significant changes in ultrasonic signals and can thus result in both false alarms (when there is no damage) and missed detection of damage if it is present. However, a relatively small load can open cracks to enhance their detectability. These observations have motivated the introduction and demonstration of a load-differential imaging method for fatigue crack detection and localization for which the reference signals are taken to be at the same damage state but at different loads. A series of images generated from load-differential signals clearly shows the initiation and progression of fatigue crack growth. Furthermore, load-differential imaging has the potential for identifying multiple cracks if they open at different loads.

Load-differential methods clearly demonstrate the importance of having open cracks to ensure their reliable detection. It should also be noted that temperature or other environmental conditions will not adversely affect load-differential imaging performance as long as there are not significant changes in between load steps. Experiments with bonded components showed mixed results. For the case where the bonding was not changing under load, load-differential methods were not able to detect a disbond, which is not unexpected. Cracks were still able to be clearly detected for well-bonded components, but severe variation of boundary conditions during loading obscured cracks. Several of the experiments also pointed out the importance of ensuring the health of the transducers as loads are varied.

7. Concluding Remarks

This three year project accomplished its primary objective of using loading effects to monitor damage with guided waves but without a direct baseline comparison. The load-differential method was successfully demonstrated to detect fatigue cracks by their load-dependent response. In some cases localization of individual cracks was achieved. The success of the method strongly depends upon two conditions: (1) knowledge of the load associated with each recorded signal, and (2) the absence of other changes taking place during the load variations. In particular, experimental results demonstrated the importance of both stable transducers and boundary conditions during load variations, although some changes in both were fairly well tolerated. Although not specifically investigated as part of this project, changes in boundary conditions such as are caused by disbonds may be the desired damage type to detect, in which case sensitivity to these boundary conditions changes would be desirable.

Data recorded from tests performed as part of this project were analyzed primarily using conventional delay-and-sum imaging. This analysis technique not only provided a convenient way to combine data from multiple transducer pairs, it also gave confidence in the consistency of the data by providing localization information. However, it is not the only possible analysis method. Signal difference and correlation based methods in common use could also be applied, as could adaptive imaging methods that have been used for similar problems [46,47]. Modeling to better understand the expected load-dependent response from both cracks and other sources of scattering could also enable better analysis methods.

The effects of loading on baseline comparison methods were also evaluated as part of this project. It was shown that if signals and baselines are recorded at different loads, signal changes are significant and could lead to either false alarms or masking of damage. The general anisotropic nature of applied loads inherently prevents application of methods developed for temperature compensation, which points to the importance of knowing the current loading state.

Results from this project also point out the well-known difficulty of detecting tightly closed fatigue cracks using ultrasonic methods. Many proposed SHM systems are considering permanently mounted sensors combined with ground-based instrumentation that interrogates the sensors on the ground under static conditions. The danger of this approach is that some fatigue cracks may be tightly closed under these conditions and thus undetectable. On the other hand, instantaneous measurement of dynamic loads in flight may also be problematic, as well as achieving the range of loads needed to implement a full load-differential measurement. This study provides initial data to help determine if the benefits of such an approach outweigh the obstacles to implementation. It also may provide justification to change ground-based testing methods to ensure that cracks are open by application of appropriate static loads.

Acknowledgments

The following six individuals, who are the authors of this report, were the primary contributors to this project:

- Professor Jennifer E. Michaels, Principal Investigator
- Professor Thomas E. Michaels, Co-Principal Investigator
- Dr. Sang Jun Lee, Postdoctoral Associate
- Mr. Xin Chen, Graduate Research Assistant
- Mr. Navneet Gandhi, Graduate Research Assistant
- Mr. Fan Shi, Graduate Research Assistant

The following individual also contributed to this project:

- Mr. Shiv Chawla, Graduate Research Assistant
- Mr. Ross Levine, Graduate Research Assistant
- Ms. Honglei Li, Graduate Research Assistant

References

1. J. L. Rose, "Guided wave nuances for ultrasonic nondestructive evaluation," *IEEE Trans. Ultrason, Ferroelect. Freq. Contr.*, **47**(3), pp. 575-583, 2000.
2. R. P. Dalton, P. Cawley, and M. J. S. Lowe, "The potential of guided waves for monitoring large areas of metallic aircraft fuselage structure," *Journal of Nondestructive Evaluation*, **20**(1), pp. 29-46, 2001.
3. A. J. Croxford, J. Moll, P. D. Wilcox, and J. E. Michaels, "Efficient temperature compensation strategies for guided wave structural health monitoring," *Ultrasonics*, **50**, pp. 517-528, 2010.
4. Y. Lu and J. E. Michaels, "Feature extraction and sensor fusion for ultrasonic structural health monitoring under changing environmental conditions," *IEEE Sensors Journal*, **9**(11), pp. 1462-1471, 2009.
5. X. Zhao, R. L Royer, S. E. Owens and J. L. Rose, "Ultrasonic Lamb wave tomography in structural health monitoring," *Smart Materials and Structures*. **20**, 105002, 2011.
6. L. Yu and V. Giurgiutiu, "In situ 2-D piezoelectric wafer active sensors arrays for guided wave damage detection," *Ultrasonics*, **48**, pp. 117-134, 2008.
7. C. H. Wang, J. T. Rose, and F.-K. Chang, "A synthetic time-reversal imaging method for structural health monitoring," *Smart Materials and Structures*, **13**(2), pp. 415-423, 2004.
8. J. E. Michaels, "Detection, localization and characterization of damage in plates with an *in situ* array of spatially distributed ultrasonic sensors," *Smart Materials and Structures*, **17**, No. 035035 (15pp), 2008.
9. T. Clarke, P. Cawley. P. D. Wilcox and A. J. Croxford, " Evaluation of the damage detection capability of a sparse-array guided-wave SHM system applied to a complex structure under varying thermal conditions," *IEEE Transactions on Ultrasonics, Ferrolectrics, and Frequency Control*, **56**(12), pp. 2666-2678, 2009.

10. P. Fromme, “Influence of guided ultrasonic wave scattering directionality on the detection sensitivity for SHM of fatigue cracks,” *Proc. SPIE,* **7650**, 76501M (10 pages), 2010.

11. Y. Lu and J. E. Michaels, “A methodology for structural health monitoring with diffuse ultrasonic waves in the presence of temperature variations,” *Ultrasonics*, **43**, pp. 717-731, 2005.

12. G. Konstantinidis, B. W. Drinkwater, and P. D. Wilcox, “The temperature stability of guided wave structural health monitoring systems,” *Smart Material and Structures*, **15**(4), pp. 967-976, 2006.

13. T. Clarke, F. Simonetti and P. Cawley, “Guided wave health monitoring of complex structures by sparse array systems: Influence of temperature changes on performance,” *Journal of Sound and Vibration*, **329**, pp. 2306-2322, 2010.

14. J. Takatsubo, B. Wang, H. Tsuda, N. Toyama, and K. Urabe, “Ultrasonic spectroscopy for the identification of defects and environmental disturbances,” (in Japanese) *Trans. Jpn. Soc. Mech. Eng. Series A*, **72**, pp. 179–185, 2006.

15. H. Li, J. E. Michaels, S. J. Lee, and T. E. Michaels, “Quantification of surface wetting in plate-like structures via guided waves,” in *Review of Progress in QNDE*, **31**, in press, expected 2012.

16. D. S. Hughes and J. L. Kelly, “Second-order elastic deformation of solids,” *Phys. Rev.*, **92**, pp. 1145-1149, 1953.

17. R. A. Toupin and B. Bernstein, “Sound waves in deformed perfectly elastic materials. Acoustoelastic effect,” *J. Acoust. Soc. Am.*, **33**, pp. 216-225, 1961.

18. Y.-H. Pao, W. Sachse, and H. Fukuoka, "Acoustoelasticity and ultrasonic measurement of residual stress," in *Physical Acoustics Volume XVII*, Eds. W. P. Mason and R. N. Thurston (Academic Press, New York), pp. 61-143, 1984.

19. M. Duquennoy, M. Ouaftouh, M. Ourak, and F. Jenot, “Theoretical determination of Rayleigh wave acoustoelastic coefficients: comparison with experimental values,” *Ultrasonics*, **39**, pp. 575-583, 2002.

20. Y. Iwashimizu and O. Kobori, “The Rayleigh wave in a finitely deformed isotropic elastic material,” *J. Acoust. Soc. Am.*, **64**(3), pp. 910-916, 1978.

21. D. Husson, “A perturbation theory for the acoustoelastic effect of surface waves,” *J. Appl. Phys.*, **57**(5), pp. 1562-1568, 1985.

22. J. Qu and G. Liu, “Effects of residual stress on guided waves in layered media,” *Rev. Prog. Quant. NDE*, **17**, D. O. Thompson and D. E. Chimenti (Eds.), Plenum Press, pp. 1635-1642, 1998.

23. P. Rizzo and F. Lanza di Scalea, “Effect of frequency on the acoustoelastic response of steel bars,” *Exp. Tech.*, **27**(6), pp. 40-43, 2003.

24. M. Lematre, G. Feuillard, T. Delaunay, and M. Lethiecq, “Modeling of ultrasonic wave propagation in integrated piezoelectric structures under residual stress,” *IEEE Trans. Ultrason. Ferroelect. Freq. Contr.*, **53**(4), pp. 685-696, 2006.

25. F. Chen and P. D. Wilcox, “The effect of load on guided wave propagation,” *Ultrasonics*, **47**, pp.111-122, 2007.

26. J. D. Frandsen, R. V. Inman, and O. Buck, “Comparison of acoustic and strain gauge techniques for crack closure,” *International Journal of Fracture*, **11**, pp. 345–348, 1975.

27. S. J. Bowles, C. A. Harding, and G. R. Hugo, “Effect of crack closure on ultrasonic detection of fatigue cracks at fastener holes,” *Review of Progress in QNDE*, **28B**, pp. 1878-1885, 2009.

28. J. Y. Kim, V. A. Yakovlev, and S. I. Rokhlin, "Surface acoustic wave modulation on a partially closed fatigue crack," *Journal of the Acoustical Society of America,* **115**, pp. 1961–1972, 2004.

29. B. Mi, J. E. Michaels and T. E. Michaels, "An ultrasonic method for dynamic monitoring of fatigue crack initiation and growth," *Journal of the Acoustical Society of America,* **119**(1), pp. 74-85, 2005.

30. G. D. Connolly and S. I. Rokhlin, "Quantitative enhancement of fatigue crack monitoring by imaging surface acoustic wave reflection in a space-cycle-load domain," *in Review of Progress in QNDE,* **30**, pp. 1499-1506, 2011.

31. Y. Ohara, S. Horinouchi, M. Hashimoto, Y. Shintaku, and K. Yamanaka, "Nonlinear ultrasonic imaging method for closed cracks using subtraction of responses at different external loads," *Ultrasonics*, **51**, pp. 661-666, 2011.

32. J. E. Michaels, S. J. Lee, J. S. Hall, and T. E. Michaels, "Multi-mode and multi-frequency guided wave imaging via chirp excitations," *Proceedings of SPIE*, **7984**, edited by T. Kundu, 79840I (11 pp), 2011.

33. Y.-H. Pao and U. Gamer, "Acoustoelastic waves in orthotropic media," *J. Acoust. Soc. Am.*, **77**, pp. 806-812, 1985.

34. A. H. Nayfeh and D. E. Chimenti, "Free wave propagation in plates of general anisotropic media," *J. Appl. Mech.*, **56**, pp. 881-886, 1989.

35. J. L. Rose, *Ultrasonic Waves in Solid Media* (Cambridge University Press, 1999).

36. N. Gandhi, *Determination of Dispersion Curves for Acoustoelastic Lamb Wave Propagation*, M.S. Thesis, Georgia Institute of Technology, 2010.

37. J. R. Asay and A. H. Guenther, "Ultrasonic studies of 1060 and 6061-T6 aluminum", *Journal of Applied Physics*, **38**, pp. 4086-4088, 1967.

38. M. Dubuget, R. El Guerjouma, S. Dubois, J. C. Baboux, and A. Vincent, "Characterization of the non-linear elastic properties of aluminium alloys using ultrasonic evaluation under load," *Materials Science Forum*, **217-222**, pp. 951-956, 1996.

39. R. T. Smith, R. Stern, and R. W. B. Stephens, "Third-order elastic moduli of polycrystalline metals from ultrasonic velocity measurements", *J. Acoust. Soc. Am.*, **40**, pp. 1002-1008, 1966.

40. Y. Li and R. B. Thompson, "Influence of anisotropy on the dispersion characteristics of guided ultrasonic plate modes," *J. Acoust. Soc. Am.*, **87**, pp. 1911-1931, 1990.

41. M. Castaings and B. Hosten, "Lamb and SH waves generated and detected by air-coupled ultrasonic transducers in composite material plates," *NDT&E International*, **34**, pp. 249-258, 2001.

42. A. D. Degtyar and S. I. Rokhlin, "Absolute stress determination in orthotropic materials from angular dependence of ultrasonic velocities," *Journal of Applied Physics*, **78**(3), pp. 1547-1556, 1995.

43. N. Gandhi and J. E. Michaels, "Efficient perturbation analysis of Lamb wave dispersion curves," *Review of Progress in Quantitative Nondestructive Evaluation*, **29A**, D. O. Thompson and D. E. Chimenti (Eds.), American Institute of Physics, pp. 215-222, 2010.

44. J. E. Michaels, T. E. Michaels and A. C. Cobb, "Ultrasonic monitoring of structural 'hot spots' during full scale fatigue tests," *Proceedings of the 6th International Workshop on Structural Health Monitoring*, F.-K. Chang (Ed.), DEStech Publications, Inc., Lancaster, PA, pp. 1576-1583, 2007.

45. S. J. Lee, J. E. Michaels, H. Sohn and T. E. Michaels, "Guided wave-based PZT diagnostics via linear reciprocity," *AIAA Journal*, **49**(3), pp. 621-629, 2011.

46. J. S. Hall and J. E. Michaels, "Minimum variance ultrasonic imaging applied to an *in situ* sparse guided wave array," *IEEE Transactions on Ultrasonics, Ferroelectrics, and Frequency Control*, **57**(10), pp. 2311-2323, 2010.

47. J. S. Hall, P. McKeon, L. Satyanarayan, J. E. Michaels, N. F. Declercq and Y. H. Berthelot, "Minimum variance guided wave imaging in a quasi-isotropic composite plate," *Smart Materials and Structures*, **20**, 025013 (8pp), 2011.

48. J. S. Hall, P. Fromme, and J. E. Michaels, "Ultrasonic guided wave imaging for damage characterization," *2011 Aircraft Airworthiness & Sustainment Conference*, San Diego, CA, April 18-21, 2011 (available online at http://www.airworthiness.com)

Project Publications and Presentations

Refereed Publications

1. J. E. Michaels, N. Gandhi and S. J. Lee, "Acoustoelastic Lamb Waves and Implications for Structural Health Monitoring," in *From Waves in Complex Systems to Dynamics of Generalized Continua -- Tributes to Professor Yih-Hsing Pao on his 80th Birthday*, K. Hutter, T.-T. Wu and Y.-C. Shu (Eds.), World Scientific, Hackensack, New Jersey, Chapter 4, 2011.
2. S. J. Lee, J. E. Michaels, H. Sohn and T. E. Michaels, "Guided wave-based PZT diagnostics via linear reciprocity," *AIAA Journal*, **49**(3), pp. 621-629, 2011.
3. J. E. Michaels, S. J. Lee and T. E. Michaels, "Effects of applied loads and temperatures on ultrasonic guided waves," *Proceedings of the 2010 European Workshop on Structural Health Monitoring*, DEStech Publications, Inc., Lancaster, PA, pp. 1267-1272.
4. J. E. Michaels, S. J. Lee, X. Chen and T. E. Michaels, "Load-enhanced imaging of fatigue cracks via sparse guided wave arrays," *Proceedings of the 8th International Workshop on Structural Health Monitoring*, F.-K. Chang (Ed.), DEStech Publications, Inc., Lancaster, PA, pp. 1150-1157, 2011.
5. J. E. Michaels, S. J. Lee, A. J. Croxford and P. D. Wilcox, "Chirp excitation of ultrasonic guided waves," submitted to *Ultrasonics*, November 2011, under review.
6. N. Gandhi, J. E. Michaels and S. J. Lee, "Acoustoelastic Lamb wave propagation in biaxially stressed plates," submitted to the *Journal of the Acoustical Society of America*, January 2012, under review.
7. X. Chen, J. E. Michaels, S. J. Lee and T. E. Michaels, "Load-differential imaging for detection and localization of fatigue cracks using Lamb waves," submitted to *NDT&E International*, February 2012, under review.
8. F. Shi, J. E. Michaels and S. J. Lee, "*In situ* estimation of applied biaxial loads with Lamb waves," submitted to the *Journal of the Acoustical Society of America*, April 2012, under review.

Non-Refereed Publications

9. N. Gandhi and J. E. Michaels, "Efficient perturbation analysis of Lamb wave dispersion curves," *Review of Progress in Quantitative Nondestructive Evaluation*, **29A**, D. O. Thompson and D. E. Chimenti (Eds.), American Institute of Physics, pp. 215-222, 2010.
10. S. J. Lee, J. E. Michaels, T. E. Michaels and H. Sohn, "*In situ* PZT diagnostics using linear reciprocity under environmental and structural variations," *Proceedings of SPIE, Health Monitoring of Structural and Biological Systems*, **7650**, T. Kundu (Ed.), SPIE, pp. 76500N:1-10, 2010.

11. J. E. Michaels, S. J. Lee and T. E. Michaels, "Impact of applied loads on guided wave structural health monitoring," *Review of Progress in Quantitative Nondestructive Evaluation*, **30B**, D. O. Thompson and D. E. Chimenti (Eds.), American Institute of Physics, pp. 1515-1522, 2011.
12. N. Gandhi, J. E. Michaels and S. J. Lee, "Acoustoelastic Lamb wave propagation in a homogeneous, isotropic aluminum plate," *Review of Progress in Quantitative Nondestructive Evaluation*, **30A**, D. O. Thompson and D. E. Chimenti (Eds.), American Institute of Physics, pp. 161-168, 2011 (1st place winner, student poster competition).
13. S. J. Lee, N. Gandhi, J. E. Michaels and T. E. Michaels, "Comparison of the effects of applied loads and temperature variations on guided wave propagation," *Review of Progress in Quantitative Nondestructive Evaluation*, **30A**, D. O. Thompson and D. E. Chimenti (Eds.), American Institute of Physics, pp. 175-182, 2011.
14. J. E. Michaels, S. J. Lee, X. Chen, F. Shi and T. E. Michaels, "Understanding and exploiting applied loads for guided wave structural health monitoring," *2011 Aircraft Airworthiness & Sustainment Conference*, San Diego, CA, April 18-21, 2011 (available online at http://www.airworthiness.com).
15. S. J. Lee, J. E. Michaels, X. Chen and T. E. Michaels, "Fatigue crack monitoring via load-differential guided wave methods," *Review of Progress in Quantitative Nondestructive Evaluation*, **31**, D. O. Thompson and D. E. Chimenti (Eds.), American Institute of Physics, expected 2012.
16. F. Shi, J. E. Michaels and S. J. Lee, "An ultrasonic guided wave method to estimate applied biaxial loads," *Review of Progress in Quantitative Nondestructive Evaluation*, **31**, D. O. Thompson and D. E. Chimenti (Eds.), American Institute of Physics, expected 2012.
17. X. Chen, S. J. Lee, J. E. Michaels and T. E. Michaels, "Load-differential features for automated detection of fatigue cracks using guided waves," *Review of Progress in Quantitative Nondestructive Evaluation*, **31**, D. O. Thompson and D. E. Chimenti (Eds.), American Institute of Physics, expected 2012.
18. J. E. Michaels and T. E. Michaels, "Signal processing and imaging with ultrasonic guided waves: goals, challenges and recent progress," *Proceedings of the 18th World Conference on Nondestructive Testing*, April 16-20, 2012, Durban, South Africa (invited paper).

M. S. Thesis

19. N. Gandhi, *Determination of Dispersion Curves for Acoustoelastic Lamb Wave Propagation*, M.S. Thesis, Georgia Institute of Technology, 2010.

Presentations Without Proceedings

20. J. E. Michaels, "Acoustoelastic Lamb Waves and Implications for Structural Health Monitoring," presented at the *2010 International Symposium on Experimental Mechanics*, Taipei, Taiwan, May 20-21, 2010 (Invited Presentation).

Seminar Presentations (includes results from this project)

21. J. E. Michaels, "A Vision for Guided Wave Structural Health Monitoring: Issues and Recent Progress," presented at the University of Arizona, Department of Civil Engineering, Tucson, Arizona, April 2011 (Invited Presentation).
22. J. E. Michaels, "Recent Advances in Guided Wave Structural Health Monitoring at Georgia Tech," presented at the Naval Air Systems Command, Structures Division, Patuxent River Naval Air Station, Maryland, June 2011.

23. J. E. Michaels, "Structural Health Monitoring with Guided Waves: Goals, Challenges and Recent Progress," presented at the IEEE Signal Processing/AESS/GRSS Atlanta Chapters Monthly Meeting, Atlanta, Georgia, August 2011 (Invited Presentation).
24. J. E. Michaels, "Signal Processing and Imaging with Ultrasonic Guided Waves: Application to Structural Health Monitoring," presented at Carnegie Mellon University, Department of Electrical and Computer Engineering, Pittsburgh, Pennsylvania, September 2011 (Invited Presentation).
25. J. E. Michaels, "Structural Health Monitoring with Ultrasound: Overview, Challenges and Recent Progress," presented at Rensselaer Polytechnic Institute, Department of Mechanical, Aerospace, and Nuclear Engineering, Troy, New York, February 2012 (Invited Presentation).